Response to Reviewers' Comments

Min-Jee Kang, Hye-Yeong Chun, and Rolando R. Garcia

October 13, 2020

Dear editor and reviewers,

We received four reviews for our manuscript "Role of equatorial planetary and gravity waves in the 2015–16 quasi-biennial oscillation disruption". First of all, we would like to thank all the reviewers for their time spent on reviewing our long manuscript. All reviews have been beneficial and made us aware of important points which had to be addressed. We, the authors, are therefore thankful for their contribution to improve the manuscript. We carefully addressed all comments and tried our best to improve the manuscript based on the suggestions and comments.

During the revision process, we changed the title to "Role of equatorial waves and convective gravity waves in the 2015–16 quasi-biennial oscillation disruption". In addition, we newly included (i) the time series of the meridional and vertical wind shears at 40 hPa in Fig. 4d, (ii) the climatology of the daily $\bar{q}_\phi$ in Fig. 8c, and (iii) the daily EPD for the MRG waves in Fig. 8d. Following the reviewers' suggestions, we added new supplementary figures (Figures S1, S6, and S9) and clarified some points that were unclear in the original manuscript.

We include a point-by-point response to each comment in the following paragraphs. We indicate the original comment of the respective reviewer in blue color and our answer in black color. In addition, we provide a tracked-changed version of the manuscript.

Sincerely,

Hye-Yeong Chun

Response to Reviewer #1's Comments

General Comment:

This paper provides quite many missing pieces of the 2016 QBO disruption puzzle. Previous literature has concentrated on the role of equatorward-propagating extratropical waves, with only a couple papers giving equatorial wave modes any focus.

Overall, the effort made by the authors is quite impressive. All equatorial wave modes are separated and their effect on the wind structure is studied in detail, and additionally parameterized convective GWs are included in the study. As the authors mention, of course the CGW parameterization has some limitations (which parameterization doesn't?), but I think the approach is physically consistent and the CGW results are, at least, qualitatively correct.

The paper is a bit lengthy, but short summaries are provided for the trickier figures, which I appreciated. Overall well written, figures are mostly good, a nice sketch in Fig. 16 to put all together, interesting discussions and definitely worthy of publication in ACP. I only have a fair amount of minor comments, mainly to make some figures or methods easier to interpret for the reader, and in some parts to request a more detailed comparison with recent QBO disruption literature.

Specific Comments:

1) Title: strictly speaking, it's not only planetary wavenumbers that you study, I suggest something more accurate "Role of equatorial waves and convective gravity waves in the 2015/16 QBO disruption" or similar (it's ok to use the QBO abbreviation in the title, since all your potential audience will know what it means)

Thank you for your good suggestion. Following the suggestion, the title is changed to "Role of equatorial waves and convective gravity waves in the 2015–16 quasi-biennial oscillation disruption". [p.1, L1–2]

2) p.2, l.31-33: specify that this is for extratropical latitudes when you refer to polar vortex and its downward impact.

It is specified as suggested. [p.2, L32–33]

3) p.2, l.55: ’is the prerequisite for’

I think a better wording would be ‘... eq. waves preconditioned the extratropical Rossby wave breaking, ...’. prerequisite implies that without the MRG, the ex. Rossby wave breaking and QBO disruption wouldn’t have happened, which to my knowledge cannot be assured 100%.

We agree with you. The sentence is modified as suggested. [p.2, L56]

4) p.2, l.56: ‘... each equatorial wave mode to the QBO...’

It is changed as suggested. [p.2, L57]

5) p.3, l.87-88: sentence is repetitive, can be removed

The sentence is removed as suggested.

6) p.3, l.89-93: specify subsections where each item is done, e.g. specific wave types within section 3

Thank you for your good suggestion. We specified subsections where each item is done. [p. 3, L90–93]

7) p.6, l.178: include the GPM dataset into section 2.1

Thank you for pointing this out. We included the GPM dataset in Sect. 2.1. [p. 4, L106–108]

8) p.6, l.179: Here or perhaps within the supplement, justify why the magnitude and scaling are not crucial for both datasets in Fig. S1 to match: not the exact magnitude, but rather the shape of the vertical profiles is what’s important, correct?

Thank you for your comment. The spatiotemporal variations in the magnitude of convective heating rate are important, but the overall magnitude largely depends on the resolution of the data provided. Therefore, the ‘exact’ magnitude would be less important compared to the shape of the heating profiles. The difference in the overall magnitude can be adjusted by the conversion factor (Kang et al., 2017), a scale factor that constitutes convective source spectrum, when calculating convective gravity wave momentum flux. The related sentence is included in the revised supplement. [Fig. S2]

9) p.6, l.180: SPB –> Since this abbreviation is not used later in the manuscript, I recommend

to keep the full name, and remove the abbreviation from the first time it's used

It is modified as suggested. [p.3, L85; p.7, L186]

10) Figure 1: I suggest making 1(a) the lat.-height sections and 1(b) the vertical profiles and refer to them accordingly in the text.
Also, make it clear in the caption that the climatology is for WQBO years.
Y-axis labels: for better visibility I'd keep the pressure levels only, since the numbers with height in km get mixed up in between panels.

Thank you for your good suggestion. Following the suggestion, we marked (a) and (b) in Fig. 1 and deleted labels of the height axis. We also clarified the meaning of the climatology in the figure caption of Fig. 1 in the revised manuscript. [Fig. 1]

11) p.7, l.188: In section 2.1 you say it will be referred to as WQBO climatology, you may want to rephrase that for consistency. Here, remind the reader that when you're talking about climatology, it refers to WQBO phase.

Thank you for pointing this out! We revised the statement in Sect. 2.1 that the 10-selected years will be referred to as the 'climatology' for conciseness. We also remind the reader of this in the results section. [p.4, L114; p.7, L205–206]

12) p.7, l.199-200: '... positive (negative) drag on the zonal wind in regions of positive (negative) shear, ...'

It is changed as suggested. [p.8, L217–218]

13) p.7, l.212: February –> March

Thank you! It is corrected. [p.8, L234]

14) p.7, l.195-213: I miss some linking of these results with recent literature in this paragraph:
–> How do these results compare to Lin et al. (2019)? Especially for MRG, IG and CGW, it should be highlighted your results build upon those by Lin et al. (2019) (their Fig. 3 is quite similar to yours), that focus mostly on MRG in their discussions. Your eq. wave differentiation is more detailed, which is a big plus.
–> Regarding your Kelvin wave forcing results, I find it really neat that it helps maintain the two westerly jets. This was suggested/hinted by Li et al. (2020), who studied the long-

lasting westerly jet around 20hPa, but your results really confirm this is the case. Li et al. (2020) also showed above-average upper-tropospheric Kelvin wave activity linked to El Nino. This should be mentioned/discussed within this paragraph.

–> Also, this is a very long paragraph, could be easily split into 2-3.

Thank you for your detailed comments. We modified the paragraph as suggested:

- We included a comparison between Fig. 2 and Lin et al. (2019)'s Fig. 3. We also emphasized that the contribution to the QBO disruption from the IG waves is first shown in this study.
- We included a discussion on the long-lasting jet near 20 hPa and its contribution from Kelvin waves, referring to Li et al. (2020).
- We split a paragraph into three.

[p. 8, L221–235]

15) Fig. 3: I suggest to move the climatology plot to the supplement (as it doesn't have crucial information for the main text), and make the rest bigger. Right now this figure is too busy and it's easy to get lost within, specially with the duplicate letters for the sub-panels.

Thank you for your comment. Although we respect the reviewer's suggestion, we decided to keep the figure in the revised manuscript, as two figures (disruption and climatology) together can clearly show how the structures of the wind and wave forcings are unusual during the disruption. We instead changed letters for sub-panels and adjusted each figure to increase visibility as much as possible. [Fig. 3]

16) p.9, l.253-254: Mention to Lin et al. (2019) needed here. Your results are in line with theirs, plus the addition of IG in the preconditioning.

We mentioned Lin et al. (2019) in the revised manuscript as suggested. [p. 10, L279–280]

17) p.10, l.294: origination –> just 'origin'

It is corrected. [p.11, L325]

18) p.11, l.324: I suggest making this (dividing by density) for all figures: the vertical/ horizontal arrows without scaling for pressure in the previous plots, may lead the reader to underestimate upper level wave propagation at first glance, specially if one is quickly comparing upper tropospheric and stratospheric levels without paying much attention to

the legend.

However, this is not a must: the figures have the divergence in pressure-independent units, and the units of the arrows are clearly shown - more than enough to correctly interpret everything with basic knowledge about EP flux.

Thank you for your comment. Following the reviewer's suggestion, we made all figures divided by air density except for Fig. 2, because the EPF for the CGWs in Fig. 2 divided by air density was too strong in the upper stratosphere. [Figs. 5, 7, and 11]

19) p.12, l.369-374: This belongs in the methods section

We moved the statements to the methods section (Sect. 2.5). [p. 7, L190–198]

20) Fig. 8(c-d): I suggest to, apart from making the c-d plot smaller, put the timeseries next to each other, or even merge them into one continuous timeseries.

Thank you for your suggestion. We merged Figs. 8c and 8d into one continuous timeseries. [Fig. 8]

21) p.13, l.379-380: You may easily add a climatology line into Fig. 8(c-d)

Following the reviewer's suggestion, we added a climatology line with ±1 standard deviation range in Fig. 8c. [Fig. 8]

22) p.13, l.381: Could the authors perhaps provide a daily timeseries of MRG EPD (in the boxed region) to compare with the q timeseries to assess this as a source? Would be a nice addition as Fig. 8(e-f)

Thank you for the good suggestion. Following the reviewer's suggestion, we added the daily EPD time series for the MRG waves as a new figure Fig. 8d, and included a discussion that the magnitude of the positive EPD increases as the number of grids with $\bar{q}_\phi < 0$ increases. [Fig. 8; p. 13, L406–407]

23) Fig. 9: I suggest to translate the y-axis unit (mean rain rates) into something more relatable, e.g. mm/day

Thank you for the good point. The unit is changed to "mm day^{-1}" in the revised manuscript. [Fig. 9]

24) p.14, l.417-419: This was linked by Li et al. (2020) to the El Nino event that winter. Perhaps it would be useful to add a discussion somewhere in this section, about the overall increase in eq. wave activity and precipitation together with El Nino.
Also a mention to Barton and McCormack (2017) could be added.

Thank you for your suggestion! We included a discussion on the enhanced Kelvin wave activity related to the El Niño event and the overall enhancement in the equatorial wave activity by referring to Li et al. (2020). We did not include a paper by Barton and McCormack (2017) here because as far as we know, their focus was not on the equatorial waves but on the midlatitude Rossby waves and their equatorward propagation. [p.15, L447–449]

25) p.14, l.440-442: There is a lot of new information and little justification about the source level here, I suggest you detail more about this in the methods section, and refer to the corresponding methods section when you start with this figure.

Following the reviewer's suggestion, we included the details about the source level in the method section (Sect. 2.3) by including a new figure (Figure S1) and refer to them when we started to describe Fig. 12 in the revised manuscript. The changes in the direction of the vertical EPF and the sign of the EPD appear at 150 hPa and below (140 hPa and above) for H_e (H_w) waves. Our focus is on the westward waves, so we simply assumed the source level of $H_e + H_w$ as 140 hPa. [p.6, L160–162; p.15, L471]

26) p.15, l.446: A non-expert will need more explanation about the source level to understand the attribution made in this sentence. Again, this could be already detailed in the methods section and referred to here.

As discussed in the Comment #25, we included more explanation in the methods section. [p.6, L160–162; p.16, L475]

27) Figure 13 and p.15, l. 447-460: I don't doubt the validity of your results and conclusions regarding Fig. 13, but it would be much easier to interpret if you showed the same plots for He and Hw separately. Mixing both makes this figure a bit confusing. Separating He and Hw will allow the reader to identify which fraction deviates more from climatology (and gets filtered by the wind shear) in a more straightforward way.

We plotted Fig. 13 mimicking the phase-speed spectrum of the GW parameterization (e.g., Fig. 1 of Beres et al. 2004; Fig. 2 of Kang et al., 2017) which, together with wind profiles, can well

represent the sign and magnitude of the potential GWD. Therefore, we would like to keep Fig. 13 as the original. We understand that some readers might be confused and there could be an offset between eastward and westward waves, so we provided the same figure as Fig. 13 but for the eastward and westward propagating parts separately, in the revised supplement (Figure S9). Please note that the figure is not separated into H_e and H_w but into the eastward and westward waves. This is because we defined H_e where $k > 0$ and H_w where $k < 0$ based on the assumption that the zonal wind is close to zero near the equator, but precisely, the direction of the waves is determined by the wind speed at the altitude where the waves are generated (i.e., source level). Since we assumed the source level as 140 hPa (please refer to Response #25), the spectrum where the phase speed is greater (smaller) than zonal wind at 140 hPa is defined as eastward (westward) waves. [p.16, L492–493; Fig. S9]

28) p.15, l.462-467: You discuss the Kawatani paper in the next paragraph. Barton and McCormack (2017) showed important ENSO influence on the background winds and momentum fluxes below 30hPa (see e.g. their plots 3 and 4). It would be worth to add it into your discussion.

Following the reviewer's suggestion, we mentioned ENSO influence on the background winds in the revised manuscript referring to Barton and McCormack (2017). However, ENSO influence on the momentum fluxes below 30 hPa in Fig. 4 of Barton and McCormack (2017) is shown for the horizontal component only, while IG waves have dominant vertical component. Therefore, no further discussions regarding to the work by Barton and McCormack (2017) are made. [p.16, L502–504]

29) p.16, l.488-490: Please detail a bit more what convective source and WFRF mean for the non-expert. Convective source spectrum is related to the movement of convection itself, WFRF to the GWs emitted from it, correct?

Yes, it is correct. The convective source spectrum is about the size, magnitude, and moving speed of the convection and the WFRF is about the shape of the GW spectra emitted from the convection, which is related to the vertical configuration of the convective heating, the critical-level filtering, and resonance between the forced mode and natural mode. The combined effect of the two determines the magnitude and spectral shape of the CGW momentum flux at the source level. We included more explanation in the revised manuscript, as suggested. [p.17, L522–526]

30) p.16, l.496: higher static stability at which height range? Intuitively, deeper convection is related to tropospheric instability.

Thank you for your comment! We found that the original statement was somewhat unclear. We included the height range, 200–300 hPa, and modified the sentence more clearly referring to He et al. (2019) in the revised manuscript. According to He et al. (2019), high tropical static stability appears under global warming because of the enhanced surface temperature resulting in a smaller moist adiabatic temperature lapse rate. Please note that 2016 is the warmest year on record for the global-mean surface temperature (GISTEMP Team, 2020). [p.17, L531–533]

31) p.16, l.497: please use relative terms: warmer / colder

Thank you for your suggestion, but the related sentence was removed during the revision process.

32) p.16, l.497-499: Rephrase this sentence to make it clear that El Nino increases overall amount of convection in the tropics. There must be earlier studies (probably mentioned in the Domeisen review paper) providing this relation to say this with more certainty than 'possibly triggered by El Nino'

Thank you for your suggestion. We rephrased the sentence that El Niño increases the overall amount of convection in the tropics referring to Geller et al. (2016) and Kawatani et al. (2019). [p.17, L529–531]

References

Beres, J. J., M. J. Alexander, and J. R. Holton: A method of specifying the gravity wave spectrum above convection based on latent heating properties and background wind. J. Atmos. Sci., 61, 324–337, doi:10.1175/1520-0469(2004)061<0324:AMOSTG>2.0.CO;2, 2004.

Geller, M. A., T. Zhou, and W. Yuan: The QBO, gravity waves forced by tropical convection, and ENSO, J. Geophys. Res. Atmos., 121, 8886–8895, doi:10.1002/2015JD024125, 2016.

GISTEMP Team: GISS Surface Temperature Analysis (GISTEMP), version 4. NASA Goddard Institute for Space Studies. Dataset accessed 2020-09-10 at https://data.giss.nasa.gov/gistemp/, 2020.

He, C., Y. Wang, and T. Li: Weakened impact of the developing El Niño on tropical Indian Ocean climate variability under global warming, J. Climate, 32, 7265–7279, https://doi.org/10.1175/JCLI-D-19-0165.1, 2019.

Response to Reviewer #2's Comments

General Comment:

This paper gives a comprehensive overview of the different wave forcings that act during the 2016 QBO disruption. The paper discusses the effect of wave forcing by extratropical Rossby waves, equatorial waves, and small scale convective gravity waves, and is therefore the most complete description of the QBO disruption so far. The paper is very well written and fits well into the scope of ACP. The paper is recommended for publication after addressing my minor comments as detailed below.

Main Comments:

1) For the spectral analysis time segments of 90 days are used after applying sine and cosine windows at the first and last 30 days. According to Parseval's theorem, this will lead to an underestimation of spectral amplitudes, and, on average, EPF and EPD will be ~30% underestimated. This relatively small effect will not affect the basic results of the paper, but it should be mentioned.

Thank you for pointing out this part. We already recognized that the variance of the 90-day time series becomes two-thirds of the original variance after applying sine and cosine windows at the first and last 30 days, respectively. Therefore, in our calculation, EPF and EPD were multiplied by a scale factor of 3/2, which was not mentioned clearly in the original manuscript. Although no specific sentences on the scaling were given in the paper of Kim and Chun (2015), it was mentioned in a recent paper by Kim et al. (2019). The calculation of the EPF and EPD is clarified in the revised manuscript referring to Kim et al. (2019). [p.5, L148]

2) I am not sure whether the preconditioning of the QBO disruption by MRG EPD and IG EPD in October 2015 is a reliable result. Firstly, the magnitude of EPD is quite small, secondly, the EPD in October 2015 looks different in ERA-Interim, as can be seen in the supplement.

Thank you for asking an important question.

- With regard to your first question, the sum of the MRG and IG wave forcings are found to be ~-0.9 (-1.2) m s^{-1} mon^{-1}, which is ~61% (55%) of the total negative forcing in October

(November) 2015. We think that these magnitudes are considerably larger than what we expect and cannot be negligible.

- As for your second question, we included the time series of zonal wind, zonal wind tendency, and each wave forcing using ERA-I data as a new figure in the supplement (Figure S6). The contribution of each wave forcing to the total negative wave forcing is given in the below table (Table A1). It is found that the sum of MRG wave forcing and IG wave forcing in October (November) 2015 using ERA-I data is ~-1.0 (-1.3) m s^{-1} mon^{-1}, 61% (53%) of the total negative forcing, which is very similar to that using MERRA-2 data, although MRG (IG) wave forcing is somewhat greater (smaller).

Based on the large contribution by MRG and IG waves and its consistency between datasets, we concluded that MRG and IG waves precondition the zonal wind in the early stage of the QBO disruption. Please also refer to the response to the Specific Comment #6. [Fig. S6]

Table A1. The same as Table 1 but using ERA-I data except for the climatology.

2015–16	Oct 2015	Nov 2015	Dec 2015	Jan 2016	Feb 2016	Mar 2016
MRG	-0.7 (41%)	-0.8 (32%)	-0.8 (24%)	-0.9 (18%)	-1.5 (27%)	-1.1 (28%)
IG	-0.3 (19%)	-0.5 (21%)	-0.3 (9%)	-0.1 (2%)	-0.3 (6%)	-0.6 (16%)
Rossby	-0.6 (40%)	-1.2 (47%)	-2.2 (67%)	-4.0 (80%)	-3.7 (67%)	-2.2 (56%)
Kelvin	1.1	0.7	1.0	1.6	1.2	0.9
Rossby-Y	-0.5 (34%)	-1.0 (38%)	-1.9 (58%)	-3.4 (70%)	-3.2 (58%)	-1.9 (48%)
Rossby-Z	-0.1 (6%)	-0.2 (9%)	-0.3 (9%)	-0.5 (10%)	-0.5 (9%)	-0.3 (8%)

Specific Comments:

1) p2, l33: You may want to include more recent work on the effect of the QBO on surface weather and climate, for example Kidston et al. (2015), or Gray et al. (2018).

Kidston, J., A. A. Scaife, S. C. Hardiman, D. M. Mitchell, N. Butchart, M. P. Baldwin, and L. J. Gray (2015), Stratospheric influence on tropospheric jet streams, storm tracks and surface weather, Nat. Geosci., 8, 433-440.

Gray, L. J., J. A. Anstey, Y. Kawatani, H. Lu, S. Osprey, and V. Schenzinger (2018), Surface impacts of the Quasi Biennial Oscillation, Atmos. Chem. Phys., 18, 8227-8247.

Thank you for suggesting more recent works. Those are included in the revised manuscript.

[p.2, L33]

2) p3, l73: The reference Evan et al., JAS, 2012 does not fit here. Evan et al., JAS, 2012 discuss intermediate-scale tropical inertia-gravity waves of horizontal wavelengths in the 5000km range, and not the effect of small scale gravity waves.
This reference should be replaced by Evan et al., JGR, 2012 which is a WRF simulation of the QBO forcing by small scale gravity waves of horizontal wavelengths >270km. In addition to the listed model studies you should also include observational evidence of the effect of small scale gravity waves, for example Ern et al., JGR, 2014.
Evan, S., M. J. Alexander, and J. Dudhia (2012), WRF simulations of convectively generated gravity waves in opposite QBO phases, J. Geophys. Res., 117, D12117, doi:10.1029/2011JD017302.
Ern, M., F. Ploeger, P. Preusse, J. C. Gille, L. J. Gray, S. Kalisch, M. G. Mlynczak, J. M. Russell III, and M. Riese (2014), Interaction of gravity waves with the QBO: A satellite perspective, J. Geophys. Res. Atmos., 119, 2329-2355, doi:10.1002/2013JD020731.

Thank you for pointing out the mistake and suggesting appropriate papers. The reference Evan et al. (JAS, 2012) is changed into Evan et al. (JGR, 2012). We also included observational evidence by Ern et al. (2014) as suggested. [p.3, L73]

3) p3, l88: "All" gravity waves is not correct! As stated in l.82/83, this paper discusses only small scale gravity waves of horizontal wavelengths <100-200km. However, there is also considerable QBO forcing by small scale gravity waves of horizontal wavelengths >200km, as can be seen from Evan et al., JGR, 2012.

We agree with you, but the related sentence was removed during the revision process.

4) p4, l106: On the selection of WQBO cases: Please state more clearly that the definition of the WQBO as used in this paper focuses on QBO situations that are comparable to that of the 2016 QBO disruption. Generally, there should be WQBO periods or WQBO onsets also in other months.

Thank you for your comment. We clarified that there should be WQBO phases in other seasons, but we only focus on NH winter to compare with the QBO disruption case. [p.4, L111–112]

5) p5, l134/135: As EPF is obtained by summing in the spectral space (l.142), applying cosine windows will lead to an underestimation of spectral amplitudes, and also of EPF, and EPD. See Main Comment (1).

As discussed in the Main Comment #1, we included the sentence that EPF is multiplied by a scale factor of 3/2 to conserve its original variance. [p.5, L148]

6) p9, l253/254: I am not sure whether it is a reliable result that IG and MRG would act as a preconditioning at 40hPa in October 2015 before Rossby waves can take effect! Please note that Fig.4b (for MERRA2) and Fig.S5 in the supplement (for ERA-Interim) look quite different! The preconditioning effect that you suggest seems to be much weaker than the differences between the two reanalyses.

Thank you for your comment. Please note that the time series of Fig. S5 in the original supplement (Fig. S7 in the revised supplement) is not for ERA-I but for MERRA-2 averaged over 5°S–10°S. As discussed in the Main Comment #2, the sum of MRG wave forcing and IG wave forcing is quite similar between MERRA-2 and ERA-I data in October–November 2015. The wave forcing by IG waves using ERA-I is somewhat smaller than that using MERRA-2, possibly due to a coarser horizontal resolution (0.75°). The related sentence is included in the revised manuscript. We also clarified in the figure caption that Fig. S5 (Fig. S7 in the revised manuscript) is for MERRA-2 data. [p.10, L306–307; Figs. S6–S7]

7) p10, l281-285: Another reason for this difference could be the part of the gravity wave spectrum that is neither covered by the CGW scheme, nor resolved or parameterized in MERRA2. It should be emphasized that MERRA2 is not a free-running model! There will be model imbalances that are caused by data assimilation. Data assimilation can therefore correct misrepresentations of the gravity wave forcing by the nonorograpic GWD parameterization.

We agree with you that data assimilation corrects misrepresentations of gravity wave forcing by GWD parameterization which could stem from the missing GW spectrum in the parameterization. However, this fact may not be strongly related to the difference between the parameterized GWD from MERRA2 and CGWD from the offline parameterization, because the analysis increment is not included in the parameterized GWD but is provided separately as a different variable named “total eastward wind analysis tendency” in MERRA-2 (GMAO, 2015).

8) Fig.6: Here you identify source regions of Rossby waves by positive EPD coinciding with upward directed EPF. At 15N around 150hPa EPF is directed downward coinciding with negative EPD. Do you think this is another source region of Rossby waves? As EPF is directed downward, it looks like these waves cannot propagate into the stratosphere.

We agree with you, and the related sentence is deleted in the revised manuscript.

9) p11, l327: that the positive EPD region is a source region of the westward-propagating waves. -> that the positive EPD region should be a source region of westward-and upward propagating waves.

Thank you for your suggestion. It is modified. [p.12, L358]

10) p12, l370: It should be mentioned that Eq.(3) includes both barotropic and baroclinic instability. Did you check which term is stronger - the barotropic term (meridional gradients), or the baroclinic term (vertical gradients)? Coy et al., 2017 claimed that barotropic instability would be stronger. In your Fig.8, this does not fit the title and the figure caption saying "baroclinic instability".

Thank you for your suggestion. In the original manuscript, it was mentioned that the $\bar{q}_{\phi}$ term is dominated by the barotropic instability; but it was not highlighted. Figure A1 below shows the same as Figs. 8a–b but excluding the third term in the righthand side of Eq. (3), which is very similar to Figs. 8a–b. This implies that the barotropic term is much larger than the baroclinic term. This result is consistent with the finding of Garcia and Richter (2019), who showed that the reversal of the vorticity gradient was almost completely dominated by the behavior of the barotropic part, specifically by the behavior of the meridional curvature of the zonal wind. We moved explanation of Eq. (3) to the methods section (Sect. 2.5 in the revised manuscript) and stated clearly that the Eq. (3) is dominated by the barotropic instability. Also, “baroclinic instability” in Fig. 8 is changed into “barotropic instability”. [p.7, L198–199; Fig. 8]

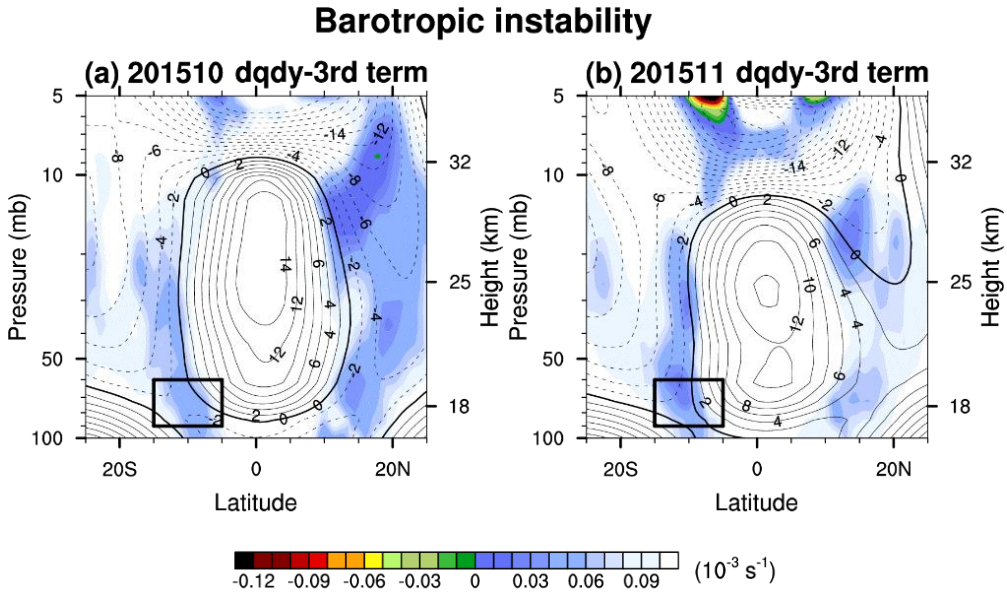

Figure A1. The same as Figs. 8a–b but for $\bar{q}_\phi$ excluding the third term in the righthand side of Eq. (3).

11) p17, l513: barotropic instability -> barotropic and/or baroclinic instability

As discussed in the Specific Comment #11, we stated clearly in the revised manuscript that $\bar{q}_\phi$ term is dominated by the barotropic instability. Therefore, we would like to keep "barotropic instability" here.

Technical comments:

1) p5, l124: the parameter \hat{f} is not used in Eq.(1)

Thank you for pointing out this error! "Eq. (1)" is changed to "F^ϕ and F^z" in the revised manuscript. [p.5, L128]

2) p6, l175: is lower than 700 hPa -> is at altitudes lower than 700 hPa

Thank you! It is corrected. [p.6, L182]

3) Fig.1: colorbar should be m/s, but is m/s/month

Thank you! It is corrected. [Fig. 1]

4) Fig.3: one of the colorbars should refer to the wind in m/s, but both colorbars give

tendencies in m/s/month

Thank you! It is corrected. [Fig. 3]

5) p8, l222: (Fig. 3a) -> (Fig. 3c)

Thank you! It is corrected. [p.8, L244]

6) p9, l256/257: Figure S4 is the same figure with Fig. 3 but using ERA-I data. -> Figure S4 shows the same as Fig. 3 but using ERA-I data.

It is modified as suggested. [p.10, L283]

7) p9, l264: (Fig. 4c) -> (Fig. 4a, dotted line)

Thank you! It is corrected. [p.10, L291]

8) caption of Fig.7, l795: (c) January 2016, -> (c) December 2015

Thank you! It is corrected. [Fig. 7]

9) caption of Fig.7, l799: where the EPD is smaller than -> where the EPD is stronger than

Thank you for pointing out the ambiguous expression. It is changed to “where the EPD is algebraically smaller (more negative) than the climatology”, not only in the caption of Fig. 7 but also in that of Figs. 5 and 11 for consistency. [Figs. 5, 7, 11]

10) p13, l390: affects -> affect

Thank you! It is corrected. [p.14, L417]

11) caption of Fig.9, p35, l814: January 2016, and (b) -> January 2016, and (d)

Thank you! It is corrected. [Fig. 9]

References

Global Modeling and Assimilation Office (GMAO): MERRA-2 tavg3_3d_udt_Np: 3d,3-Hourly,Time-Averaged,Pressure-Level,Assimilation,Wind Tendencies V5.12.4, Greenbelt, MD, USA, Goddard Earth Sciences Data and Information Services Center (GES DISC), accessed 28 September 2020, 10.5067/CWV0G3PPPWFW, 2015.

Kim, Y.-H., Kiladis, G.N., Albers, J.R., Dias, J., Fujiwara, M., Anstey, J.A., Song, I.-S., Wright,

C.J., Kawatani, Y., Lott, F. and Yoo, C.: Comparison of equatorial wave activity in the tropical tropopause layer and stratosphere represented in reanalyses. Atmos. Chem. Phys., 19, 10027–10050, 2019.

Response to Reviewer #3's Comments

General Comment:

Summary: This paper provides a detailed examination of the equatorial wave structures and their evolution during October 2015 through February 2016, a time when the quasi-biennial oscillation experienced a significant disruption. This investigation, based on MERRA-2, a global assimilation system, breaks down the wind, temperature, and precipitation fields into Rossby, Mixed Rossby Gravity (MRG), inertia-Gravity (IG), and Convective Gravity (CG) waves. A novel aspect of this work is the use of a convective gravity wave parameterization to calculate the CG wave effects. The different Eliassen Palm (EP) fluxes and their divergences are evaluated. Quantities calculated for the QBO disruption are compared to their corresponding climate signatures. The results show how during October-November of 2015 MRG and IG waves acted to precondition the QBO winds before the strong Rossby waves that occurred in 2016 and created the anomalous QBO easterlies. Why these waves were stronger than usual during this time is still unknown.

Strengths: This work provides a comprehensive view of the UT/LS equatorial waves during the QBO disruption. It expands on the work of Lin et al. (2019) by including aspects of the tropospheric forcing by precipitation and the addition of CG wave model and also differs in the choice of assimilation system from Lin et al. (2019). Figure 16 provides an especially useful summary of the changes roles played by the different waves.

Weaknesses: No major weaknesses. There are a few points that could be improved for clarity that are detailed below. There are a large number of figures. These provide a comprehensive record but it can be difficult for readers to locate the features of interest as described in the text.

Recommendation: Publish after minor revisions noted below. This is a well written, well organized, manuscript. The figures are appropriately captioned and the abstract accurately summaries the work. The topic should be of interest to many readers of ACP interested the the QBO and equatorial waves.

Comments:

1) Line 44: "El Nino" Coy et al. (2017) only mentioned a possibility of an ENSO connect. The terms El Nino or ENSO are not found in Osprey et al. (2016) so this sentence should be rewritten.

Thank you for pointing this out! The reference by Osprey et al. (2016) is deleted in the revised manuscript.

2) Line 58: Should be "Coy et al. (2017)". There is a Coy et al. (2016) describing the MERRA-2 QBO before the disruption that could probably be mentioned somewhere in the data section: Coy, L., K. Wargan, A. M. Molod, W. R. McCarty, and S. Pawson. 2016. "Structure and Dynamics of the Quasi-Biennial Oscillation in MERRA-2." J. Climate, 29:14: 5339-5354 [10.1175/jcli-d-15-0809.1]

Thank you for pointing out this error! It is corrected. [p.2, L58]

3) Line 67: Each MERRA-2 data set has a DOI number that researchers are encouraged to reference and clarifies exactly what data set was used. For example from https://disc.gsfc.nasa.gov/datasets/M2I3NVASM_5.12.4/summary?keywords=%22MERRA-2%22 To cite the data in publications: Global Modeling and Assimilation Office (GMAO) (2015), MERRA-2 inst3_3d_asm_Nv: 3d,3-Hourly,Instantaneous,Model-Level,Assimilation,Assimilated Meteorological Fields V5.12.4, Greenbelt, MD, USA, Goddard Earth Sciences Data and Information Services Center (GES DISC), Accessed: [Data Access Date], 10.5067/WWQSXQ8IVFW8

Thank you for your important point. We added MERRA-2 data reference in the revised manuscript. [p.3, L68]

4) Lines 248-249: How is the budget formulated so that resolved MRG and IG wave forcing acts to "enhance" the momentum budget residual, REQ? Maybe this could be rewritten for clarity.

Thank you for your good comment. We found that the original sentence was unclear. We intended to say that the strong MRG and IG wave forcing may account for the relatively strong negative REQ in November 2015. We changed the sentence as follows: “IG waves exert a strong negative forcing in November 2015, which might be related to the enhancement of

negative REQ at 40 hPa along with the MRG wave forcing". [p.9, L272–273]

5) Lines 277-287: This is a good discussion of the CGWD. It would help to see the vertical zonal mean zonal wind shear at 40 hPa as a part of Fig. 4 as that should determined in large part the GWD forcing. In addition the meridional shear of the zonal mean zonal wind across the equator might correspond to the changes in the Rossby wave forcing and be helpful to see plotted.

Thank you for your good suggestion. During the revision process, we plotted meridional wind shear across the equator and vertical wind shear averaged over 5°N–5°S, which are included as a new figure (Fig. 4d) in the revised manuscript. We found that the temporal evolution of CGW (Rossby wave) forcing is similar to that of vertical (meridional) wind shear. The related discussion is included in the revised manuscript. [p.10, L303–306]

6) Lines 357-362: Figures 3, 4, and 7 all illustrate aspects of MRG waves, however it is difficult to put together a consistent picture of support for the mid-jet easterly acceleration described here. Most of the easterly acceleration appears to take place in the regions of strong wind shear, not mid-jet. In particular the contribution from MRG waves in Fig. 4 at 40 hPa is small and appears nearly constant in time. The mid-jet should be identified more quantitatively and MRG wave aspects calculated with respect to the jet at each month, at least for the earlier months, to justify this conclusion.

Thank you for your comment. Although the MRG wave forcing is generally strong in the regions of strong wind shear, the easterly acceleration by the MRG waves in the mid-jet (5°N–5°S) is evident at 40 hPa in October, November, and December 2015 with magnitudes of -0.4, -0.6, and -0.6 m s^{-1} mon^{-1}, respectively (Table 1). The magnitude of mid-jet in 5°N–5°S is 12.3, 11.1, and 8.2 m s^{-1} in October, November, and December, respectively (Figure 4a), which implies that the MRG wave forcing can at least partly account for the weakening of the mid-jet. During the revision process, we additionally plotted a time–latitude cross section of the MRG wave forcing at the altitude range of 40–60 hPa, where the MRG wave forcing was strong (Figure A2), which also shows a deceleration of the jet core by the MRG waves in the early period. The related discussion is included in the revised manuscript. [p.13, L389–390]

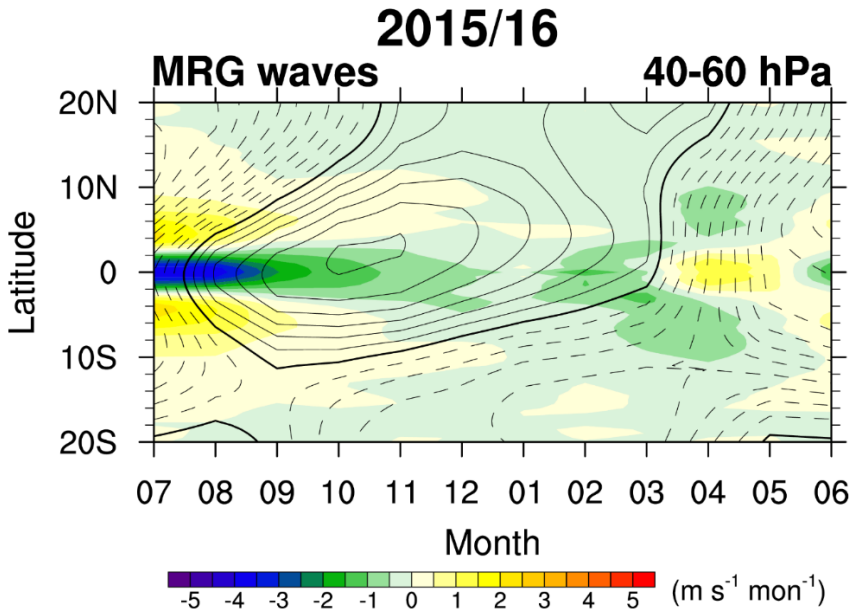

Figure A2. Time–latitude cross section of EPD for the MRG waves at 40–60 hPa, superimposed with the zonal-mean zonal wind (contour lines). Positive (negative) zonal winds are plotted with solid (dashed) lines with a contour interval of 2 m s^{-1}, and thick contour lines denote a zero-zonal wind speed.

7) Lines 375-392: This instability analysis is based on zonal mean winds. A stronger case for instability might be possible with non-zonally average winds, especially when the focus is on the relatively small region defined by the box in Figure 8.

Thank you for your comment. We found that the number of grids with $\bar{q}_\phi < 0$ is much larger than the original calculation when calculating baroclinic instability based on each longitudinal grid (Figure A3). However, we thought that the background flow defined to extract the MRG waves should be used to evaluate baroclinic instability as a possible source of the MRG waves. Therefore, we would like to keep the calculation of $\bar{q}_\phi$ based on zonal averages.

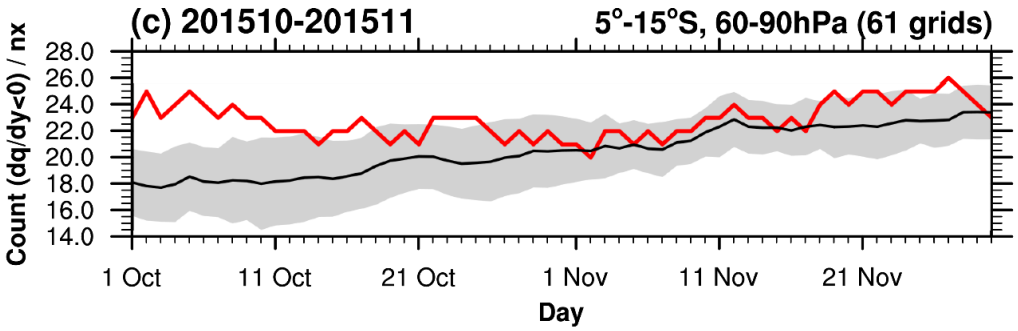

Figure A3. The number of grids where daily-mean $\bar{q}_\phi$ (s^{-1}) in each longitude is negative in the boxed region (5°–15°S, 60–90 hPa) normalized by the number of longitudes (nx = 576) in October–November 2015 (red) and its climatology with ±1 standard deviation (gray shading).

8) Lines 443-485: The "...apparent positive wind shear..." Is difficult to find in Fig. 14a.The specific levels should be specified in the text.

Thank you for your comment. The specific levels (140–200 hPa) are included in the revised manuscript. [p.17, L515–516]

9) Lines 499-502: The white and gray curves described in the text appear to be different from the Fig. 15 caption description.

Thank you. The description on the gray curves is modified in the revised manuscript. [p.17, L534]

Minor Comments:

1) Line 375: The units in Fig. 8 suggest that q_y is plotted not q_phi. This is a small point. Perhaps the units could be described in the figure caption.

Thank you for pointing out the error! The unit is corrected and described in the figure caption. [Fig. 8]

2) Lines 732-733: The year is missing from the reference.

Thank you, but we think the year '2011' was included in the original manuscript.

Response to Reviewer #4's Comments

General Comment:

The authors investigated the relative contribution of each resolved wave and parameterized waves to the QBO disruption in 2015-2016. They have shown that MRG and westward IG weakened the QBO and then led to extratropical Rossby breaking at the QBO jet core at 40 hPa. They also investigated the roles of CGWs obtained from an offline CGW parameterization that author's group has developed and showed the importance of variable wave sources. There have been several studies to investigate the mechanism of the 2015-2016 QBO disruption. I think this paper is the most comprehensive study among them. I believe this paper is suitable for the publication in ACP. My recommendation is published after very minor revision. I have a few comments added below.

Comments:

1) MRG are confined to the range |k|<=20 and omega <0.75 cpd in the symmetric spectrum. I think zonal |k|<=20 is a little wide for the MRG. Presumably |k|<=~10 would be better. Westward IGWs should be included in this definition. How much do the results depend on the ranges of |k|? I guess the relative contribution of MRG, shown in Table 1 and Figure 4, would be changed. One good point to answer this concern is to mention the dominant zonal wavenumber ranges for the MRG to force the QBO. I guess 3 < k < 6, but am not sure. I would suggest authors at least to mention the dependence of |k| selection to the quantitative results.

Thank you for your comment! The MRG waves are confined to the spectral range where the signs of F^{z1} and F^{z2} are the opposite within $|k| \leq 20$ and $0.1 \leq \omega \leq 0.5$ cpd in the anti-symmetric spectrum (Kim and Chun 2015, JGR). Here, the F^{z1} and F^{z2} represent the first and second terms of the vertical EPF (F^z). This range is basically within $|k| \leq 10$ as seen in the example of the MRG wave spectrum in Figure A4, which is similar to what the reviewer expected. During the revision process, we performed a sensitivity test on the EPD for the MRG waves by changing the spectral boundary of the MRG waves as $|k| \leq 10$ and $0.1 \leq \omega \leq 0.5$ cpd in the anti-symmetric spectrum. It is found that the EPDs of the MRG waves in October

and November 2015 are -0.437 and -0.5883 m s^{-1} mon^{-1} (originally: -0.433 and -0.5876 m s^{-1} mon^{-1}), respectively, implying that the difference is within 1%. The dominant zonal wavenumber ranges for MRG waves are mentioned in the revised manuscript. [p.5, L144–145]

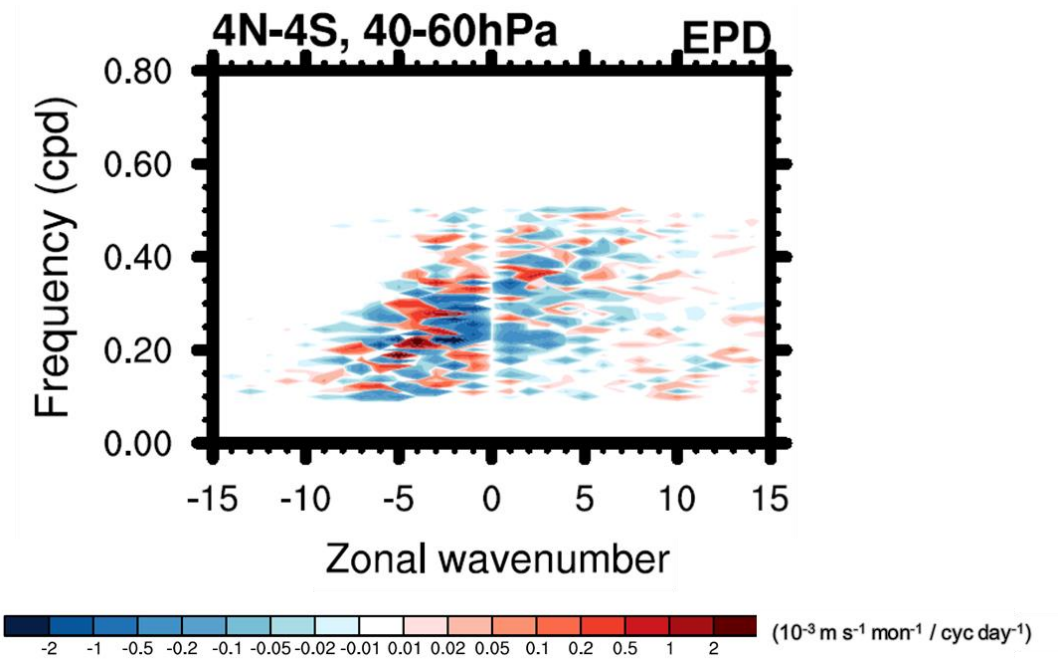

Figure A4. Spectral density of the EPD for the MRG waves averaged over 4ºN–4ºS at 40–60 hPa in November 2015.

2) L216: "The required wave forcing term (REQ) is calculated as a residual by subtracting the advection terms from the zonal wind tendency in the TEM equation"
When calculating REQ, do the authors consider the first term on the left of Eq. (1), that is meridional advection term, which is normally very small near the equator? In my experiences, the meridional advection term has also some values off the equator even at ~5 degrees, which cannot be sometimes negligible.

Yes, we also consider the meridional advection term, so the REQ is calculated as a residual by subtracting both the meridional and vertical advection terms from the zonal wind tendency. It is clarified in the revised manuscript. [p.8, L239]

3) L258: "although the magnitudes of the REQ and wave forcing (vertical advection) in ERA-I is generally stronger (weaker) than that in MERRA-2" I guess one possible reason for this is the different values of w* between MERRA-2 and ERA-I. As you know, the representation of BDC is quite different quantitatively among reanalyses as the S-RIP

project has indicated.

We agree with you. As the reviewer mentioned, $\bar{w}^*$ value in the reanalysis is well known for its large spread. In addition to the differences in $\bar{w}^*$, a large spread in the vertical wind shear, which is generally related to the vertical resolution of the data, is also a possible reason for the discrepancy in the vertical advection term, which is supported by Figure 5 of Kim and Chun (2015, ACP). The related discussion is included in the revised manuscript. [p.10, L285–286]

4) I would suggest to refer the paper by Dunkerton (2016, GRL, https://doi.org/10.1002/2016GL070921). Dunkerton's paper, published just after the QBO disruption, discussed some presumable mechanisms, which would be now useful for the current study.

Thank you for suggesting a paper. The paper by Dunkerton (2016) is now included in the revised manuscript. [p.2, L44]

5) Figure 4(c): The explanation lines of Rossby-Y & Rossby-Z are hard to see. Please expand the lines.

Thank you for pointing this out! The explanation lines in Figure 4c are expanded in the revised manuscript. [Fig. 4]

References

Kim, Y.-H., and H.-Y. Chun: Momentum forcing of the quasi-biennial oscillation by equatorial waves in recent reanalyses. Atmos. Chem. Phys., 15, 6577–6587, doi:10.5194/acp-15-6577-2015, 2015.

Role of equatorial ~~planetary~~waves and convective gravity waves in the 2015–16 quasi-biennial oscillation disruption

Min-Jee Kang[1], Hye-Yeong Chun[1], and Rolando R. Garcia[2]

[1]Department of Atmospheric Sciences, Yonsei University, Seoul, South Korea
[2]National Center for Atmospheric Research, Boulder, Colorado, USA

Correspondence to: Hye-Yeong Chun (chunhy@yonsei.ac.kr)

Abstract. In February 2016, the descent of the westerly phase of the quasi-biennial oscillation (QBO) was unprecedentedly disrupted by the development of easterly winds. Previous studies have shown that extratropical Rossby waves propagating into the deep Tropics were the major cause of the 2015–16 QBO disruption. However, a large portion of the negative momentum forcing associated with the disruption still stems from equatorial planetary and small-scale gravity waves, which calls for detailed analyses by separating each wave mode compared with climatological QBO cases. Here, the contributions of resolved equatorial planetary waves [Kelvin, Rossby, mixed-Rossby gravity (MRG), and inertia-gravity (IG) waves] and small-scale convective gravity waves (CGWs) obtained from an offline CGW parameterization to the 2015–16 QBO disruption are investigated using MERRA-2 global reanalysis data from October 2015 to February 2016. In October and November 2015, anomalously strong negative forcing by MRG and IG waves weakened the QBO jet at 0°–5°S near 40 hPa, leading to Rossby wave breaking at the QBO jet core in the southern hemisphere. From December 2015 to January 2016, exceptionally strong Rossby waves propagating horizontally (vertically) continuously decelerated the southern (northern) flank of the jet. In February 2016, when the westward CGW momentum flux at the source level was much stronger than its climatology, CGWs began to exert considerable negative forcing at 40–50 hPa near the equator, in addition to the Rossby waves. The enhancement of the negative wave forcing in the Tropics stems mostly from strong wave activity in the troposphere associated with increased convective activity and the strong westerlies (or weaker easterlies) in the troposphere, except that the MRG wave forcing is more likely associated with increased barotropic instability in the lower stratosphere.

1 Introduction

The quasi-biennial oscillation (QBO) is the dominant source of variability in the equatorial stratosphere, characterized by alternating easterly and westerly winds with a period of around 28 months (Baldwin et al., 2001). Based on the classical theory, the QBO is generated by momentum deposition by vertically propagating equatorial planetary and gravity waves (Lindzen and Holton, 1968; Holton and Lindzen, 1972). The impact of the QBO is not limited to the tropical stratosphere; the QBO modulates the strength of tropospheric convection (Collimore et al., 2003; Liess and Geller, 2012; Lee et al., 2019), Madden–Julian Oscillation (Yoo and Son, 2016; Marshall et al., 2017), and the tropical cyclone tracks (Ho et al., 2009). In addition, the

QBO affects not only the subtropical jet and the subsequent changes in the growth and life cycle of the synoptic-to-planetary scale waves in the troposphere (Garfinkel and Hartmann, 2011), but also the intensity of the stratospheric polar vortex (Holton and Tan, 1980; Anstey and Shepherd, 2014), which is strongly tied to the surface temperature and pressure distribution in the extratropics (Baldwin and Dunkerton, 2001; Kidston et al., 2015; Gray et al., 2018). The meridional circulation induced by the QBO also changes the transport of chemical species such as ozone (Randel and Wu, 1996), water vapor (Giorgetta and Bengtsson, 1999), methane (Patra et al., 2003), etc. Therefore, understanding the QBO is important for improving short- and long-range forecasts due to its quasi-periodical nature and global impact (Boer and Hamilton, 2008; Scaife et al., 2014).

In February 2016, sudden development of easterly winds in the middle of the westerly phase of the QBO (40 hPa) interrupted the normal descent of the westerly phase, which was the first such occurrence since QBO observations started in 1953 (Osprey et al., 2016; Newman et al., 2016). This phenomenon is called the 2015–16 QBO disruption. None of the seasonal forecast models predicted the QBO disruption (Osprey et al., 2016), while reproducing the QBO disruption was possible only by a JAGUAR (Japanese Atmospheric General circulation model for Upper Atmosphere Research; Watanabe and Miyahara, 2009) model initialized in January 2016 (Watanabe et al., 2018). A series of studies have shown that the major cause of the QBO disruption was strong equatorward-propagating Rossby waves from the extratropics. Those studies suggested that extratropical Rossby wave generation was enhanced due to a strong El Niño (~~Osprey et al.,~~Dunkerton, 2016; Coy et al., 2017) and low Arctic sea-ice concentration (Hirota et al., 2018). Furthermore, anomalous westerlies in the subtropical lower stratosphere, possibly caused by El Niño and the seasonal timing (Barton and McCormack, 2017), enabled the Rossby wave flux to refract toward the equatorial stratosphere.

However, there have been several cases in which the QBO disruption did not occur despite the presence of westerly winds in the subtropical lower stratosphere and strong Rossby wave flux propagating into the equator from the Northern Hemisphere (NH) extratropics (e.g., cases in 2010/11). This is consistent with the fact that the extratropical Rossby waves generally decelerate the edge of the QBO jet, not the jet core (O'Sullivan, 1997). Thus, it is unclear how the Rossby waves decelerate the QBO jet core during the 2015–16 QBO disruption. Regarding this question, Lin et al. (2019) have shown that strong extratropical waves in a confined longitude region could make a local critical layer for the Rossby waves to break in the middle of the QBO jet. They also argued that high-frequency waves, mainly the mixed-Rossby gravity (MRG) waves, slowed down the background wind, which facilitates the formation of a local critical layer. This result suggests that negative momentum forcing by equatorial waves ~~is the prerequisite for~~preconditioned the extratropical Rossby wave breaking, which motivates the current study to investigate the role of each equatorial ~~waves to~~wave mode in the QBO disruption from early to later stages.

Coy et al. (~~2016~~2017) showed that about half of the negative momentum forcing required for the QBO disruption in February 2016 can be explained by the horizontal component of Eliassen–Palm flux (EPF) divergence (EPD), which is largely attributed to the Rossby waves that propagate from the extratropics. They mentioned that further analyses on the vertical component of the EPD are necessary given that the vertical EPF in the tropical region significantly increased during the

disruption. Barton and McCormack (2017) also recognized the non-negligible contribution of the vertical EPD, but no systematic analysis on the equatorial wave forcing has been undertaken since then.

In the present study, we examine the contributions of equatorial planetary waves, including equatorial Kelvin, Rossby, MRG, and inertia-gravity (IG) waves, and small-scale convective gravity waves (CGWs), to the 2015–16 QBO disruption by employing the separation method of equatorial wave modes of Kim and Chun (~~2015~~2015a) and the offline CGW parameterization by Kang et al. (2017) using the Modern-Era Retrospective Analysis for Research and Applications version 2 (MERRA-2) reanalysis data (Gelaro et al., 2017) on native model levels~~.~~ (GMAO, 2015). This is the first study to classify the equatorial waves in detail and investigate each wave's role in the QBO disruption. Note that if the EPD is calculated without separating each wave mode, the importance of the westward-propagating waves might be obscured by the eastward-propagating waves, given that Kelvin wave activity was enhanced during the 2015–16 QBO disruption (Kumar et al., 2018; Li et al~~.~~., 2020). The second new aspect of this study is to investigate the role of small-scale CGWs. Generally, small-scale CGWs have been recognized as an important driver of the easterly QBO (Kawatani et al., 2010; Evan et al., 2012; Ern et al., 2014; Kim and Chun, ~~2015~~2015a), but this has not been examined comprehensively in terms of the QBO disruption, except by Coy et al. (~~2016~~2017), who analyzed the role of the parameterized gravity wave drag (GWD) provided by MERRA-2, and by Watanabe et al. (2018), who simulated the QBO disruption with JAGUAR model resolving IG waves of horizontal wavelength longer than ~200 km. However, the parameterized GWD data provided by MERRA-2 are the combination of the orographic and non-orographic GWDs, where the non-orographic GW parameterization assumes a latitudinally dependent GW source momentum flux without considering GW sources explicitly; thus, understanding the linkage between the convective source and the wave forcing was somewhat difficult. In particular, the QBO disruption took place during a strong El Niño phase, implying that CGW activity could be much stronger than the climatology. To overcome the simplicity of the non-orographic GW parametrization in MERRA-2 and the inevitable restriction on the horizontal resolution, in this study, we provide a realistic estimate of small-scale wave drag due to CGWs ($\lambda_h < 100$–200 km, where λ_h is the horizontal wavelength) by using an offline, convectively coupled GW parameterization (Kang et al., 2017). The magnitude of the CGW momentum flux is constrained by observational data from the super-pressure balloons ~~(SPBs)~~ in the tropical region (Jewtoukoff et al., 2013), which is the only tropical in-situ observation covering small-scale GWs ($\lambda_h < 100$ km).

~~The aim of this paper is to provide a comprehensive picture of the 2015–16 QBO disruption, examining the contribution of all equatorial planetary and gravity waves.~~In this study, we first examine the extent to which each equatorial wave contributes to the momentum budget during the QBO disruption. After determining how much wave forcing was anomalous compared to the climatology, we investigate the possible cause of the anomalous wave forcing during the QBO disruption. Section 2 of the paper describes the data and methods used in this study. In Section 3 ~~presents~~, general characteristics of zonal wind and equatorial waves during the ~~main results,~~QBO disruption are presented (Sect. 3.1) including quantitative estimates of momentum forcing by equatorial waves ~~and the~~(Sect 3.2). The detailed wave structures and their sources ~~of each wave.~~are

discussed for Rossby waves and MRG waves (Sect. 3.3), inertia-gravity waves (Sect. 3.4), and small-scale CGWs (Sect. 3.5).

Section 4 provides a summary of our findings followed by concluding remarks.

2 Data and Methods

2.1 Data

In this study, we use output from MERRA-2 for 37 years (from 1980 to 2016) provided on a 0.625° longitude by 0.5° latitude regular grid at 3-h intervals. We employ native model-level data for accuracy in estimating both resolved and parameterized wave forcing, especially for the equatorial waves having relatively short vertical wavelengths (e.g., MRG waves; Richter et al., 2014). The model-top pressure is 0.01 hPa with 72 layers in total including 14 layers from 100 to 10 hPa. We utilize zonal wind, meridional wind, temperature, geopotential height, air temperature tendency due to moist processes (DTDTMST), large-scale rainfall, and convective rainfall. In addition to MERRA-2, output from the European Centre for Medium-Range Weather Forecasts (ECMWF) interim reanalysis (ERA-I; Dee et al., 2011) with a horizontal resolution of 0.75° at 6-h intervals from 2015 to 2016 is used to examine the sensitivity of resolved wave forcing on the reanalysis datasets. The 3-hourly precipitation data from Tropical Rainfall Measuring Mission (TRMM) 3B42 version 7 (Huffman et al., 2014) for 19 years (1998–2016) with a horizontal resolution of 0.25° are also used to confirm the precipitation variability in MERRA-2. For validating convective heating rate data estimated from MERRA-2 (Sect. 2.4), which are input data for CGW parameterization, gridded convective stratiform heating (GCSH) estimated from Global Precipitation Measurement (GPM) observations (GPM Science Team, 2017; Lang and Tao, 2018) are used.

Here, we define a westerly QBO (WQBO) phase when the zonal wind anomaly from the monthly climatology divided by its standard deviation exceeds +0.5 both at 30 hPa and 50 hPa for at least 4 months during the 6 months from October to March, the month when the QBO disruption develops. It should be noted that there exist WQBO phases in other seasons as well, but we focus on the NH winter to compare with the 2015–16 QBO disruption. Based on this definition, 10 winters among 37 years are selected: 1980–81, 1982–83, 1985–86, 1987–88, 1990–91, 1999–2000, 2006–2007, 2008–09, 2010–11, 2013–14. The average of those 10 winters will be referred to ~~WQBO~~as the climatology hereafter.

2.2 Transformed Eulerian-mean (TEM) momentum equation

We use the transformed Eulerian-mean (TEM) zonal momentum equation in log-pressure coordinates (Andrews et al., 1987) to examine the zonal wind acceleration, resolved wave forcing, and the vertical advection:

$$\frac{\partial \bar{u}}{\partial t} = \left(f - \frac{1}{a\cos\phi}\frac{\partial}{\partial \phi}(\bar{u}\cos\phi) \right)\bar{v}^* - \bar{w}^*\frac{\partial \bar{u}}{\partial z} + \frac{1}{\rho_0 a\cos\phi}\nabla\cdot F + \bar{X}\,, \qquad (1)$$

Here, a, u, and ρ_0 are the radius of the Earth, zonal wind, and air density, respectively. The overbar and prime indicate the zonal average and the perturbation from it, respectively. The EPF, expressed as $F \equiv (0, F^{\phi}, F^{z})$, is composed of meridional $[F^{\phi} = \rho_0 a \cos\phi\,(-\overline{u'v'} + \bar{u}_z \overline{v'\theta'}/\bar{\theta}_z)]$ and vertical $[F^{z} = \rho_0 a \cos\phi(\hat{f}\overline{v'\theta'}/\bar{\theta}_z - \overline{u'w'})]$ components, and its divergence (EPD) is calculated as follows:

$$\frac{1}{\rho_0 a \cos\phi}\nabla \cdot F = \frac{1}{\rho_0 a \cos\phi}\left[\frac{1}{a\cos\phi}\frac{\partial}{\partial\phi}\left(F^{\phi}\cos\phi\right) + \frac{\partial F^{z}}{\partial z}\right]. \quad (2)$$

In ~~Eq. (1),~~ F^{ϕ} and F^{z}, $\hat{f}$ is the modified Coriolis parameter defined by $\hat{f} = f - 1/(a\cos\phi)\,\partial/\partial\phi\,(\bar{u}\cos\phi)$ where f is the Coriolis parameter, and $\bar{v}^*$ and $\bar{w}^*$ are the residual meridional and vertical velocities defined by $\bar{v}^* = \bar{v} - {\rho_0}^{-1}(\rho_0 \overline{v'\theta'}/\bar{\theta}_z)_z$ and $\bar{w}^* = \bar{w} + (a\cos\phi)^{-1}\left(\cos\phi\,\overline{v'\theta'}/\bar{\theta}_z\right)_{\phi}$, respectively. $\bar{X}$ in Eq. (1) represents forcing by processes other than EPD, including parameterized GWD. Although MERRA-2 provides GWD, it is not coupled with the variation of the convection. Therefore, we calculated physically based and convection-dependent GW parameterization offline (Kang et al., 2017; 2018), which will be described in Sect. 2.4.

2.3 Classification of the equatorial wave modes

We separate equatorial waves into Kelvin, Rossby, MRG, and IG waves using the method proposed by Kim and Chun (~~2015~~2015a) with MERRA-2 reanalysis data. Here, we briefly describe the way to separate each wave component, while the details can be found in Section 4 of Kim and Chun (~~2015~~2015a). First, all the perturbation variables constituting the EPF are divided into symmetric and anti-symmetric components with respect to the equator for a 90-day segment after applying sine and cosine windows at the first and last 30 days, respectively. Second, a two-dimensional Fourier transform is performed on the perturbation variables with respect to longitude and time to obtain their zonal wavenumber–frequency ($k - \omega$) spectra at each latitude and height from 30°N to 30°S and 100 hPa to 5 hPa. Kelvin waves are confined to the spectral range of $0 < k \leq 20$ and $\omega < 0.75$ cycle per day (cpd) in the symmetric spectrum in the latitude range where $|F^{z1}| < |F^{z2}|$. Here, F^{z1} and F^{z2} represent the first and second terms of the vertical component of EPF (F^{z}), respectively. MRG are confined to the range $|k| \leq 20$ and $0.1 \leq \omega \leq 0.5$ cpd in the anti-symmetric spectrum within the latitude range where $F^{z1} \times F^{z2} < 0$. Generally, the dominant zonal wavenumbers for MRG waves are $|k| \leq 10$. The spectral ranges that are not classified as Kelvin or MRG waves, are defined as Rossby waves for the ranges $|k| \leq 20$ and $\omega \leq 0.4$ cpd, and IG waves otherwise. Finally, EPF and EPD calculated at a given k and ω are summed over the spectral range of each wave mode using Parseval's relation (Horinouchi et al., 2003~~).~~), and multiplied by a scale factor of 3/2 to conserve the original variance (Kim et al., 2019). Note that the westward waves (intrinsic frequency < 0) propagate in the same direction as the EPF vectors, whereas the eastward waves (intrinsic frequency > 0) propagate in the opposite direction of the EPF vectors (Andrews et al., 1983). Therefore, given the dominant

upward propagation in the stratosphere, EPF vectors for the Rossby, MRG, westward IG waves are directed upward, whereas those for the Kelvin waves and eastward IG waves are directed downward.

In the troposphere, the abovementioned method is not suitable for classifying each wave mode (Kim and Chun, ~~2015~~2015a), because the source of the stratospheric equatorial waves, such as convection, contaminates the F^{z1} and F^{z2}. Therefore, we instead apply very simple criteria to separate the wave spectrum below 100 hPa as follows: In the frequency range of $\omega \leq 0.4$ cpd, the perturbation variables in the ranges of $0 < k \leq 20$ and $-20 \leq k < 0$ are defined as low-frequency eastward (L_e) and westward (L_w) waves, respectively, which approximately represent Kelvin and Rossby waves, respectively. The variables in the spectral ranges of (i) $k > 20$ or (ii) $0 < k \leq 20$ and $\omega > 0.4$ cpd and those of (i) $k < -20$ or (ii) $-20 \leq k < 0$ and $\omega > 0.4$ cpd are defined as high-frequency eastward (H_e) and westward (H_w) waves, respectively, which approximately represent eastward and westward IG waves, respectively. ~~This~~It is noteworthy that the source level of H_e (H_w) waves are likely located at 150 hPa and below (140 hPa and above) based on the changes in the direction of EPF vectors and the sign of EPD (Fig. S1). Therefore, in this study, we simply assume the source level of $H_e + H_w$ waves as 140 hPa. The separation method in the troposphere enables us to identify the source location of the anomalously strong waves observed in the stratosphere.

2.4 Offline CGW parameterization

We apply the offline CGW parameterization using MERRA-2 data focusing on small-scale waves (λ_h < 100 km and λ_z < 40 km, where λ_z is the vertical wavelength), which is similar to the work of Kang et al. (2017, 2018) using NCEP Climate Forecast System Reanalysis (CFSR; Saha et al~~.~~., 2010) data. The offline CGW parameterization calculates GW momentum flux induced by convective heating rate at the source level (cloud top) as a function of phase velocity; the GW momentum flux and drag from the cloud top to the stratosphere are calculated based on columnar wave propagation by using Lindzen's saturation theory (Lindzen, 1981). The parameterization requires convective heating rate and convective cloud-top and -bottom heights in addition to standard variables such as wind, temperature, and geopotential height as input data. MERRA-2 provides only cloud-top height without convective heating rate, so we tried to extract convection-induced heating rate from the MERRA-2 output field DTDTMST; this field contains all process that contributes to latent heating by moist convection, not exclusively by cumulus convection (Bosilovich et al., 2016). To reconcile this limitation, we select cases that satisfy several criteria to represent clouds which can generate convective GWs. First, we only considered DTDTMST profiles in which column-maximum height is higher than 850 hPa. Second, we estimated the convective cloud-top and -bottom heights as the locations where DTDTMST falls to 20% and 5%, respectively, from its maximum. Here, the convective cloud top should not exceed cloud-top height provided by MERRA-2. Although the percentage of 20% seems large, we decided to use the value considering the large tail in the upper part of the DTDTMST profile (Fig. ~~S1~~S2). Note that the cloud-top height is provided by MERRA-2, but we chose instead to estimate it from the DTDTMST profile because the cloud-top heights in MERRA-2 are sometimes too high due to stratiform clouds, such as anvil clouds, which do not represent the top height of the convection properly. Third, when (i) the convective cloud top height is at altitudes lower than 700 hPa, (ii) the convective cloud bottom height is higher

than 7 km, or (iii) the convective cloud depth is shallower than 1 km, the profiles are eliminated. The DTDTMST profiles selected using the aforementioned procedure will be referred to as convective heating profiles hereafter; they are generally similar to the convection-induced heating profiles estimated from ~~satellite~~GPM observations (~~GPM Science Team, 2017; Lang and Tao, 2018) (~~Fig. ~~S1~~S2). Note that the magnitude of the CGW momentum flux is constrained by the observed GW momentum flux from ~~SPBs~~super-pressure balloons in the tropical region (Jewtoukoff et al., 2013). Because spatio-temporal variations in convective activity and background flows are considered in the parameterization, it is valuable to investigate the variations in the magnitude and the spectral shape of the CGW momentum flux during the QBO disruption.

2.5 Barotropic instability

Barotropic instability, a possible source of the MRG waves, is evaluated using the meridional gradient of the potential vorticity (Andrews et al., 1987):

$$\bar{q}_\phi = 2\Omega\cos\phi - \left[\frac{(\bar{u}\cos\phi)_\phi}{a\cos\phi}\right]_\phi - \frac{a}{\rho_0}\left(\frac{\rho_0 f^2}{N^2}\bar{u}_z\right)_z, \quad (3)$$

where Ω is the Earth's rotation and N is the buoyancy frequency. The negative regions of $\bar{q}_\phi$ suggest a possibility of baroclinic instability, because the positive and negative $\bar{q}_\phi$ values in a neighboring region satisfy the necessary condition for the instability (Gill, 1982). In this study, however, negative $\bar{q}_\phi$ is considered as an indication of barotropic instability because the baroclinic term is negligible (not shown).

3. Results

3.1 General characteristics of zonal wind and equatorial waves

Figure 1 shows zonal-mean zonal wind in a latitude–height cross section from October 2015 to February 2016~~,~~ and monthly climatology from October to February~~,~~ (Fig. 1a) and the zonal-mean zonal wind profile averaged over 5°N–5°S during the disruption, compared with its monthly climatology~~.~~ (Fig. 1b). Again, the climatology here refers to that of the WQBO phases defined in Sect. 2.1. In October 2015, WQBO is very deep compared to the climatology. The WQBO starts to split into two maxima as early as November 2015~~,~~ (Fig. 1a), and the westerly wind becomes anomalously weak at 40–50 hPa by more than 1σ, where σ is the standard deviation of the zonal-mean zonal wind, in December 2015~~.~~ (Fig. 1b). In January 2016, the zonal wind at 40 hPa continuously decelerates, and then changes into easterly in February. From January 2016, the zonal wind at the altitude above 30 hPa exhibits a strong westerly wind greater than the climatology by more than 1σ~~,~~ (Fig. 1b), indicating

that the WQBO is anomalously deep. In the upper troposphere (100–150 hPa), easterly anomalies are shown in November 2015, but from January 2016, westerly anomalies appear.

Figure 2 shows latitude–height cross sections of the EPF and EPD for each type of wave in February 2016. Note that the parameterized CGW momentum flux ($\rho_0\overline{u'w'}$) is multiplied by ($-\cos\phi$) to display the vertical EPF vectors of CGWs, and each of the wave forcings and vectors in Fig. 2 is scaled differently in order to mainly focus on their morphology. The EPD more negative than climatology by more than 1σ is stippled, which represents anomalously strong negative wave forcing. The parameterized CGWs (P-CGWs in Fig. 2a) generally exert a positive ~~or (~~negative) drag on the zonal wind in regions of positive ~~or (~~negative) wind shear, respectively, with the strongest negative forcing at 7–20 hPa between 5°N and 10°S. The negative CGW forcing at 40–50 hPa between 10°N and 10°S is anomalously strong. In 20°N–5°S, westward-propagating P-CGWs are dominant, which can be inferred from the direction of vertical EPF vectors.

Kelvin waves (Fig. 2b) exert positive wave forcing in the positive shear zone, strengthening the bottom side of the westerly jet. Therefore, Kelvin waves may help to maintain two westerly jets (5–30 hPa and 50–80 hPa) with a developing easterly jet in between~~.~~, as in Fig. 3c of Lin et al. (2019). This result is also consistent with the findings of Li et al. (2020), who showed the contribution of strong Kelvin wave activity related to an El Niño event to the long-lasting westerly jet near 20 hPa. MRG waves (Fig. 2c) show anomalously strong negative forcing at 50–80 hPa, 30–40 hPa, and 15–20 hPa, concentrated at the equator. They seem to be generated in the altitude range (60–90 hPa and 30–40 hPa) in which the EPD has positive values at 5°–10°N/S~~.~~, which is also revealed in Fig. 3b of Lin et al. (2019). As will be shown later, the effect of the MRG waves is to flatten the meridional profile of the westerly jet, possibly making the jet more sensitive to erosion by other waves, such as Rossby waves.

IG waves (Fig. 2d~~)~~), which has not been reported before, exhibit a negative forcing near the equator (10°N–10°S) ~~exhibit a negative forcing~~ from 70 hPa to 5 hPa with a maximum forcing at 8–20 hPa, while the anomalously strong negative IG wave forcing is mainly located at 50–70 hPa and 8–20 hPa. The negative Rossby wave forcing (Fig. 2e) is anomalously stronger than the climatology at 30–50 hPa between 20°N and 25°S, which is attributed to the waves that propagate from the NH extratropics~~.~~ as in the previous studies. The same figure during the whole QBO disruption period from October 2015 to ~~February~~March 2016 is shown in Fig. ~~S2~~S3 in the online supplemental material.

Figure 3 shows time–height cross sections of the zonal wind, zonal wind tendency, vertical advection [the second term on the right-hand side of Eq. (1)], required wave forcing, and forcing due to each type of wave averaged over 5°N–5°S from July 2015 to June 2016; and their monthly climatology from July to June. The required wave forcing term (REQ) is calculated as a residual by subtracting ~~the~~both the meridional and vertical advection terms from the zonal wind tendency in the TEM equation. In Fig. 3a, both the zonal-mean zonal wind during the disruption and the climatology propagate downward with time, but the WQBO is much deeper during the disruption than in the climatology. This feature is clearly seen in the difference plot of the zonal-mean zonal wind (Fig. 3b), showing a strong westerly anomaly in the upper stratosphere. The westerly wind decelerates at 40 hPa from October 2015, changes into easterly in February 2016, and starts to propagate downward as an

easterly QBO phase afterward. The deceleration of the westerly wind at 40 hPa is also revealed in the zonal-wind tendency (Fig. ~~3a~~3c), as the negative wind tendency at 40 hPa becomes anomalously strong in October 2015.

To investigate whether vertical advection contributes to the anomalous zonal wind tendency near 40 hPa, the vertical advection term (ADVz) in the TEM equation is shown in Fig. 3d. Climatologically, the sign of the equatorial wave forcing is the same as that of the vertical wind shear~~.~~ (Fig. 3m). Therefore, positive $\overline{w}^*$ makes the sign of ADVz opposite to that of the vertical wind shear (Eq. 1), acting to oppose zonal wind tendency (Dunkerton, 1991). From November to December 2015 at 40 hPa, however, ADVz has the same negative sign as the zonal wind tendency because both $\overline{w}^*$ and vertical wind shear are positive (not shown), while the wave forcing is negative regardless of the positive wind shear. Therefore, ADVz acts to accelerate the easterly development by 17% and 2% of the zonal-wind tendency, respectively, with values of -0.3 and -0.1 m s^{-1} mon^{-1} in November and December 2015, respectively. This implies that ADVz also contributes to the QBO disruption in the early stages.

The climatology of REQ (Fig. ~~3e~~3n) has negative (positive) values in the regions of negative (positive) vertical wind shear, but a sudden increase in negative REQ emerges at 40 hPa in October 2015 (Fig. 3e) without negative vertical wind shear. The estimated wave forcing by P-CGWs (Fig. 3f) resembles REQ, especially at the upper stratosphere, where strong negative wind shear exists, and in the altitude range between 40 and 70 hPa after the intrusion of easterly wind. This indicates that the P-CGWs largely contribute to the QBO disruption after the negative wind shear appears near the 40 hPa (i.e., after February 2016). Kelvin wave forcing ~~(Fig. 3g)~~ during the disruption (Fig. 3g) is much greater than the climatology (Fig. 3p) near the altitude of 30 and 60 hPa due to the positive wind shear. The wave forcing could be stronger because of the strong vertical wave flux propagating from the troposphere, which is identified by the enhanced vertical EPF for the Kelvin waves at 70 hPa (Fig. ~~S3~~S4). The positive forcing near 30 and 60 hPa from January to March 2016 accelerates the upper and lower jets, respectively, thereby the upper and lower parts of the QBO jet are not dissipated totally, maintaining the separated jet during the disruption (Fig. 2). Acceleration in the upper and lower parts of the separated QBO jet is also shown by the momentum forcing by P-CGWs (Fig. 3f). The contribution of CGWs to the enhanced jet in the current study may explain why the westerly winds simulated by Watanabe et al. (2018) are relatively weak compared to those in MERRA-2 near 20 hPa and 70 hPa, without non-orographic GW parameterization.

MRG wave forcing ~~(Fig. 3h)~~ is generally stronger during the disruption (Fig. 3h) than in the climatology~~.~~ (Fig. 3q). In addition, there is a sudden increase in the negative MRG forcing at 40 hPa from October to November 2015, which is similar to the pattern seen in REQ at this time and location. This suggests that the MRG waves influence the early stage of the QBO disruption by slowing down the QBO jet. IG waves (Fig. 3i) exert a strong negative forcing in November 2015 ~~contributing~~, which might be related to the enhancement of negative REQ near 40 hPa~~, together~~ along with the MRG wave forcing. Rossby wave forcing (Fig. 3j) near 40 hPa is stronger than the climatology consistently from November 2015 to March 2016, which is considered as a major cause of the QBO disruption.

To summarize, in October 2015, the negative forcing by MRG waves is anomalously strong compared to the climatology at 40 hPa between 5°N and 5°S, and becomes stronger in November 2015 together with IG waves when the Rossby waves start to break at the southern hemispheric (SH) part of the QBO (see Fig. 5). Therefore, MRG and IG wave forcing may precondition the zonal mean flow near the QBO jet core to be easily disrupted by the Rossby waves. This result is similar to what Lin et al. (2019) mentioned that MRG waves precondition the zonal mean flow before Rossby wave breaking. From December 2015 to February 2016, the Rossby wave forcing is dominant among the equatorial waves, while the negative CGW forcing contributes significantly to the disruption in February 2016 when negative vertical wind shear appears near 40 hPa. Figure ~~S4 is~~S5 shows the same ~~figure with~~as Fig. 3 but using ERA-I data. We found that the time evolution of each wave forcing in ERA-I is similar to that in MERRA-2, although the magnitudes of the REQ and wave forcing (vertical advection) in ERA-I is generally stronger (weaker) than that in MERRA-2~~.~~ (Fig. S5). This is possibly due to the large spread in both $\overline{w}^*$ and vertical wind shear between the reanalyses (see Fig. 5 of Kim and Chun, 2015b).

3.2 Quantitative contributions of the equatorial waves

Figure 4 shows the time series of zonal wind, zonal wind tendency, and wave forcing by each type of wave from July 2015 to June 2016 at 40 hPa. The monthly averaged momentum forcing by each type of wave and its contribution to the total negative wave forcing (percentage) are given in Table 1. The zonal wind (Fig. 4a, solid line) changes into easterly in February 2016, whereas the zonal wind tendency (Fig. ~~4c~~4a, dotted line) changes into negative value in October 2015, as shown in Fig. 3. The negative zonal wind tendency in October 2015 is induced by both MRG (-0.43 m s^{-1} mon^{-1}) and IG waves (-0.46 m s^{-1} mon^{-1}), with contributions of 39% and 41%, respectively, while Rossby wave forcing is -0.22 m s^{-1} mon^{-1}, with a relatively small contribution of 20% (Fig. 4b). In November 2015, negative wave forcing by Rossby, MRG, and IG waves increase with contributions of 45%, 27%, and 28%, respectively, which are 2.4, 2.5, and 1.6 times stronger than the climatology, respectively. Afterward, Rossby waves mainly provide negative forcing which induces easterly accelerations in December 2015 and January 2016, with the contributions of 70% and 91% of the total negative forcing, respectively. They are 3.2 and 4.3 times larger than the climatology, respectively. In February 2016, Rossby waves, parameterized CGWs, MRG waves, and IG waves at 40 hPa contribute to the total negative wave forcing by 61%, 20%, 12%, and 7%, respectively. The CGWs dominate the negative forcing with a percentage of 60% in March 2016. When the average is taken over 5°–10°S, however, Rossby waves dominate from October 2015 (Fig. ~~S5~~S7). This implies that the Rossby wave forcing was strong enough to decelerate the edge of the QBO jet (5°–10°S), while it presumably extends to the jet core (0°–5°S; Fig. 5) due to the weakening of the QBO jet by the MRG (Fig. 7) and IG (Fig. 11) wave forcing near the equator. When we compare Figs. 4b and 4d, a similarity between the time evolution of the meridional (vertical) wind shear and that of the Rossby wave (CGW) forcing is shown. This is because the magnitude of the meridional (vertical) wind shear largely determines or is determined by that of the Rossby wave forcing (GWD). Similar time evolution of the equatorial wave forcing is shown in ERA-I (Fig. S6), but the IG wave forcing is somewhat smaller than that in MERRA-2, possibly due to a coarser horizontal resolution.

Coy et al. (2017) showed that the positive peak of GWD in July 2015 is 4.5 m s^{-1} mon^{-1} and the negative GWD in February 2016 is -0.5 m s^{-1} mon^{-1} (see their Fig. 2). In the current study, the positive peak of CGW drag (CGWD) in July 2015 is 3.75 m s^{-1} mon^{-1} and the negative CGWD in February 2016 is -1.0 m s^{-1} mon^{-1}. There are two potential reasons for this discrepancy. First, the GWD reported by Coy et al. (2017) is provided by MERRA-2, which is based on non-orographic GWD parameterization that does not consider GW sources explicitly. The CGWD in the current study is obtained from the physically-based CGWD parameterization, which takes into account the GW variability according to the convective activity. Second, there are some differences in analysis, such as latitude range for averaging [10°N–10°S for Coy et al., (2017) but 5°N–5°S for the present study] and the vertical grids [pressure level for Coy et al., (2017) but model level for the present study]. When we set the average latitude as 10°N–10°S, the CGWD in February 2016 is about -0.7 m s^{-1} mon^{-1}, which is still greater than GWD reported by Coy et al. (2017). This implies that the negative momentum forcing by CGWs is stronger than that by GWs from a fixed source during the disruption.

Fig. 4c shows the meridional and vertical components of the Rossby wave forcing at 40 hPa. The magnitude of the meridional component is larger than that of the vertical component, and becomes dominant in December, January, and February when the negative wave forcing prevails. This demonstrates the importance of meridional propagation from extratropics, as also reported from the previous studies (e.g., Coy et al., ~~2016~~2017; Osprey et al~~.~~., 2016). However, the vertical component is not negligible given that the maximum contribution of the vertical component to the total Rossby wave forcing reaches 26%, which is 18% of the total negative wave forcing, in December 2015 (Table 1). The strong vertical EPD in the stratosphere (40 hPa) does not necessarily indicate the wave propagation from the equatorial region. Hence, the ~~origination~~origin of the vertical Rossby wave forcing will be analyzed in the following subsection.

3.3 Contributions of Rossby waves and MRG waves

In this subsection, we focus on the Rossby and MRG waves and their sources. Figure 5 shows the evolution of the EPF and EPD for the Rossby waves (left), and their meridional (middle) and vertical (right) components, separately, from November 2015 to February 2016. The vertical profiles of meridional EPF (EPF-y) at 10°N and 10°S are included, and meridional distribution of the vertical EPF (EPF-z) at 70 hPa are plotted at the bottom of each month in red lines. In the vertical profiles and meridional distribution plots, climatological monthly means are included with black lines with $\pm 1\sigma$ values indicated in gray shading. Note that in the following figures, the EPF is divided by air density for better visualization. In November 2015 (Fig. 5a), the Rossby waves start to break at the southern flank of the QBO westerly jet near 50 hPa, which is anomalously strong compared to the climatology. They most likely propagate from the NH, given that EPF-y at 10°N is directed southward with a magnitude greater than the climatology by more than 1σ. The EPF-y at 10°S is directed northward at the altitude below 70 hPa, and it is slightly stronger than the climatology; however, this EPF hardly propagates into the QBO jet. In December 2015 (Fig. 5b), anomalously strong negative EPD near 40 hPa in the SH extends northward to 10°N, with the strong EPF-y at 10°N propagating toward SH. The negative EPD in the SH part of the QBO jet at 40 hPa is mainly explained

by its meridional component, which presumably originates from the EPF-y at 10°N between 70 and 30 hPa. On the other hand, the negative EPD in the NH part of the QBO jet at 40 hPa is mainly explained by its vertical component considering the anomalously strong vertical EPD there. The strong vertical EPD seems to originate from the EPF-z at 70 hPa between 0° and 15°N. In January 2016 (Fig. 5c) when the Rossby wave forcing is the strongest, the overall feature is similar to December 2015 although with somewhat different aspects: (i) negative EPD at 40 hPa exhibits a significant peak in 0°–5°S, (ii) EPF-y at 10°N has an additional peak at 40 hPa, and the (iii) EPF-z at 70 hPa in the SH becomes much stronger than the climatology. In February 2016 (Fig. 5d), the anomalously strong negative EPD is more concentrated at 40 hPa with a larger contribution from the meridional EPD at 0°–25°N, while the vertical EPF at 70 hPa is less pronounced compared to January. To sum up, the Rossby wave forcing and the associated wave flux are anomalously strong from November 2015 to February 2016, and both the meridional and vertical components are significantly stronger than the climatology. The meridional EPD, most likely caused by waves propagating southward at 10°N, largely contributes to the deceleration of the QBO jet in the SH. The vertical EPD, presumably caused by waves propagating vertically at 70 hPa between 0° and 15°N, largely contributes to the deceleration of the QBO jet in the NH.

To investigate whether the anomalously strong EPF-z at 70 hPa in Fig. 5 originates in the equatorial region, Fig. 6 shows the EPF and EPD for the L_w waves, which are westward-propagating low-frequency waves, in the troposphere and for the Rossby waves in the lower stratosphere. Here, we focus on January and February 2016 when EPF-z is strong and moderate, respectively. ~~Note that the EPF in Fig. 6 is the same as in Fig. 2, except that it is divided by air density for better visualization.~~ In January 2016 (Fig. 6a), there are three potential source regions of the Rossby waves: (i) 5°N–10°S at 120–400 hPa (equatorial source), (ii) 15°–25°S at 200–350 hPa (SH source), and (iii) 20°–25°N and 250–450 hPa (NH source), considering that the positive EPD region ~~is~~should be a source region of ~~the~~ westward- and upward-propagating waves. First, from the equatorial source, wave activity propagates upward and northward up to ~120 hPa. There, it seems to merge with the wave activity from the NH sources, while part of it propagates upward to the NH stratosphere near 0°–15°N. Second, some of the waves from the SH source propagate to the SH stratosphere after depositing a large amount of negative momentum between 100 and 70 hPa, and others propagate to the NH stratosphere. Third, the wave activity from the NH source does not seem to propagate upward. In addition to the three source regions, there might be other source regions at the midlatitude, so the propagation from the midlatitudes in both hemispheres also needs to be considered. It is shown that the wave activity from the NH (SH) midlatitude propagates into the equatorial stratosphere at the altitude range above 100 hPa (200 hPa). The ~~behaviour~~behavior in February 2016 ~~shows a~~is generally similar ~~pattern~~ to that in January 2016~~, except for an additional positive EPD region at 15°–25°N and 110–150 hPa~~. In summary, the strong EPF-z for Rossby waves at 70 hPa is attributed to both the equatorially generated waves and the waves propagating from the NH and the SH.

Figure 7 shows the EPF and EPD for the MRG waves in October, November, and December 2015, and February 2016, when MRG waves significantly contribute to the negative EPD. The vertical profiles of EPF-y at 10°N and 10°S are plotted on the right and left side of each panel, and the meridional distribution of the EPF-z at 70 hPa is plotted at the bottom of each

panel. In Fig. 7, we will focus on the altitude near 40 hPa, where the wave forcing is directly related to the QBO disruption, although strong negative wave forcing also exists in the upper stratosphere. In October 2015 (Fig. 7a), all the wave forcing is similar to the climatology except for the MRG waves (Fig. ~~S2~~S3); the negative MRG wave forcing is stronger than the climatology by more than 1σ at 50 hPa in 0°–5°S (indicated by the magenta dots). Given the dominant upward propagation in the lower to middle stratosphere, the MRG waves exerting negative forcing near 50 hPa in 0°–5°S seem to propagate from 60–80 hPa and 5°–10°S where the positive EPD exists. While the increase in the meridional EPF at 5°–10°S near 70 hPa is somewhat unclear in the EPF-y at 10°S, it is clear in the EPF-y at 7°S and 5°S showing a noticeable increase toward the equator compared to the climatology (not shown). The increase in the vertical EPF at 60–80 hPa is evident in the EPF-z at 70 hPa, which is greater than the climatology by more than 1σ in 10°S–0°. It is worthwhile to note that there exists positive EPD over 5°–10°N at 70 hPa as well, implying that 5°–10°N and 60–80 hPa might be another source region for MRG wave generation. However, the increases in the EPF-z at 70 hPa and EPF-y at 5°–10°N are less significant compared to the climatology. In November 2015 (Fig. 7b), a pattern similar to that in October 2015 appears, but with an increase in the magnitude of the negative EPD at 40–60 hPa within 5°N/S and the EPF-y at 10°S in 50–80 hPa. The strong EPD at 0°–10°S and 40–60 hPa originates most likely from the strong EPF-y at 10°S in 60–80 hPa and EPF-z at 70 hPa in 5°–15°S. In December 2015 (Fig. 7c) and February 2016 (Fig. 7d), strong negative EPD, equatorward EPF-y at 10°S, and upward EPF-z at 70 hPa are still evident.

According to this analysis, we conclude that MRG waves decelerate the QBO jet core (5°N–5°S) at the onset of the QBO disruption, given that the negative zonal wind tendency from October to November 2015 is partly attributed to the anomalously strong MRG wave forcing~~.~~: the MRG wave forcing at 40 hPa in October and November 2015 are -0.4 and -0.6 m s mon^{-1}, respectively, and the QBO jet core reduces to 12.3, 11.1, and 8.2 m s^{-1} from October to December 2015 (Fig. 4; Table 1). The positive EPD at 60–80 hPa between 5°S and 15°S by MRG is much greater than the climatology both for the meridional and vertical components. From 60–80 hPa and 5°–15°S, the waves propagate equatorward and upward reaching 40–50 hPa near the equator (Figs. 7a–b), implying that the region of 60–90 hPa, 5°–15°S (boxed region in Fig. 8) is a possible location where the MRG waves are mainly excited.

Coy et al. (2017) have investigated whether baroclinic instability leads to the easterly wind development in February 2016, although they did not investigate the possibility of the wave generation/amplification by baroclinic/barotropic instability for the period before February 2016. As MRG waves contribute significantly to the negative EPD from October to November 2015 (Figs. 3, 4 and 7), it is worth examining whether baroclinic/barotropic instability is a likely source of MRG waves (Andrews and McIntyre, 1976; Garcia and Richter, 2019) in October and November 2015~~, which is evaluated using the meridional gradient of the potential vorticity (Andrews et al., 1987):~~.

~~$$\bar{q}_\phi = 2\Omega\cos\phi - \left[\frac{(\bar{u}\cos\phi)_\phi}{a\cos\phi}\right]_\phi - \frac{a}{\rho_0}\left(\frac{\rho_0 f^2}{N^2}\bar{u}_z\right)_z, \quad (3)$$~~

~~where Ω is the Earth's rotation and N is the buoyancy frequency. The negative regions of $\bar{q}_\phi$ suggest a possibility of baroclinic instability, because the positive and negative $\bar{q}_\phi$ values in a neighboring region satisfy the necessary condition for the instability (Gill, 1982).~~

Figure 8 presents the monthly-mean $\bar{q}_\phi$ (Figs. 8a–b~~) and~~), the number of grids where the daily-mean $\bar{q}_\phi$ is negative (~~Figs~~Fig. 8c~~–d~~) along with its climatology, and daily-mean EPD for the MRG waves (Fig. 8d) in October and November 2015. The monthly-mean $\bar{q}_\phi$ in the boxed region has small positive values in October 2015 (Fig. 8a) and November 2015 (Fig. 8b). In ~~Figs~~Fig. 8c~~–d~~, however, 22 and 25 days during October and November, respectively, have negative $\bar{q}_\phi$ values by at least one point within the boxed region, which satisfy a necessary condition for baroclinic instability, dominated by the barotropic instability (not shown). The number of negative $\bar{q}_\phi$ days are much larger than the climatology (11 and 19 days with standard deviations of 11 and 7 days in October and November, respectively~~; not shown). This suggests that baroclinic~~). When the number of grids with $\bar{q}_\phi < 0$ increases, the daily-mean EPD becomes large (e.g., 1–11 October, 21–25 October, and 25–30 November). This suggests that barotropic instability at the boxed region is a possible source for generating the anomalously strong MRG waves. The MRG waves generated by the ~~baroclinic~~barotropic instability in the narrow westerly jets accelerate the zonal wind off the equator and decelerate the zonal wind near the equator, reducing the curvature and thus the instability, which indicates that the MRG waves respond to the QBO wind system (Garcia and Richter, 2019). However, as the deceleration of the jet core is important in the QBO disruption, such behavior may play an important role in preconditioning the background wind. It should be noted that the ~~baroclinic~~barotropic instability does not seem to be an exclusive source of the MRG waves because there exist precedent WQBO cases having considerable negative $\bar{q}_\phi$ without significant enhancement in the wave generation (e.g., 2010, 1987, and 1982). Therefore, further studies on the source of the MRG waves should be done in the future. It is also interesting that $\bar{q}_\phi$ shows large negative values at the upper stratosphere (~5 hPa) where the zonal wind curvature is large in association with strong westerly jet (Hamilton, 1984). Nevertheless, it is unlikely that the MRG waves generated at 5 hPa ~~affects~~affect the QBO disruption as the upward propagating MRG waves (i.e., vertical EPF >0) are dominant in the stratosphere, and the strong easterlies between 5 to 10 hPa inhibit the propagation of the MRG waves.

We found in the previous figures (Figs. 5 and 6) that the increased Rossby wave forcing in the stratosphere partly originates from the equatorial troposphere. Therefore, in Fig. 9, we examine the zonal-mean precipitation in the equatorial troposphere to identify convective activity using MERRA-2 data. Overall, the zonal-mean precipitation from November 2015 to February 2016 is stronger than the climatology in 5°N–5°S. It is greater than the climatology by more than 1σ from November to December 2015 (Figs. 9a–b). In February 2016 (Fig. 9d), the precipitation is much stronger than the climatology between 5°N and 10°S by more than 3σ. The maximum precipitation is slightly shifted southward in December–January–February (DJF), following the location of the inter-tropical convergence zone (ITCZ).

We further check whether the precipitation spectrum related to each equatorial wave type is enhanced during the disruption. Figure 10 illustrates the power spectrum of the precipitation data of MERRA-2 divided by background spectrum averaged over 10°N–10°S for both the symmetric and anti-symmetric components. The background spectrum is obtained by applying 1-2-1 smoothing to the base-10 logarithm of the raw spectrum (separately for the symmetric and antisymmetric spectrum) in wavenumber and frequency 40 and 10 times, respectively, and applying based-10 exponential again to the smoothed spectrum (Chao et al., 2009). If the raw spectrum divided by the background spectrum is greater than 1.4, it is considered statistically significant at the 95% level for 41 degrees of freedom (i.e., corresponding to the number of the latitude grid cells from 10°N to 10°S) (Wheeler and Kiladis, 1999).

The area where the precipitation spectrum is greater than the climatology by more than 1σ, which is denoted by a stippled pattern, widens from November 2015 to February 2016, indicating that not only the mean value but also the variability of the convection significantly increases during the disruption. The spectra related to Rossby waves in the symmetric spectrum (k = -10–0, ω = 0–0.15 cpd) are statistically significant throughout the period, suggesting that the convective activity in the troposphere is the probable source for Rossby waves. However, the waves in the low-frequency spectra have less possibility to propagate upward into the stratosphere due to their slow vertical-group velocity (Yang et al., 2011). In November 2015 (Fig. 10a) and December 2015 (Fig. 10b), the spectra related to MRG waves in the anti-symmetric component (k = -9 and ω = 0.12; k = -5 and ω = 0.28) are statistically significant and their amplitude is stronger than the climatology by more than 1σ. However, they are less likely to be the primary source of the anomalously negative MRG wave forcing in the stratosphere, given that the EPF-z for MRG waves greater than the climatology only appears at altitude above 70 hPa (Fig. 7). It is also interesting that the peaks related to Kelvin waves (k = 0–10 and ω = 0–0.25) are increasing from November 2015 (Fig. 10a) to February 2016 (Fig. 10d), consistent with the increasing EPF-z at 70 hPa (see Fig. ~~S3~~S4) and the resultant EPD (Fig. 2) during the disruption. The enhanced Kelvin wave activity during the disruption period was caused by the enhanced convective activity associated with strong El Niño events (Li et al., 2020). Overall, we found that convectively-coupled equatorial waves are enhanced during the QBO disruption, which seem to be associated with El Niño.

To validate the realism of the MERRA-2 precipitation data, we additionally calculate the space-time spectra of precipitation provided by TRMM in Fig. ~~S6~~S8. The key features are present in TRMM, but its amplitude is larger than that of MERRA-2, possibly attributed to the finer resolution. Note that TRMM data are available in a shorter period (1998–2016) than the MERRA-2 data (1980–2016), so only five years are included as WQBO climatology in Fig. ~~S6~~S8. As in the MERRA-2 data, there exists significant increase in the precipitation of TRMM during January and February 2016 (Fig. ~~S6~~S8) compared to the climatology.

3.4 Contribution of inertia-gravity waves

Figure 11 shows EPF vectors and EPD for the IG waves, together with the meridional distribution of EPF-z at 70 hPa, from November 2015 to February 2016. In this figure, the vertical cross section of EPF-y is not shown because EPF-z

dominates the total EPF. EPF-z here is the net EPF of eastward and westward IG waves, so the positive EPF-z indicates stronger westward EPF than the eastward one, given the dominant upward propagation in the stratosphere. Anomalously strong negative wave forcing exists at 10–20 hPa near the equator throughout the period. In November 2015 (Fig. 11a), negative wave forcing is anomalously strong at 40–80 hPa near the equator (0°–5°S), influencing the deceleration and the downward shift of the WQBO jet core in the following months. The strong negative forcing is likely attributable to the strong vertical EPF at 70 hPa, which is greater than the climatology by more than 1σ. In December 2015 (Fig. 11b) and January 2016 (Fig. 11c), it is shown that the negative wave forcing at 40–80 hPa near the equator and the westward EPF-z at 70 hPa in 10°N–10°S are anomalously strong, as in November 2015. In February 2016, negative wave forcing exists at 40 hPa and 0°–5°S without significance, while the negative wave forcing near the top of the lower jet is significant. From November 2015 to February 2016, the strong westward IG wave forcing is mainly induced by the vertical EPF penetrating into the stratosphere from the troposphere. Then why do the westward IG waves at 70 hPa show a noticeable increase during the disruption?

To answer this question, we show the vertical EPF for $H_e + H_w$ waves ~~[(i) $|k| > 20$ for all ω or (ii) $|k| \leq 20$ for $\omega > 0.4$ cpd]~~ (approximately for IG waves) at the source level (140 hPa; Sect. 2.3) from November 2015 to February 2016 in Fig. ~~12, where the source level is set to 140 hPa based on the changes in the sign of EPD (not shown).~~12. The eastward and westward waves have similar magnitudes in November 2015. However, the westward-propagating waves start to dominate the vertical EPF from December 2015. In January and February 2016, the vertical EPF at 140 hPa is greater than the climatology by more than 1σ at 10°N–10°S. The stronger westward EPF-z at 140 hPa from December 2015 to February 2016 suggests that the preference for westward propagating waves at 70 hPa stems from the source level (140 hPa; Sect. 2.3) except in November 2015.

Figure 13 illustrates the power spectral density of the precipitation in a phase-speed spectrum of the $H_e + H_w$ waves from November 2015 to February 2016 along with the climatology. The precipitation spectrum is classified as eastward- (westward-) propagating waves when the phase-speed is larger (smaller) than the zonal wind at the source level. The double-sided arrows represent the zonal wind range between the source level (140 hPa) and 70 hPa in each month, indicating the phase-speed range of the critical-level filtering. In November 2015 (Fig. 13a), the zonal wind at the source level is near zero, so the precipitation spectrum has a similar amplitude between the eastward and westward waves. However, the eastward waves are almost filtered out due to the positive vertical wind shear between 140 and 70 hPa (see Fig. 1). This feature is different from the climatology, which has stronger westward waves than eastward waves at the source level. As most of the pronounced westward waves are filtered out due to the negative vertical wind shear (see Fig. 1), the remaining spectrum at 70 hPa in November 2015 has more westward waves than the climatology. In December 2015 (Fig. 13b), the wave characteristics at the source level during the disruption agree well with the climatology—that is, stronger westward waves than eastward waves and a similar magnitude of westerly winds at the source level. However, both a larger magnitude of the precipitation spectrum and the narrower critical-level filtering range for the westward waves result in stronger westward momentum flux at 70 hPa during the disruption than the climatology. From January 2016 (Fig. 13c), (i) the westerly anomaly at the source level, (ii) strong precipitation spectrum,

and (iii) decreased critical-level filtering of the westward waves induce a stronger westward momentum flux at 70 hPa. The presence of stronger westerlies at the source level than the climatology during the disruption becomes apparent in February 2016, leading to the strongest westward momentum flux at the source level. The same conclusion is obtained when the eastward and westward waves are analyzed separately (Fig. S9). Figure 13 suggests that strong westward IG waves at 70 hPa during the disruption are largely attributed to the reduced critical-level filtering of westward waves in November 2015, while in December 2015, those are attributed to both enhanced convection and the decreased critical-level filtering. In January and February 2016, westerly anomaly at the source level and the reduced filtering of westward waves plays an important role in the increased westward IG wave forcing, along with stronger convection.

Kawatani et al. (2019) showed stronger westward wave forcing between 40 hPa and 70 hPa during El Niño than during La Niña in their Model for Interdisciplinary Research on Climate-Atmospheric General Circulation Model (MIROC-AGCM) simulation. They explained that larger westward forcing is due to the strong westward EPF in the UTLS, which is attributed to the enhanced convective activity with $-10 < c < 10$ m s^{-1} (where c is the phase speed) and less critical-level filtering of the IG waves during El Niño than during La Niña. ~~This is~~The stronger filtering of IG waves during El Niño is due to the westerly anomalies in the lower stratosphere, which is supported by the fact that the zonal wind near the equator becomes more westerly during El Niño than during La Niña (Barton and McCormack, 2017). These are consistent with our result, implying that the enhanced wave source (i.e., convection) and the propagation conditions favorable for westward IG waves in the current study are presumably associated with the strong El Niño condition.

3.5 Contribution of parameterized CGWs

Figure 14 illustrates the zonal-mean zonal CGWD overlaid with zonal-mean zonal wind profile and the source-level CGW momentum flux averaged over 5°N–5°S in February 2016, when CGWD started to contribute to the QBO disruption, along with the climatology. Negative CGWD appears where the vertical wind shear is negative, with a maximum magnitude of -1.9 m s^{-1} mon^{-1} at 47 hPa. Once a negative vertical wind shear develops, CGWs begin to exert negative forcing on the zonal wind, making the vertical wind shear stronger, which in turn leads to a greater negative CGWD. It is noticeable that the source-level CGW spectrum reveals much stronger momentum flux than the climatology and the difference from the climatology is larger for the westward momentum flux than the eastward momentum flux, resulting in a faster and more irreversible easterly development at 40 hPa. In addition to the source spectrum, the apparent positive wind shear in the upper troposphere (140–200 hPa) during February 2016 enhances the propagation of westward waves into the stratosphere in comparison to the negative wind shear in the climatology.

We would like to answer the following two questions: (1) Why is the source-level CGW momentum flux stronger in February 2016 than in the climatology? (2) Why is the increased amount of westward momentum flux larger than that of eastward momentum flux? Figure 15 illustrates the convective source spectrum and the wave-filtering and resonance factor (WFRF) spectrum, which are two important factors constituting source-level CGW momentum flux spectrum in the

parameterization by Kang et al. (2017). The ~~magnitude of~~ convective source spectrum is related to the size, magnitude, and movement of the convection: its magnitude is proportional to the square of the convective heating rate, having a peak where the phase speed equals to the moving speed of convection (c_{qh}). ~~WFRF~~WFRF is related to the shape of the wave spectra emitted from the convection, which includes two main effects: (i) critical-level filtering within the convective forcing region and (ii) the ~~amplification of the response due to the matching of~~resonance between the vertical ~~wavelength~~harmonics of the ~~GW and the vertical configuration of~~ convective heating and the natural wave modes. As the convective heating is deeper, WFRF integrated over all phase speeds becomes larger and its peak is shifted to the higher phase speed (Song and Chun, 2005). The magnitude of the convective source spectrum (Fig. 15a) is much stronger than the climatology and WFRF (Fig. 15b) shows a stronger magnitude throughout all phase speeds, both of which lead to the exceptionally strong momentum flux of CGWs. The stronger magnitude of WFRF is not only due to ~~a higher static stability and~~ the stronger/deeper convection ~~that are possibly triggered~~caused by El Niño~~, in which there is a warm troposphere and cool stratosphere (Domeisen~~ (Geller et al., ~~2019~~2016; Kawatani et al., 2019) but also due to the higher static stability at the cloud top (~200–300 hPa) in association with the warm surface temperature. Note that tropospheric static stability is enhanced under the global warming (He et al., 2019; Richter et al., 2020), and 2016 is the warmest year on record for the global-mean surface temperature (GISTEMP Team, 2020). The zonal wind at the cloud top (white line) exhibits a weaker easterly compared to the climatology ~~(gray line):~~: zonal winds at the cloud top averaged over 5°N–5°S are -3.4 and -4.4 m s^{-1} for the disruption and the climatology, respectively. On the other hand, the difference in c_{qh} (gray line) is negligible. Thus, the westerly wind anomaly at the cloud top is responsible for the westward CGWs that are increased more than the eastward CGWs at the source level during the disruption.

4. Summary and Conclusion

In this study, we have investigated the contribution of each equatorial planetary wave mode and parameterized convectively-excited gravity waves, CGWs, to the 2015–16 QBO disruption by utilizing the equatorial wave separation method of Kim and Chun (~~2015~~2015a) and the offline CGW parameterization by Kang et al. (2017) using MERRA-2 model-level data. The main results, represented in schematic form in Fig. 16, are as follows:

- From October to November 2015, anomalously strong negative forcing by MRG waves mainly decelerated the QBO jet at 0°–5°S near 40–50 hPa. From November 2015, IG wave forcing became anomalously strong at the altitudes below 50 hPa, when the Rossby waves propagating from the NH began to break at the southern flank of the westerly jet (0°–10°S) at 30–60 hPa. The anomalous MRG waves were possibly generated by the increased frequency of barotropic instability in the lower stratosphere. IG wave forcing was attributed to (i) stronger convection in the equatorial troposphere, (ii) stronger westerly (or weaker easterly) winds leading to an enhanced westward momentum flux at the source level, and (iii) the reduced critical-level filtering of the westward waves arising from weaker negative wind shear in the UTLS compared to the climatology.

- From December 2015, Rossby-wave breaking extends from the SH to the equator. The deceleration of the QBO jet in the NH was mainly induced by the vertically propagating Rossby waves penetrating into the stratosphere. They likely originated in the NH and SH extratropics as well as in the tropics, generated by the convection in the equatorial troposphere. The deceleration of the QBO jet in the SH is mainly induced by Rossby waves propagating laterally from the NH extratropics. In January 2016, Rossby wave forcing was the strongest among all equatorial waves.
- In February 2016, the QBO jet at 40 hPa was continuously decelerated by the Rossby waves, propagating both vertically and latitudinally. At the same time, the estimation of the CGW forcing suggests that CGWs provided negative forcing on the QBO jet at 40–50 hPa near the equator, contributing to 20% of the total negative wave forcing. The enhancement in the negative CGWD is partly explained by excessively strong westward momentum flux at the source level, which was attributed to the westerly wind anomaly at the source level and the reduced critical-level filtering of the westward waves in the upper troposphere.
- Meanwhile, the Kelvin waves and CGWs helped confine the development of the easterlies to the region near 40 hPa by strengthening the westerly jets near 20–30 hPa and 60–80 hPa from January 2016.

In previous studies, laterally propagating Rossby waves from the midlatitudes have been considered as the primary cause of the QBO disruption, although Lin et al. (2019) emphasized the role of local equatorial wave forcing in preconditioning the Rossby wave breaking. In the present study, we found that anomalously strong negative MRG and IG wave forcing in the early stage of the QBO disruption played a significant role in preconditioning the QBO jet core. Figure 17 shows scatter plots demonstrating how the wave flux or wave forcing was anomalously strong compared to the climatology. The negative EPDs for the MRG and IG waves in 2015 were the strongest among those in other WQBO cases (Fig. 17a), where the EPDs for the MRG waves and IG waves are averaged for October–November and November–December, respectively. We also found that Rossby waves propagating upward from the equatorial troposphere significantly contribute to the QBO jet in the NH, which helped to interrupt the westerly jet along with the equatorward propagating Rossby waves. Both the meridional and vertical EPF of the Rossby waves propagating into the equatorial stratosphere averaged for January–February in 2016 were stronger than those in any other years of WQBO phases (Fig. 17b). The contribution of the parameterized CGWs to the QBO disruption, which had been considered small, was found to be substantial when a physically based CGW parameterization was used; the negative CGWD in February 2016 was the largest among CGWD values in February with WQBO phases at 30–50 hPa (Fig. 17c). The strongest CGWD at 30–50 hPa is not surprising given that 2016 is the only year when the negative vertical wind shear occurs near 40 hPa due to sudden easterly development. However, it is surprising that the westward CGW momentum flux at the source level in February 2016 was much stronger than in any of the February with WQBO phases (Fig. ~~16c~~17c). This suggests that the variability of the GWs according to the convective activity leads to an enhancement in the negative CGWD at 40 hPa.

The current results are based on the MERRA-2 data, and some uncertainties might be included in association with reanalysis data. Therefore, we checked whether the behavior of the equatorial waves in MERRA-2 also appears in ERA-I

during the QBO disruption period (~~Fig. S3~~Figs. S5–S6). The equatorial wave forcing in ERA-I showed similar time evolution to that in MERRA-2, despite somewhat larger wave forcing in ERA-I. In addition, the tropical precipitation in MERRA-2, which increased during the QBO disruption, was found to be evident in the observed precipitation (TRMM; Fig. ~~S6~~S8). One additional point to mention about the uncertainties in our results is on the cloud top and bottom heights used for the CGW parameterization. Although we tried to make vertical profiles of the convective heating rate comparable to those estimated from the satellite observations (Sect. 2.4), CGW momentum flux spectrum is very sensitive to the cloud-top and -bottom heights (Song and Chun, 2005; Kang et al., 2017) that are derived from the threshold percentage of the convective heating profiles. Considering the importance of cloud-top and -bottom heights, their realistic estimation needs to be further investigated in the future.

Although not discussed in the results section, a QBO westerly phase that does not rapidly propagate downward and maintains westerly winds throughout a deep layer might provide a favorable condition for the QBO disruption. Hitchcock et al. (2018) mentioned that westerly QBO should be deep enough to develop easterly winds away from the top and bottom shear regions of the jet. In addition, Osprey et al. (2016) reported enhanced tropical upwelling during the disruption. In our analysis, it is found that not only the mean upwelling ($\overline{w}^*$) in the whole stratosphere was strengthened but also upwelling in the upper stratosphere was stronger than the climatology (c.f. strong positive ADVz at the top of the QBO in Fig. 3), which made a deep and stalled QBO jet susceptible to the continuous deceleration by wave forcing. Therefore, it would be interesting to investigate the vertical upwelling and its importance during the disruption period.

In this study, we found that the 2015–16 QBO disruption occurred when the following conditions were met: (i) negative equatorial wave (MRG, IG) forcing in the early stages and (ii) strong vertical and horizontal components of Rossby waves with strong small-scale CGWs in the later stages. The enhancement in the convective activity as well as anomalous wind profile, possibly attributed to a strong El Niño, leads to anomalously strong negative equatorial wave forcing. However, it is still puzzling why the equatorial wave activity in 2015/16 is stronger than those in other El Niño periods, which requires further investigation. Because more frequent occurrences of the QBO disruption are expected in a warmer climate (Osprey et al., 2016; Hirota et al., 2018), understanding the 2015–16 QBO disruption would eventually lead to an improvement of the long-range forecast in the future.

Data availability. The MERRA-2 data were provided by the Global Modeling and Assimilation Office at NASA Goddard Space Flight Center through the NASA GES DISC online archive (available online at https://gmao.gsfc.nasa.gov/reanalysis/). The ERA-I data were obtained from the ECMWF data server (available online at http://apps.ecmwf.int/datasets/).

Author contributions. HYC and MJK designed the study and MJK carried it out. MJK prepared the manuscript with contribution from HYC and RRG. All co-authors interpreted the results and reviewed and edited the paper.

Competing interests. The authors declare they have no conflict of interest.

Acknowledgments. This work was supported by the National Research Foundation of Korea(NRF) grant funded by the Korea government(MSIT) (No. 2020R1A4A1016537). We would like to thank J.-H. Yoo for helpful comments.

References

Andrews, D. G., and Mcintyre, M. E.: Planetary waves in horizontal and vertical shear: The generalized Eliassen-Palm relation and the mean zonal acceleration, J. Atmos. Sci., 33, 2031–2048, 1976.

Andrews, D. G., Mahlman, J. D., and Sinclair, R. W.: Eliassen–Palm diagnostics of wave-mean flow interaction in the GFDL" SKYHI" general circulation model, J. Atmos. Sci., 40, 2768–2784, 1983.

Andrews, D. G., Holton, J. R., and Leovy, C. B.: Middle Atmosphere Dynamics, Academic, San Diego, California, 1987.

Anstey, J. A., and Shepherd, T. G.: High-latitude influence of the quasi-biennial oscillation, Q. J. R. Meteorol. Soc., 140, 1–21. doi:10.1002/qj.2132, 2014.

Baldwin, M. P., and Dunkerton, T. J.: Stratospheric harbingers of anomalous Weather Regimes, Science, 294, 581–584, 2001.

Baldwin, M. P., Gray, L. J., Dunkerton, T. J., Hamilton, K., Haynes, P. H., Randel, W. J., Holton, J. R., Alexander, M. J., Hirota, I., Horinouchi, T., Jones, D. B. A., Kinnersley, J. S., Marquardt, C., Sato, K., and Takahashi, M.: The quasi-biennial oscillation, Rev. GeoPhys., 39, 179–229, 2001.

Barton, C. A., and McCormack, J. P.: Origin of the 2016 QBO disruption and its relationship to extreme El Niño events, Geophys. Res. Lett., 44, 11150–11157, https://doi.org/10.1002/2017GL075576, 2017.

Boer, G. and Hamilton, K.: QBO influence on extratropical predictive skill, Clim. Dynam., 31, 987–1000, doi:10.1007/s00382-008-0379-5, 2008.

Bosilovich, M. G., Lucchesi, R., and Suarez, M.: MERRA-2: File specification GMAO Office Note No. 9 (Version 1.1), available at: http://gmao.gsfc.nasa.gov/pubs/docs/Bosilovich785.pdf (last access: 20 June 2016), 2016.

Chao, W. C., Yang, B., and Fu, X.: A revised method of presenting wavenumber-frequency power spectrum diagrams that reveals the asymmetric nature of tropical large-scale waves, Clim. Dyn., 33(6), 843–847, doi:10.1007/s00382-008-0494-3, 2008.

Collimore, C. C., Martin, D. W., Hitchman, M. H., Huesmann, A., and Waliser, D. E.: On the relationship between the QBO and tropical deep convection, J. Climate, 16, 2552–2568, https://doi.org/10.1175/1520-0442(2003)016,2552:OTRBTQ.2.0.CO;2, 2003.

Coy, L., Newman, P. A., Pawson, S., and Lait, L. R.: Dynamics of the disrupted 2015/16 quasi-biennial oscillation, J. Climate, 30, 5661–5674, https://doi.org/10.1175/JCLI-D-16-0663.1, 2017.

Dee, D. P., Uppala, S. M., Simmons, A. J., Berrisford, P., Poli, P., Kobayashi, S., Andrae, U., Balmaseda, M. A., Balsamo, G., Bauer, P., Bechtold, P., Beljaars, A. C. M., van de Berg, L., Bidlot, J., Bormann, N., Delsol, C., Dragani, R., Fuentes, M., Geer, A. J., Haimberger, L., Healy, S. B., Hersbach, H., Hólm, E. V., Isaksen, L., Kållberg, P., Köhler, M., Matricardi, M., McNally, A. P., Monge-Sanz, B. M., Morcrette, J.-J., Park, B.-K., Peubey, C., de Rosnay, P., Tavolato, C., Thépaut, J.-N., and Vitart, F.: The ERA-Interim reanalysis: configuration and performance of the data assimilation system, Q. J. Roy. Meteorol. Soc., 137, 553–597, doi:10.1002/qj.828, 2011.

Domeisen, D. I. V., Garfinkel, C. I., and Butler, A. H.: The teleconnection of El Niño–Southern Oscillation to the stratosphere, Rev. GeoPhys., 57, 5–47, https://doi.org/10.1029/2018RG000596, 2019.

Dunkerton, T. J.: Nonlinear propagation of zonal winds in an atmosphere with Newtonian cooling and equatorial wavedriving, J. Atmos. Sci., 48(2), 236–263, 1991.

~~Evan, S., Alexander, M. J., and Dudhia, J.: Model study of intermediate scale tropical inertia–gravity waves and comparison to TWP-ICE campaign observations, J. Atmos. Sci., 69, 591–610, https://doi.org/10.1175/JAS-D-11-051.1, 2012.~~

Ern, M., F. Ploeger, P. Preusse, J. C. Gille, L. J. Gray, S. Kalisch, M. G. Mlynczak, J. M. Russell III, and M. Riese: Interaction of gravity waves with the QBO: A satellite perspective, J. Geophys. Res. Atmos., 119, 2329–2355, doi:10.1002/2013JD020731, 2014.

Evan, S., M. J. Alexander, and J. Dudhia: WRF simulations of convectively generated gravity waves in opposite QBO phases, J. Geophys. Res., 117, D12117, doi:10.1029/2011JD017302, 2012.

Garcia, R. R., and Richter, J. H.: On the momentum budget of the quasi-biennial oscillation in the Whole Atmosphere Community Climate Model, J. Atmos. Sci., 76, 69–87, https://doi.org/10.1175/JAS-D-18-0088.1, 2019.

Garfinkel, C. I., and Hartmann, D. L.: The influence of the quasi-biennial oscillation on the troposphere in wintertime in a hierarchy of models. Part I: Simplified dry GCMs, J. Atmos. Sci., 68, 1273–1289, 2011.

Gelaro, R., McCarty, W., Suarez, M. J., Todling, R., Molod, A., Takacs, L., Randles, C. A., Darmenov, A., Bosilovich, M. G., Reichle, R., Wargan, K., Coy, L., Cullather, R., Draper, C., Akella, S., Buchard, V., Conaty, A., da Silva, A. M., Gu, W., Kim, G.-K., Koster, R., Lucchesi, R., Merkova, D., Nielsen, J. E., Partyka, G., Pawson, S., Putman, W., Rienecker, M., Schubert, S. D., Sienkiewicz, M., and Zhao, B.: The Modern-Era Retrospective Analysis for Research and Applications, Version 2 (MERRA-2), J. Climate, 30, 5419–5454, https://doi.org/10.1175/JCLI-D-16-0758.1, 2017.

Geller, M. A., T. Zhou, and W. Yuan: The QBO, gravity waves forced by tropical convection, and ENSO, J. Geophys. Res. Atmos., 121, 8886–8895, doi:10.1002/2015JD024125, 2016.

Gill, A. E.: Atmosphere-Ocean Dynamics, Academic Press, New York, 1982.

Giorgetta, M. A., and Bengtsson, L.: The potential role of the quasi-biennial oscillation in the stratosphere-troposphere exchange as found in water vapor in general circulation model experiments, J. Geophys. Res., 104, 6003–6020, 1999.

GISTEMP Team: GISS Surface Temperature Analysis (GISTEMP), version 4. NASA Goddard Institute for Space Studies. Dataset accessed 2020-09-10 at https://data.giss.nasa.gov/gistemp/, 2020.

GMAO: MERRA-2 inst3_3d_asm_Nv: 3D, 3-hourly, instantaneous, model-level, assimilation, assimilated meteorological fields, version 5.12.4. Greenbelt, MD, USA, Goddard Earth Sciences Data and Information Services Center (GES DISC), Accessed: accessed 1 July 2019, 10.5067/WWQSXQ8IVFW8, 2015.

GPM Science Team: GPM DPR (Gridded Convective Stratiform Heating) L3 1.5 hours 0.5 degree x 0.5 degree V06, Goddard Earth Sciences Data and Information Services Center (GES DISC), accessed 5 June 2017, 10.5067/GPM/DPRGMI/CSH/3G/06, 2017.

Gray, L. J., J. A. Anstey, Y. Kawatani, H. Lu, S. Osprey, and V. Schenzinger: Surface impacts of the Quasi Biennial Oscillation, Atmos. Chem. Phys., 18, 8227–8247, 2018.

Hirota, N., Shiogama, H., Akiyoshi, H., Ogura, T., Takahashi, M., Kawatani, Y., Kimoto, M., and Mori, M.: The influences of El Nino and Arctic sea-ice on the QBO disruption in February 2016, Nature Climate Atmos. Sci., 1, 10, doi:10.1038/s41612-018-0020-1, 2018.

Hitchcock, P., Haynes, P. H., Randel, W. J., and Birner, T.: The emergence of shallow easterly jets within QBO westerlies, J. Atmos. Sci., 75, 21–40, https://doi.org/10.1175/JAS-D-17-0108.1, 2018.

Hamilton, K. P.: Mean wind evolution through the quasi-biennial cycle of the tropical lower stratosphere, J. Atmos. Sci., 41, 2113–2125, 1984.

He, C., Y. Wang, and T. Li: Weakened impact of the developing El Niño on tropical Indian Ocean climate variability under global warming, J. Climate, 32, 7265–7279, https://doi.org/10.1175/JCLI-D-19-0165.1, 2019.

Ho, C., Kim, H., Jeong, J. and Son, S.: Influence of stratospheric quasi-biennial oscillation on tropical cyclone tracks in the western North Pacific, Geophys. Res. Lett., 36, L06702, doi:10.1029/2009GL037163, 2009.

Holton, J. R., and Lindzen, R. S.: An updated theory for the quasi-biennial cycle of the tropical stratosphere, J. Atmos. Sci., 29, 1076–1080, https://doi.org/10.1175/1520-0469(1972)029,1076:AUTFTQ.2.0.CO;2, 1972.

Holton, J. R., and Tan, H.-C.: The influence of the equatorial quasi-biennial oscillation on global circulation at 50 mb, J. Atmos. Sci., 37, 2200–2208, https://doi.org/10.1175/1520-0469(1980)037,2200:TIOTEQ.2.0.CO;2, 1980.

Horinouchi, T., Pawson, S., Shibata, K., Manzini, E., Giorgetta, M., and Sassi, F.: Tropical cumulus convection and upward propagating waves in middle-atmospheric GCMs, J. Atmos. Sci., 60, 2765–2782, 2003.

Huffman, G., Bolvin, D., Braithwaite, D., Hsu, K., Joyce, R., and Xie, P.: Integrated Multi-satellite Retrievals for GPM (IMERG), version 4.4. NASA's Precipitation Processing Center, accessed 31 March 2015, ftp://arthurhou.pps.eosdis.nasa.gov/gpmdata/, 2014.

Jewtoukoff, V., Plougonven, R., and Hertzog, A.: Gravity waves generated by deep tropical convection: Estimates from balloon observations and mesoscale simulations, J. Geophys. Res. Atmos., 118, 9690–9707, https://doi.org/10.1002/jgrd.50781, 2013.

Kang, M.-J., Chun, H.-Y., and Kim, Y.-H.: Momentum flux of convective gravity waves derived from an offline gravity wave parameterization. Part I: Spatiotemporal variations at source level, J. Atmos. Sci., 74, 3167–3189, https://doi.org/10.1175/JAS-D-17-0053.1, 2017.

Kang, M.-J., Chun, H.-Y., Kim, Y.-H., Preusse, P., and Ern, M.: Momentum flux of convective gravity waves derived from an offline gravity wave parameterization. Part II: Impacts on the quasi-biennial oscillation, J. Atmos. Sci., 75, 3753–3775, https://doi.org/10.1175/JAS-D-18-0094.1., 2018.

Kawatani, Y., Watanabe, S., Sato, K., Dunkerton, T. J., Miyahara, S., and Takahashi, M.: The roles of equatorial trapped waves and internal inertia–gravity waves in driving the quasi-biennial oscillation. Part I: Zonal mean wave forcing, J. Atmos. Sci., 67, 963–980, https://doi.org/10.1175/2009JAS3222.1, 2010.

Kawatani, Y., Hamilton, K., Sato, K., Dunkerton, T. J., Watanabe, S., and Kikuchi, K.: ENSO modulation of the QBO: Results from MIROC models with and without nonorographic gravity wave parameterization, J. Atmos. Sci., 76, 3893–3917, 2019.

Kidston, J., A. A. Scaife, S. C. Hardiman, D. M. Mitchell, N. Butchart, M. P. Baldwin, and L. J. Gray: Stratospheric influence on tropospheric jet streams, storm tracks and surface weather, Nat. Geosci., 8, 433–440, 2015.

Kim, Y.-H., and Chun, H.-Y.: Contributions of equatorial wave modes and parameterized gravity waves to the tropical QBO in HadGEM2, J. Geophys. Res. Atmos., 120, 1065–1090, https://doi.org/10.1002/2014JD022174, ~~2015~~2015a.

Kim, Y.-H., and H.-Y. Chun: Momentum forcing of the quasi-biennial oscillation by equatorial waves in recent reanalyses. Atmos. Chem. Phys., 15, 6577–6587, doi:10.5194/acp-15-6577-2015, 2015b.

Kim, Y.-H., Kiladis, G. N., Albers, J. R. , Dias, J., Fujiwara, M., Anstey, J. A., Song, I.-S., Wright, C. J., Kawatani, Y., Lott, F. and Yoo, C.: Comparison of equatorial wave activity in the tropical tropopause layer and stratosphere represented in reanalyses. Atmos. Chem. Phys., 19, 10027–10050, 2019.

Kumar, K. K., Mathew, S. S., and Subrahmanyam, K. V.: Anomalous tropical planetary wave activity during 2015/2016 quasi biennial oscillation disruption, J. Atmos. Sol-Terr. Phys., 167, 184–189, https://doi.org/10.1016/j.jastp.2017.12.004, https://doi.org/10.1016/j.jastp.2017.12.004, 2018.

Lang, S. E., and Tao, W.-K.: The next-generation Goddard convective-stratiform heating algorithm: New tropical and warm-season retrievals for GPM, J. Climate, 31, 5997–6026, 2018.

Lee, J.-H., Kang, M.-J., and Chun, H.-Y.: Differences in the tropical convective activities at the opposite phases of the quasi-biennial oscillation, Asia-Pac. J. Atmos. Sci., 55, 317–336, 2019.

Liess, S., and Geller, M. A.: On the relationship between QBO and distribution of tropical deep convection, J. Geophys. Res., 117, D03108, https://doi.org/10.1029/2011JD016317, 2012.

Li, H., Kedzierski, R. P., Matthes, K.: On the forcings of the unusual Quasi-Biennial Oscillation structure in February 2016., Atmos. Chem. Phys~~.~~, 20, 6541–6561, 2020.

Lin, P., Held, I., and Ming, Y.: The early development of the 2015/16 quasi-biennial oscillation disruption, J. Atmos. Sci., 76, 821–836, https://journals.ametsoc.org/doi/pdf/10.1175/JAS-D-18-0292.1, 2019.

Lindzen, R. S.: Turbulence and stress owing to gravity wave and tidal breakdown, J. Geophys. Res., 86, 9707–9714, https://doi.org/10.1029/JC086iC10p09707, 1981.

Lindzen, R. S., and Holton, J. R.: A theory of the quasi-biennial oscillation, J. Atmos. Sci., 25, 1095–1107, https://doi.org/10.1175/1520-0469(1968)025,1095:ATOTQB.2.0.CO;2, 1968.

Marshall, A. G., Hendon, H. H., Son, S.-W., and Lim, Y.: Impact of the quasi-biennial oscillation on predictability of the Madden-Julian oscillation, Climate Dyn., 49, 1365–1377, https://doi.org/10.1007/s00382-016-3392-0, 2017.

Newman, P. A., Coy, L., Pawson, S. and Lait, L. R.: The anomalous change in the QBO in 2015-2016, Geophys. Res. Lett., 43, 8791–8797, https://doi.org/10.1002/2016GL070373, 2016.

Osprey, S. M., Butchart, N., Knight, J. R., Scaife, A. A., Hamilton, K., Anstey, J. A., Schenzinger, V., and Zhang, C.: An unexpected disruption of the atmospheric quasi-biennial oscillation, Science, 353, 1424–1427, https://doi.org/10.1126/science.aah4156, 2016.

O'Sullivan, D.: Interaction of extratropical Rossby waves with westerly quasi-biennial oscillation winds, J. Geophys. Res., 102, 19461–19469, https://doi.org/10.1029/97JD01524, 1997.

Patra, P. K., Lal, S., Venkataramani, S., Chand, D.: Halogen Occultation Experiment (HALOE) and balloon-borne in situ measurements of methane in stratosphere and their relation to the quasi-biennial oscillation (QBO), Atmos. Chem. Phys., 3 (4), 1051–1062, 2003.

Randel, W. J., and Wu, F.: Isolation of the ozone QBO in SAGE II data by singular-value decomposition, J. Atmos. Sci., 53(17), 2546–2559, 1996.

Richter, J. H., Solomon, A., and Bacmeister, J. T.: On the simulation of the quasi-biennial oscillation in the Community Atmosphere Model, version 5, J. Geophys. Res. Atmos., 119, 3045–3062, https://doi.org/10.1002/2013JD021122, 2014.

Richter, J. H., Butchart, N., Kawatani, Y., Bushell, A. C., Holt, L., Serva., F., Anstey, J., Simipson, I. R., Osprey, S., Hamilton, K., Braesicke, P., Cagnazzo, C., Chen, C.-C., Garcia, R. R., Gray, L. J., Kerzenmacher, T., Lott, F., McLandress, C., Naoe, H., Scinocca, J., Stockdale, T. N., Versick, S., Watanabe. S., Yoshida, K., Yukimoto, S.: Response of the quasi-biennial oscillation to a warming climate in global climate models, Q. J. R. Meteorol. Soc., https://doi.org/10.1002/qj.3749, 2020.

Saha, S., Moorthi, S., Pan, H.-L., Wu, X., Wang, J., Nadiga, S., Tripp, P., Kistler, R., Woollen, J., Behringer, D., Liu, H., Stokes, D., Grumbine, R., Gayno, G., Wang, J., Hou, Y.-T., Chuang, H.-Y., Juang, H.-M. H., Sela, J., Iredell, M., Treadon, R., Kleist, D., Van Delst, P., Keyser, D., Derber, J., Ek, M., Meng, J., Wei, H., Yang, R., Lord, S., van den Dool, H., Kumar, A., Wang, W., Long, C., Chelliah, M., Xue, Y., Huang, B., Schemm, J.-K., Ebisuzaki, W., Lin, R., Xie, P., Chen, M., Zhou, S., Higgins, W., Zou, C.-Z., Liu, Q., Chen, Y., Han, Y., Cucurull, L., Reynolds, R. W., Rutledge, G., and Goldberg, M.: The NCEP Climate Forecast System Reanalysis, B. Am. Meteorol. Soc., 91, 1015–1057, 2010

Scaife, A. A., Athanassiadou, M., Andrews, M., Arribas, A., Baldwin, M., Dunstone, N., Knight, J., MacLachlan, C., Manzini, E., Müller, W. A., Pohlmann, H., Smith, D., Stockdale, T., and Williams, A.: Predictability of the quasi-biennial oscillation and its northern winter teleconnection on seasonal to decadal timescales, Geophys. Res. Lett., 41, 1752–1758, 2014.

Song, I.-S., and Chun, H.-Y.: Momentum flux spectrum of convectively forced internal gravity waves and its application to gravity wave drag parameterization. Part I: Theory, J. Atmos. Sci., 62, 107–124, https://doi.org/10.1175/JAS-3363.1, 2005.

Watanabe, S., and Miyahara, S.: Quantification of the gravity wave forcing of the migrating diurnal tide in a gravity wave-resolving general circulation model, J. Geophys. Res., 114, D07110, https://doi.org/10.1029/2008JD011218, 2009.

Watanabe, S., Hamilton, K., Osprey, S., Kawatani, Y., and Nishimoto, E.: First successful hindcast of the 2016 disruption of the stratospheric quasi-biennial oscillation, Geophys. Res. Lett., 45, 1602–1610, https://doi.org/10.1002/2017GL076406, 2018.

Wheeler, M., and Kiladis, G. N.: Convectively coupled equatorial waves: Analysis of clouds and temperature in the wavenumber–frequency domain, J. Atmos. Sci., 56(3), 374–399, 1999.

Yang, G., Hoskins, B., and Slingo, J.: Equatorial waves in opposite QBO phases, J. Atmos. Sci., 68, 839–862, doi:10.1175/2010JAS3514.1, 2011.

Yoo, C., and Son, S.-W.: Modulation of the boreal wintertime Madden-Julian oscillation by the stratospheric quasi-biennial oscillation, Geophys. Res. Lett., 43, 1392–1398, https://doi.org/10.1002/2016GL067762, 2016.

Table 1. Momentum forcing at 40 hPa by each wave (m s^{-1} mon^{-1}) and its percentage to the total negative wave forcing (parenthesis) averaged over 5°N–5°S from October 2015 to March 2016 and for the climatology. The percentage is calculated when a wave forcing is negative during the QBO disruption.

2015–16	**Oct 2015**	**Nov 2015**	**Dec 2015**	**Jan 2016**	**Feb 2016**	**Mar 2016**
MRG	-0.4 (39%)	-0.6 (27%)	-0.6 (17%)	-0.1 (1%)	-0.6 (12%)	-0.5 (10%)
IG	-0.5 (41%)	-0.6 (28%)	-0.5 (13%)	-0.4 (8%)	-0.3 (7%)	-0.4 (7%)
Rossby	-0.2 (20%)	-0.9 (45%)	-2.6 (70%)	-4.4 (91%)	-3.0 (61%)	-1.3 (23%)
CGW	0.8	0.6	0.3	0.5	-1.0 (20%)	-3.3 (60%)
Kelvin	0.9	0.6	0.7	1.1	0.7	0.5
Rossby-Y	-0.3 (30%)	-0.7 (34%)	-1.9 (52%)	-3.8 (78%)	-2.7 (55%)	-1.4 (25%)
Rossby-Z	0.03	-0.2 (11%)	-0.7 (18%)	-0.6 (13%)	-0.3 (6%)	0.1
Climatology	**Oct**	**Nov**	**Dec**	**Jan**	**Feb**	**Mar**
MRG	-0.3	-0.2	-0.2	-0.2	-0.1	-0.1
IG	-0.2	-0.4	-0.4	-0.4	-0.3	-0.4
Rossby	-0.3	-0.4	-0.8	-1.0	-1.1	-0.8
CGW	1.0	0.6	0.5	0.5	0.5	0.5
Kelvin	1.6	1.2	1.0	1.0	1.0	0.9
Rossby-Y	-0.2	-0.3	-0.6	-0.8	-0.9	-0.6
Rossby-Z	-0.1	-0.1	-0.2	-0.2	-0.2	-0.2

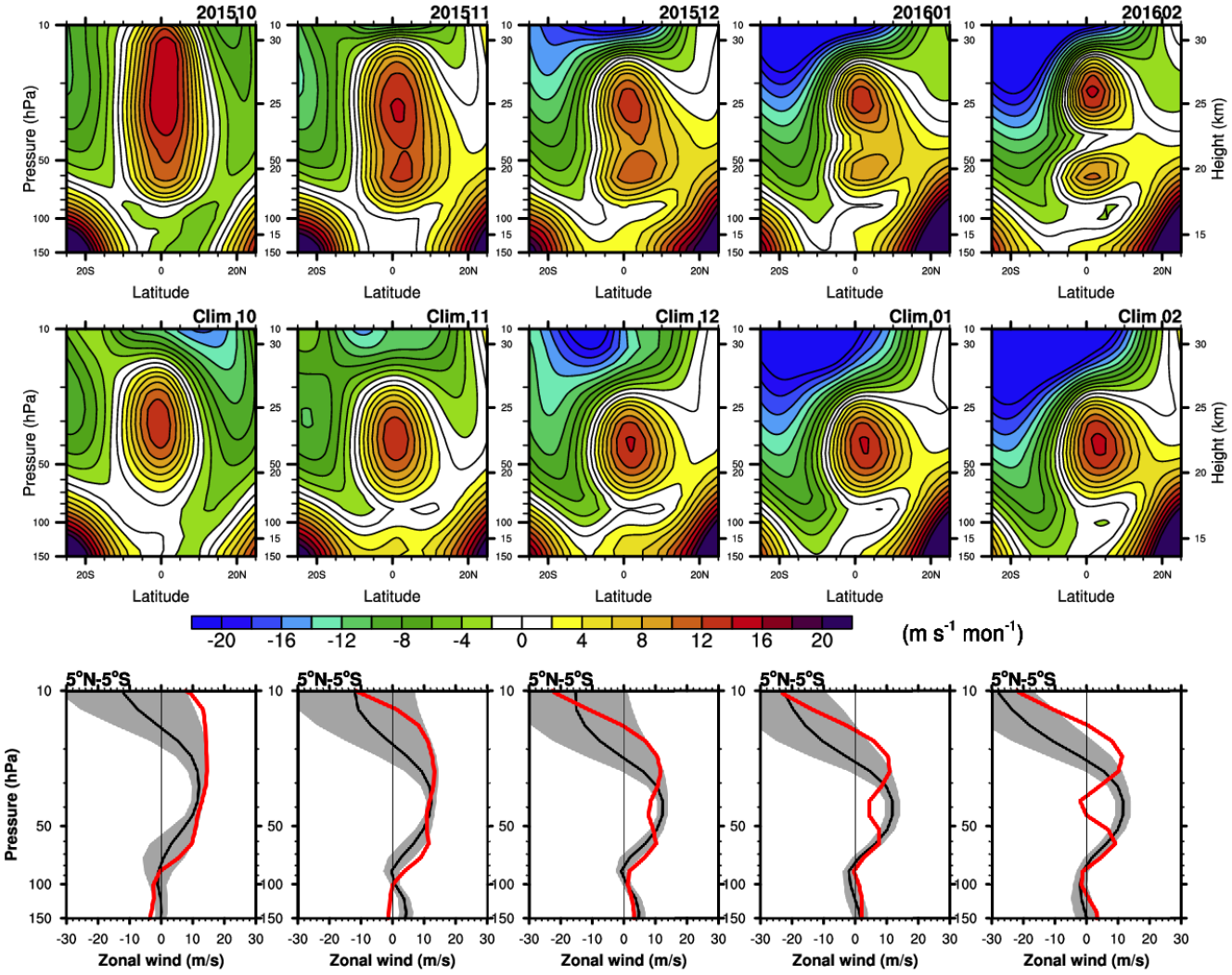
201510
201511
201512
201601
201602
Clim 10
Clim 11
Clim 12
Clim 01
Clim 02
Pressure (hPa)
Height (km)
Latitude
20S
0
20N
-20 -16 -12 -8 -4 0 4 8 12 16 20
(m s-1 mon-1)
5°N-5°S
Zonal wind (m/s)

820

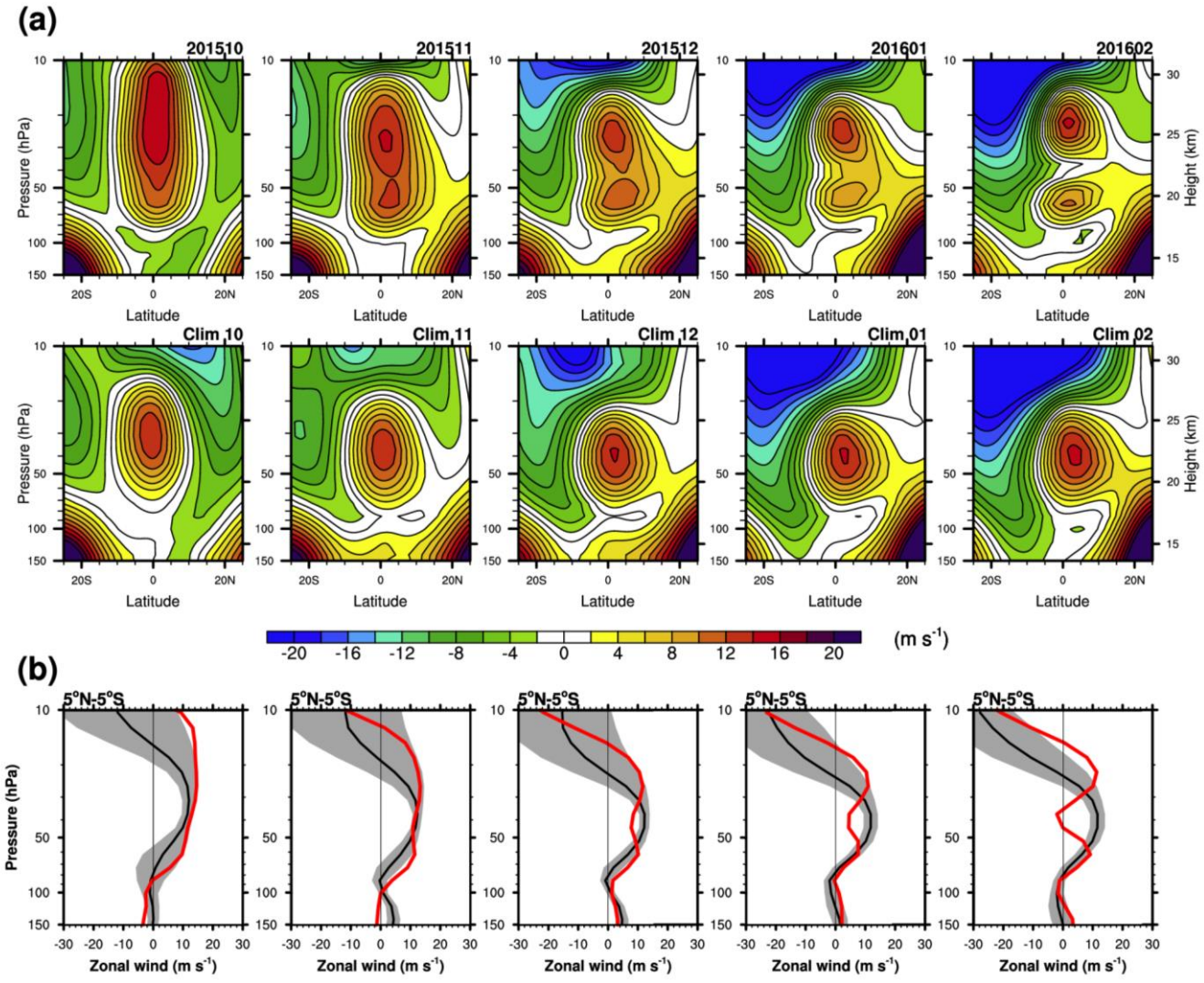

Figure 1. (a) (Top) Latitude–height cross sections of the zonal-mean zonal wind from October 2015 to February 2016, ~~(middle~~ and ~~(bottom)~~ their climatology in each month from October to February~~, and (bottom) those~~. (b) Zonal-mean zonal wind averaged between 5°N and 5°S from October 2015 to February 2016. Red lines represent the QBO disruption and black lines represent the climatology with ± 1 standard deviation (gray shading). Note that the climatology is for WQBO years.

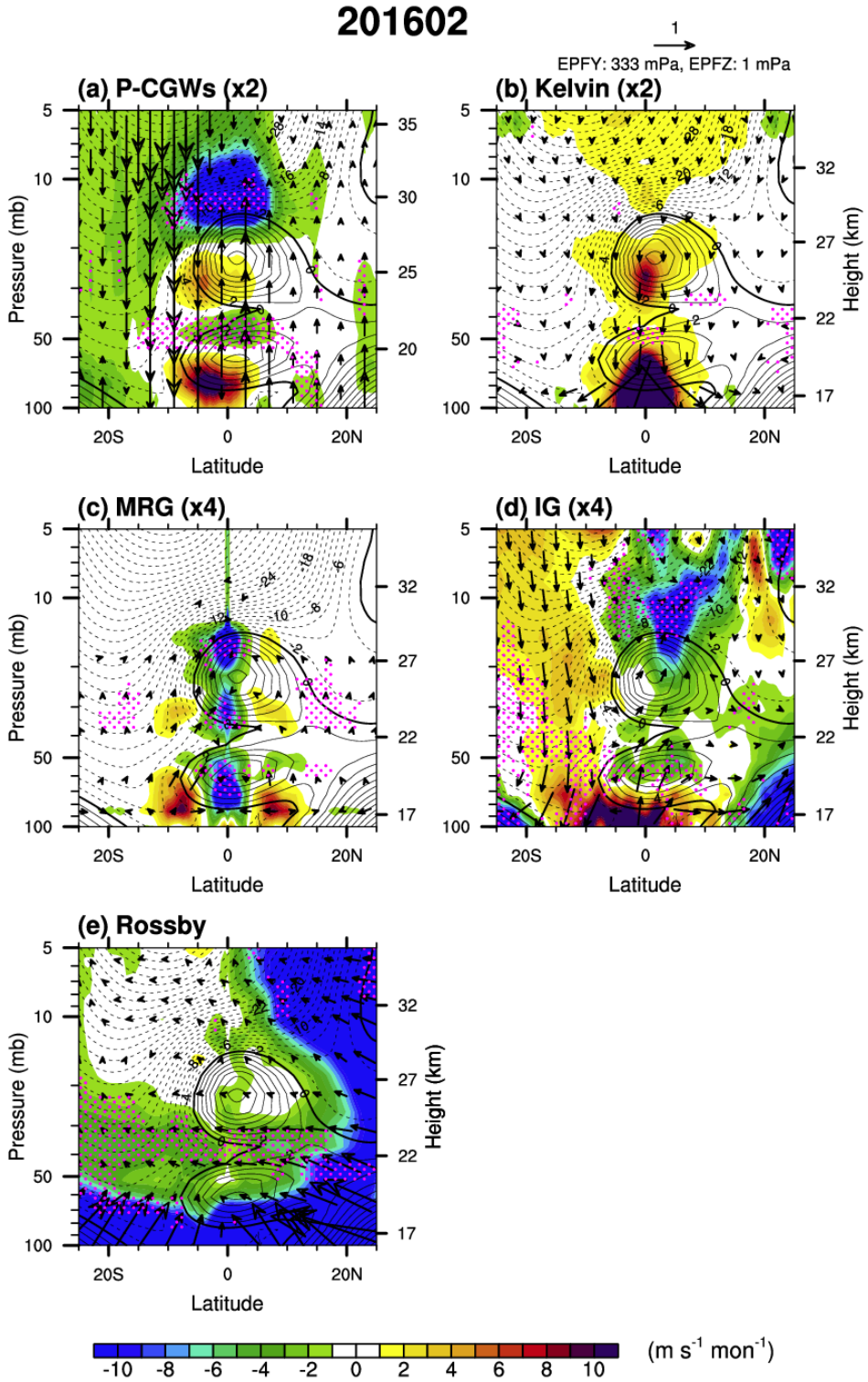
201602
1
EPFY: 333 mPa, EPFZ: 1 mPa
(a) P-CGWs (x2)
(b) Kelvin (x2)
(c) MRG (x4)
(d) IG (x4)
(e) Rossby
Pressure (mb)
Height (km)
Latitude
20S
0
20N
5
10
50
100
35
30
25
20
32
27
22
17
-10 -8 -6 -4 -2 0 2 4 6 8 10
(m s-1 mon-1)

Figure 2. Latitude–height cross sections of the EPF (vectors) and EPD (shading) for the (a) parameterized CGWs (P-CGWs, multiplied by 2) and resolved equatorial waves, including (b) Kelvin (multiplied by 2), (c) MRG (multiplied by 4), (d) inertia-gravity (IG, multiplied by 4), and (e) Rossby waves, superimposed on the zonal-mean zonal wind (contour) in February 2016. Positive (negative) zonal winds are plotted with solid (dashed) lines with a contour interval of 2 m s^{-1}, and thick contour lines denote a zero zonal wind speed. The magenta stippled pattern represents a region where the EPD is algebraically smaller (more negative) than the climatology by more than its standard deviation. The arrow on the upper right corner denotes the reference vector.

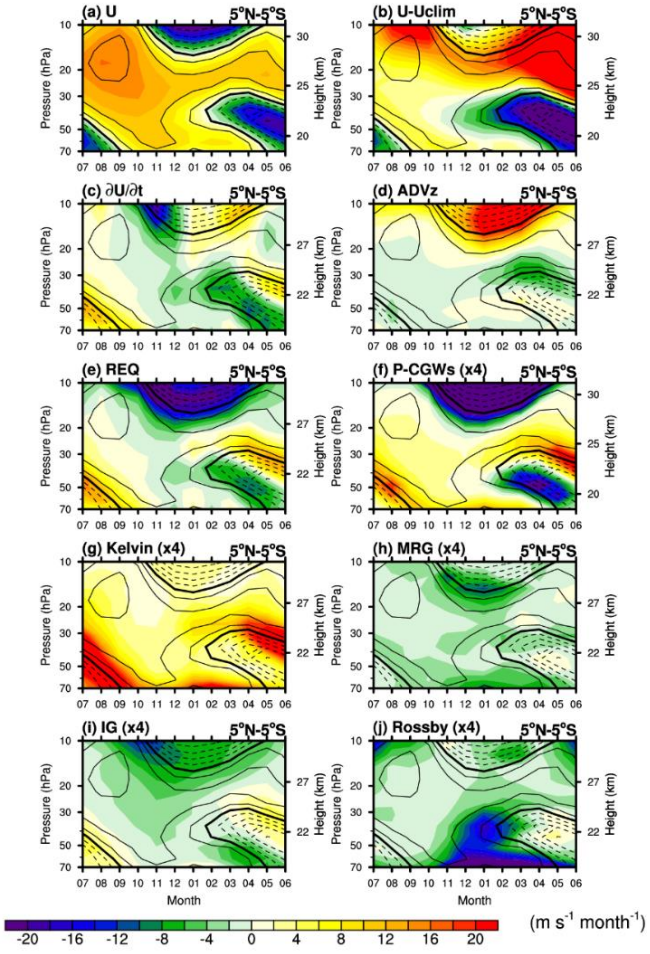
2015/16
(a) U
5°N-5°S
(b) U-Uclim
5°N-5°S
(c) ∂U/∂t
5°N-5°S
(d) ADVz
5°N-5°S
(e) REQ
5°N-5°S
(f) P-CGWs (x4)
5°N-5°S
(g) Kelvin (x4)
5°N-5°S
(h) MRG (x4)
5°N-5°S
(i) IG (x4)
5°N-5°S
(j) Rossby (x4)
5°N-5°S
Pressure (hPa)
Height (km)
Month
07 08 09 10 11 12 01 02 03 04 05 06
-20 -16 -12 -8 -4 0 4 8 12 16 20
(m s-1 month-1)

Climatology

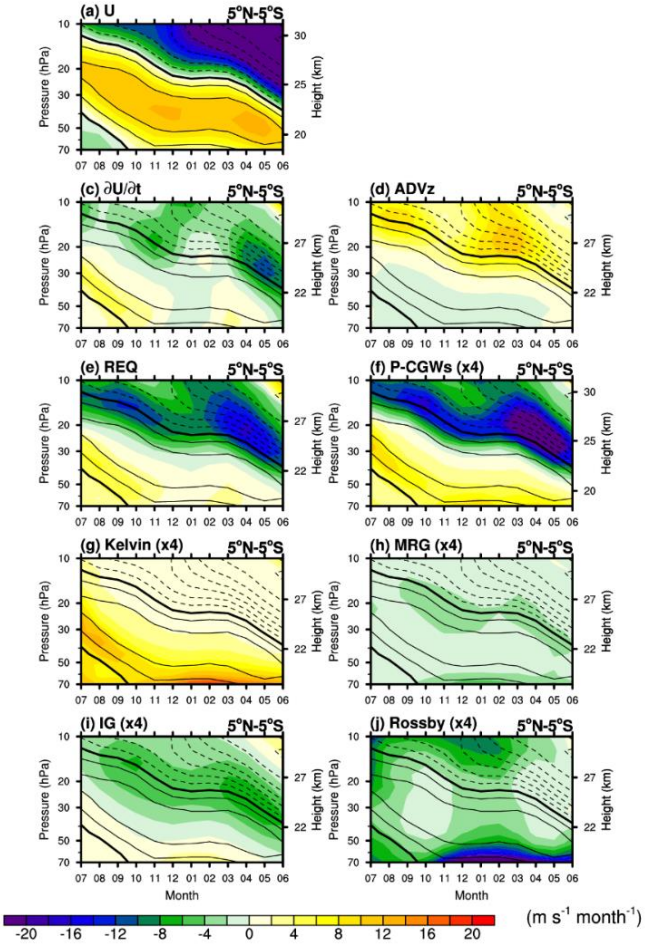

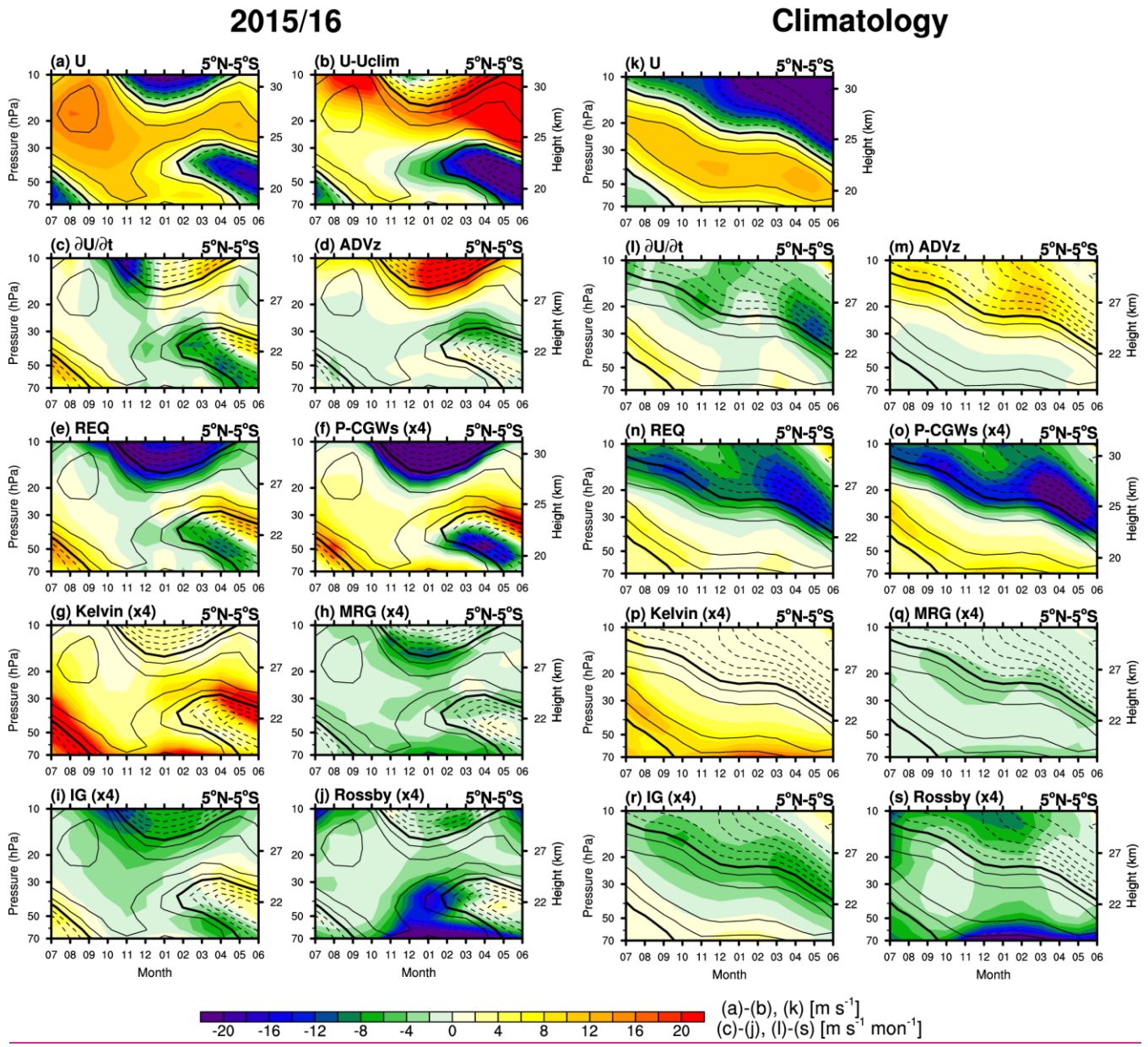

845 **Figure 3.** Time–height cross sections of the (a) zonal-mean zonal wind (U), (b) zonal wind anomaly from the climatology (U-Uclim), (c) zonal wind tendency ($\boldsymbol{\partial U/\partial t}$), (d) vertical advection (ADVz), (e) required wave forcing (REQ) in the TEM equation, and EPD for the (f) P-CGWs, (g) Kelvin, (h), MRG, (i) IG, and (j) Rossby waves (left) from July 2015 to June 2016 and ~~(right~~ (k-s) their climatology from July to June, overlaid with the zonal-mean zonal wind (black contour lines). Positive

(negative) zonal winds are plotted with solid (dashed) lines with a contour interval of 5 m s^{-1}, and thick contour lines denote a zero zonal wind speed.

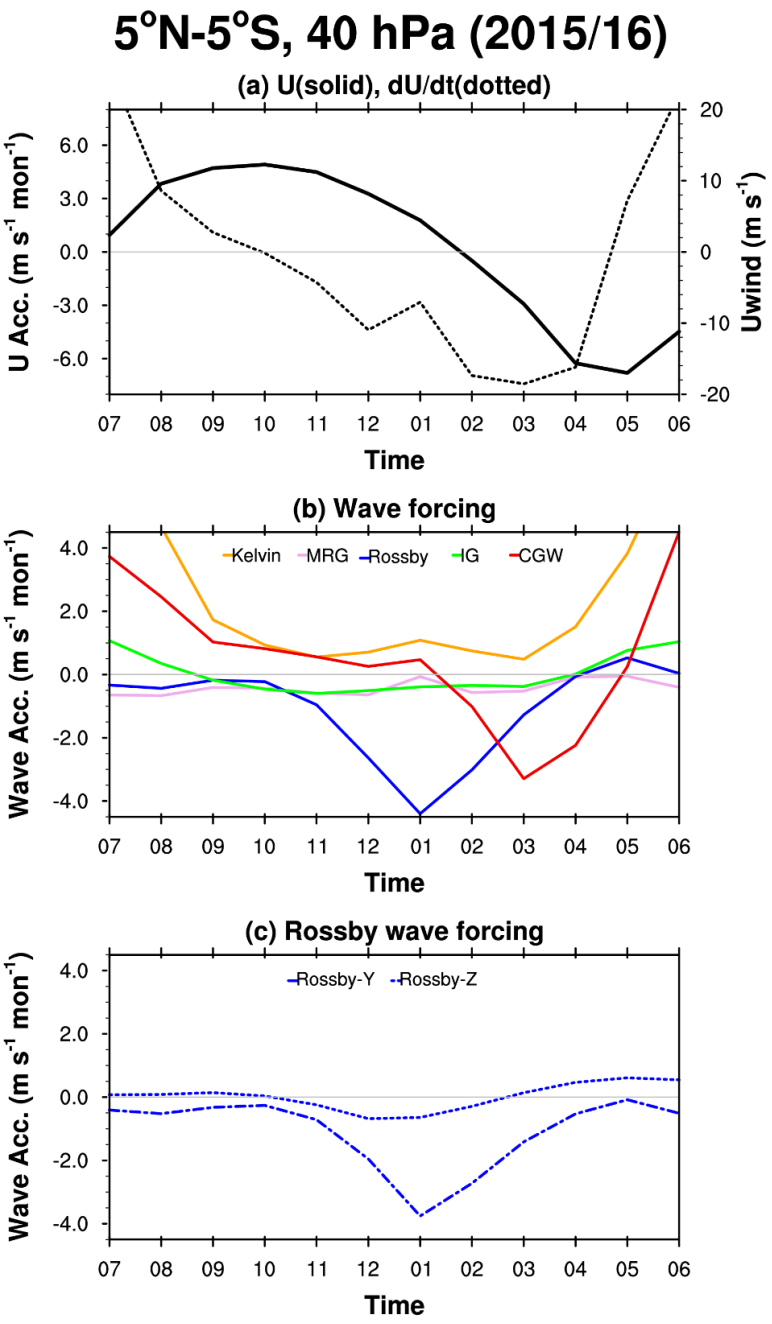
5°N-5°S, 40 hPa (2015/16)
(a) U(solid), dU/dt(dotted)
U Acc. (m s-1 mon-1)
Uwind (m s-1)
6.0
3.0
0.0
-3.0
-6.0
20
10
0
-10
-20
07 08 09 10 11 12 01 02 03 04 05 06
Time
(b) Wave forcing
Kelvin MRG Rossby IG CGW
Wave Acc. (m s-1 mon-1)
4.0
2.0
0.0
-2.0
-4.0
07 08 09 10 11 12 01 02 03 04 05 06
Time
(c) Rossby wave forcing
Rossby-Y Rossby-Z
Wave Acc. (m s-1 mon-1)
4.0
2.0
0.0
-2.0
-4.0
07 08 09 10 11 12 01 02 03 04 05 06
Time

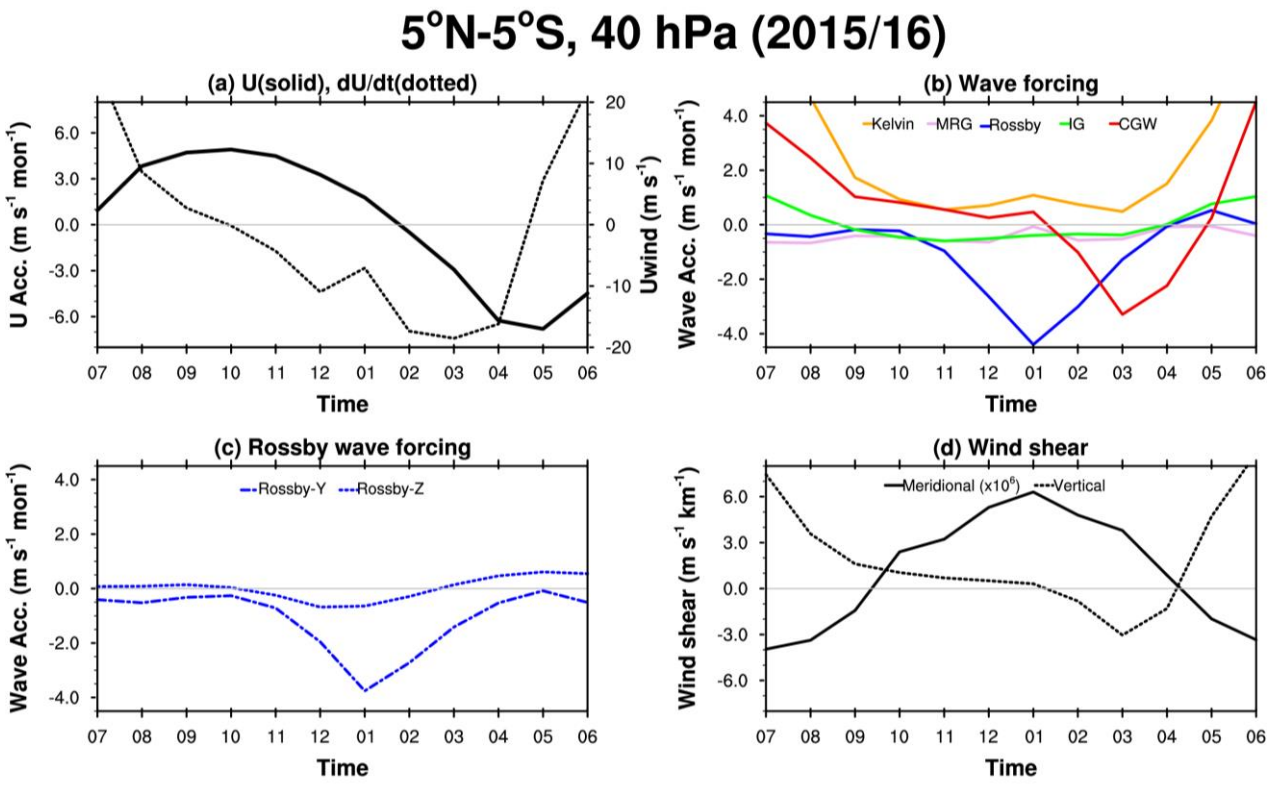

Figure 4. Time series of the (a) zonal-mean zonal wind (solid) and zonal wind tendency (dotted), (b) wave forcing by the Kelvin waves (orange), MRG waves (pink), Rossby waves (blue), IG waves (light green), and CGWs (red), ~~and~~ (c) meridional (dot-dashed) and vertical components (dotted) of the Rossby wave forcing, and (d) meridional wind shear across the equator (solid) and vertical wind shear averaged over 5°N–5°S (dotted) at 40 hPa from July 2015 to June 2016.

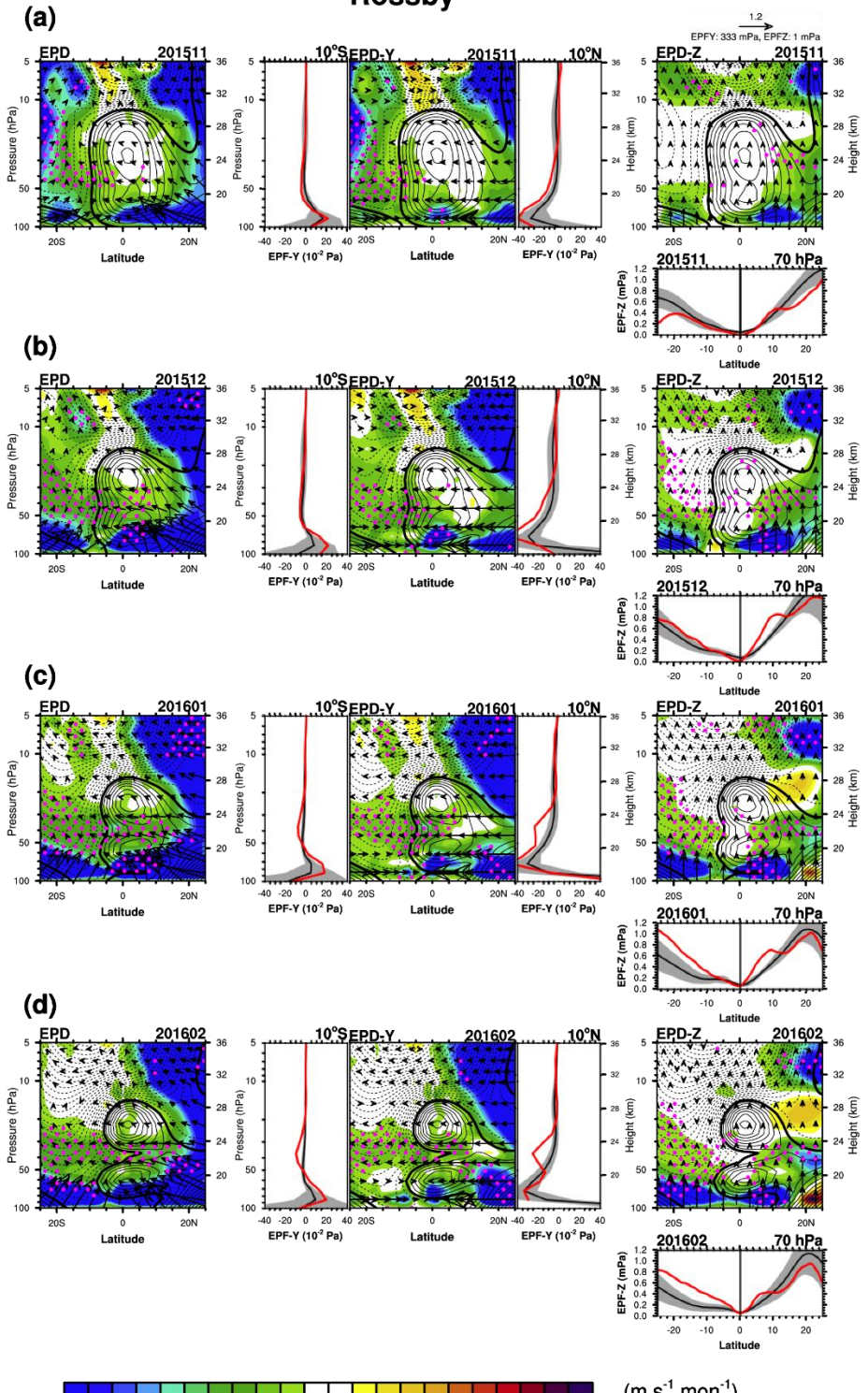
Rossby
(a)
(b)
(c)
(d)
EPD
EPD-Y
EPD-Z
201511
201512
201601
201602
10°S
10°N
EPFY: 333 mPa, EPFZ: 1 mPa
70 hPa
Pressure (hPa)
Height (km)
Latitude
EPF-Y (10⁻² Pa)
EPF-Z (mPa)
(m s⁻¹ mon⁻¹)
-10 -8 -6 -4 -2 0 2 4 6 8 10

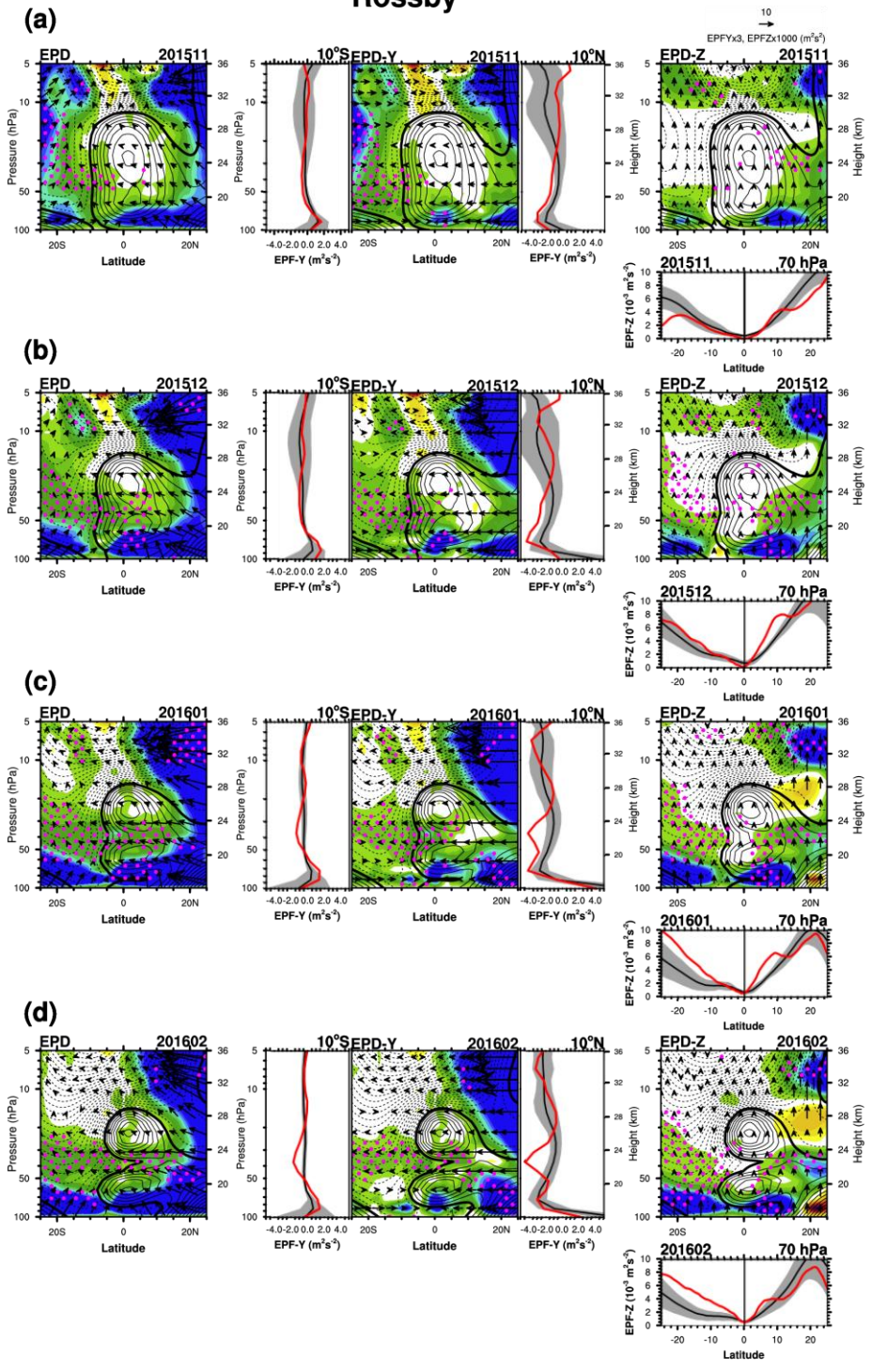
Rossby
(a)
(b)
(c)
(d)
EPD
EPD-Y
EPD-Z
201511
201512
201601
201602
10°S
10°N
70 hPa
EPFYx3, EPFZx1000 (m²s²)
Pressure (hPa)
Height (km)
Latitude
EPF-Y (m²s⁻²)
EPF-Z (10⁵ m²s⁻²)
(m s⁻¹ mon⁻¹)
-10 -8 -6 -4 -2 0 2 4 6 8 10

Figure 5. Latitude–height cross sections of the (1st column) EP flux (vectors) divided by air density and EP flux divergence (EPD, shading) for the Rossby waves, (2nd column) their meridional component, and (3rd column) their vertical component in (a) November 2015, (b) December 2015, (c) January 2016, and (d) February 2016. The panel on the left (right) side of the meridional component represents the meridional EP fluxes at 10°S (10°N) and the panel under the vertical component represents the vertical EP flux at 70 hPa [red lines for each month and black lines for their monthly climatology with ±1 standard deviation (gray shading)]. Positive (negative) zonal winds are plotted with solid (dashed) lines with a contour interval of 2 m s^{-1}, and thick contour lines denote a zero zonal wind speed. The magenta stippled pattern represents a region where the EPD is algebraically smaller ~~than~~(more negative) the climatology by more than its standard deviation.

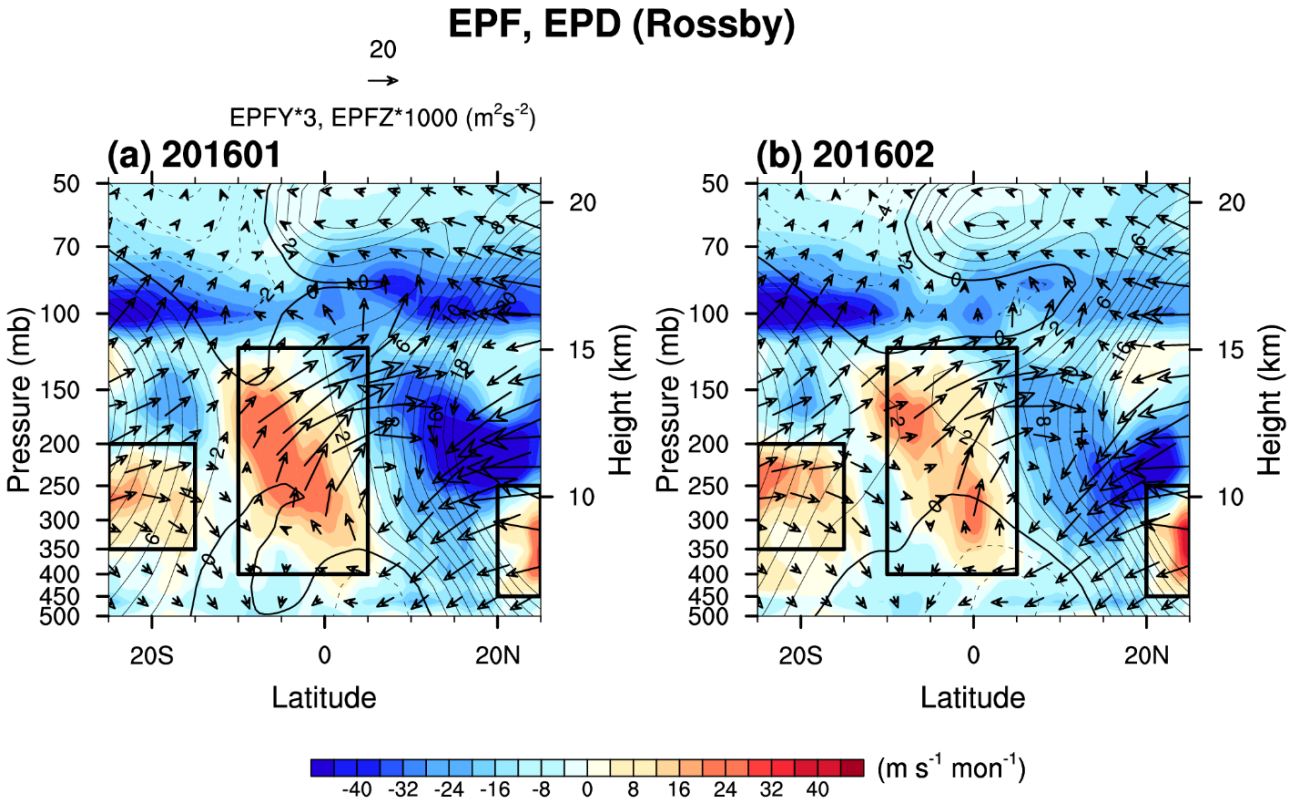

875 **Figure 6.** Latitude–height cross sections of the EP flux (vectors) divided by air density and EP flux divergence (shading) for the Rossby waves and in (a) January 2016 and (b) February 2016. Note that below 100 hPa, the $\boldsymbol{L_w}$ waves ($\boldsymbol{\omega} \leq 0.4$ cpd and $-20 \leq \boldsymbol{k} < 0$) are assumed to be the Rossby waves. Black boxes denote the three-potential source regions.

MRG

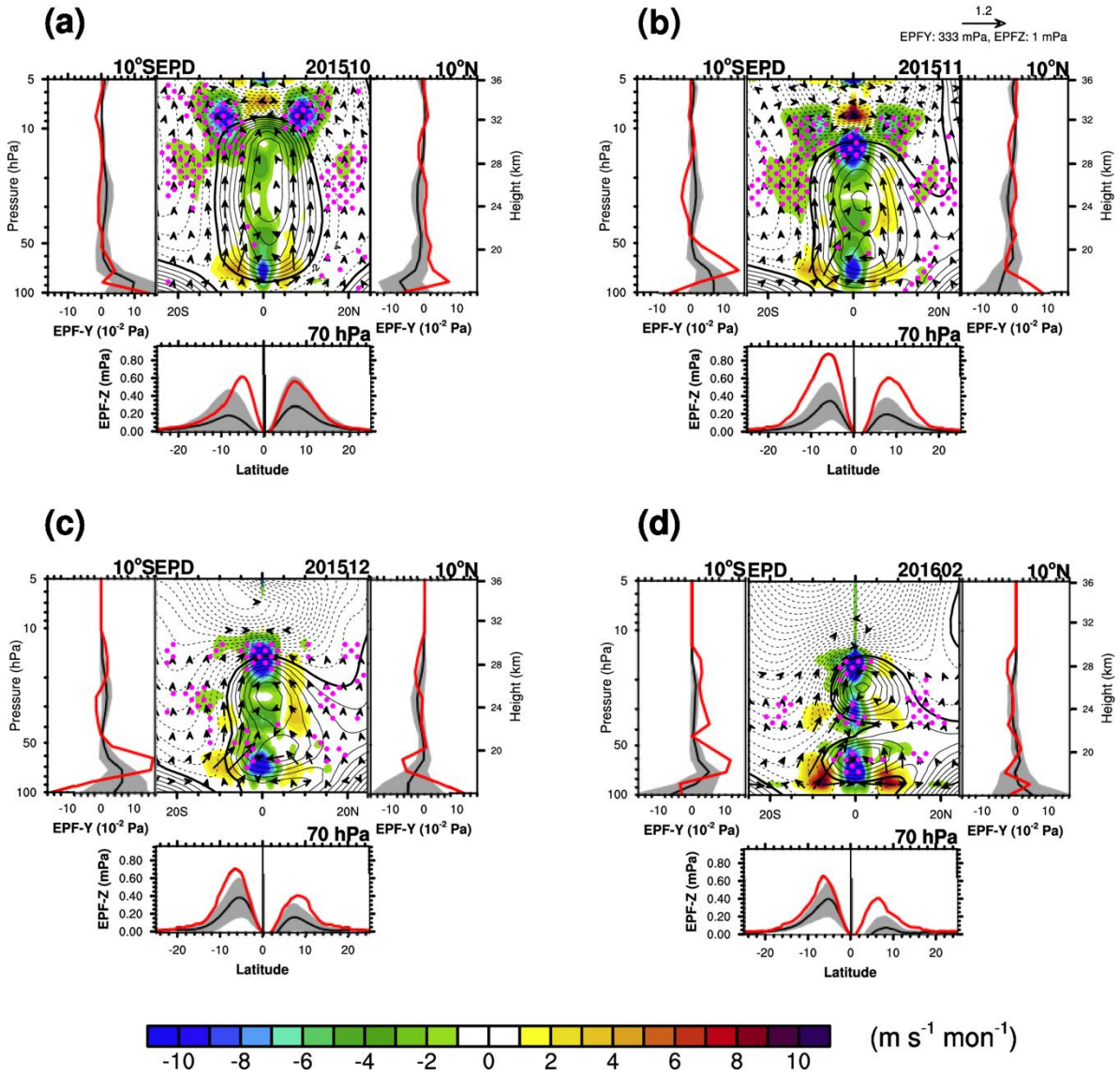
(a)
10°SEPD
201510
10°N
(b)
1.2
EPFY: 333 mPa, EPFZ: 1 mPa
10°SEPD
201511
10°N
(c)
10°SEPD
201512
10°N
(d)
10°SEPD
201602
10°N
Pressure (hPa)
Height (km)
EPF-Y (10^-2 Pa)
70 hPa
EPF-Z (mPa)
Latitude
20S
0
20N
(m s^-1 mon^-1)
-10 -8 -6 -4 -2 0 2 4 6 8 10

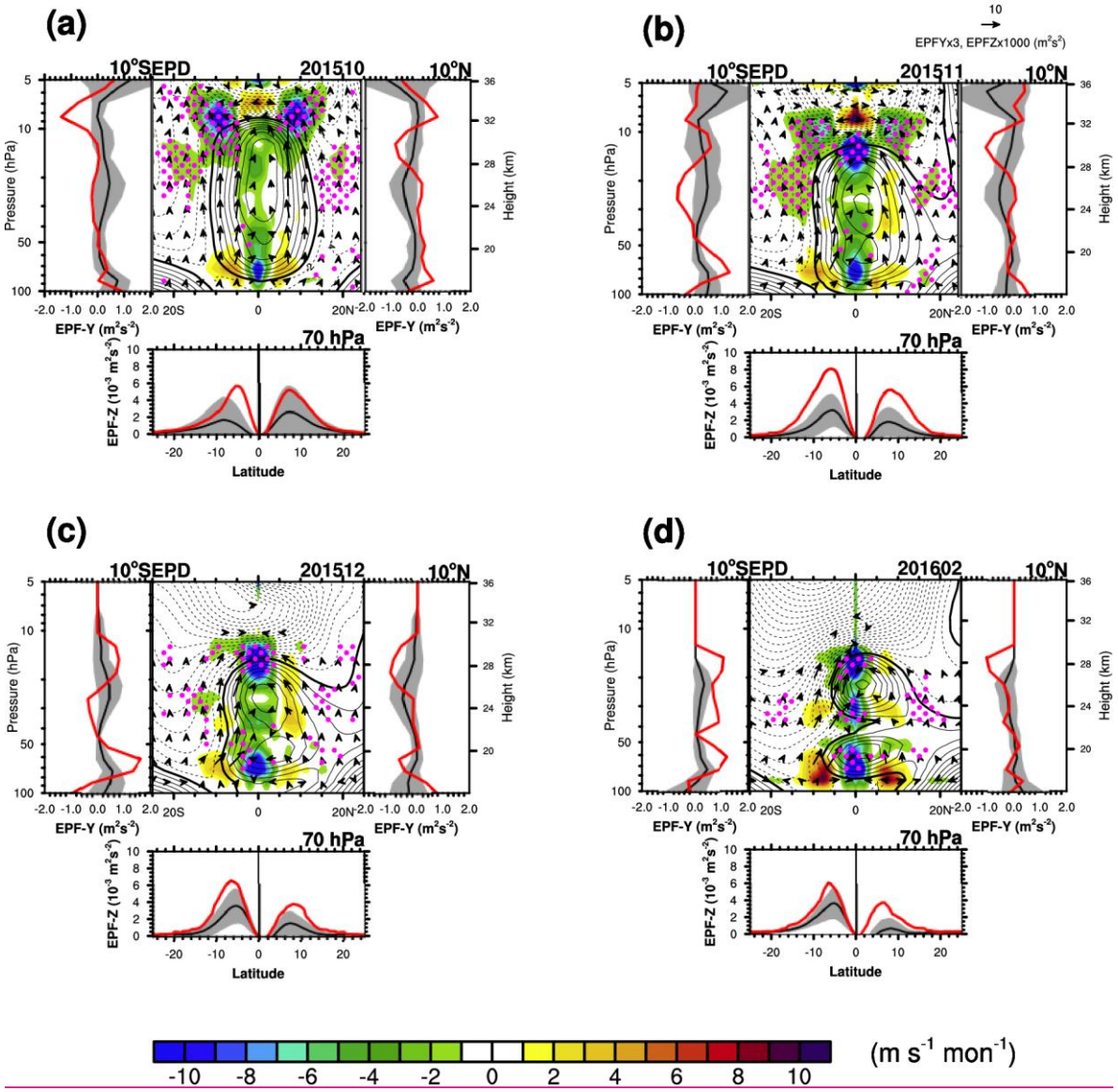

Figure 7. Latitude–height cross sections of the EP flux (vectors) and EP flux divergence (EPD, shading) for the MRG waves, in (a) October 2015, (b) November 2015, (c) ~~January 2016~~December 2015, and (d) February 2016. The panel on the left (right) side of the EPD represents the meridional EP fluxes at 10°S (10°N) and the panel under the EPD represents the vertical EP flux at 70 hPa [red lines for each month and black lines for their monthly climatology with ±1 standard deviation (gray shading)]. Positive (negative) zonal winds are plotted with solid (dashed) lines with a contour interval of 2 m s^{-1}, and thick contour lines denote a zero zonal wind speed. The magenta stippled pattern represents a region where the EPD is algebraically

smaller (more negative) than the climatology by more than its standard deviation. Here, EPF and EPD are multiplied by 8 and 4, respectively.

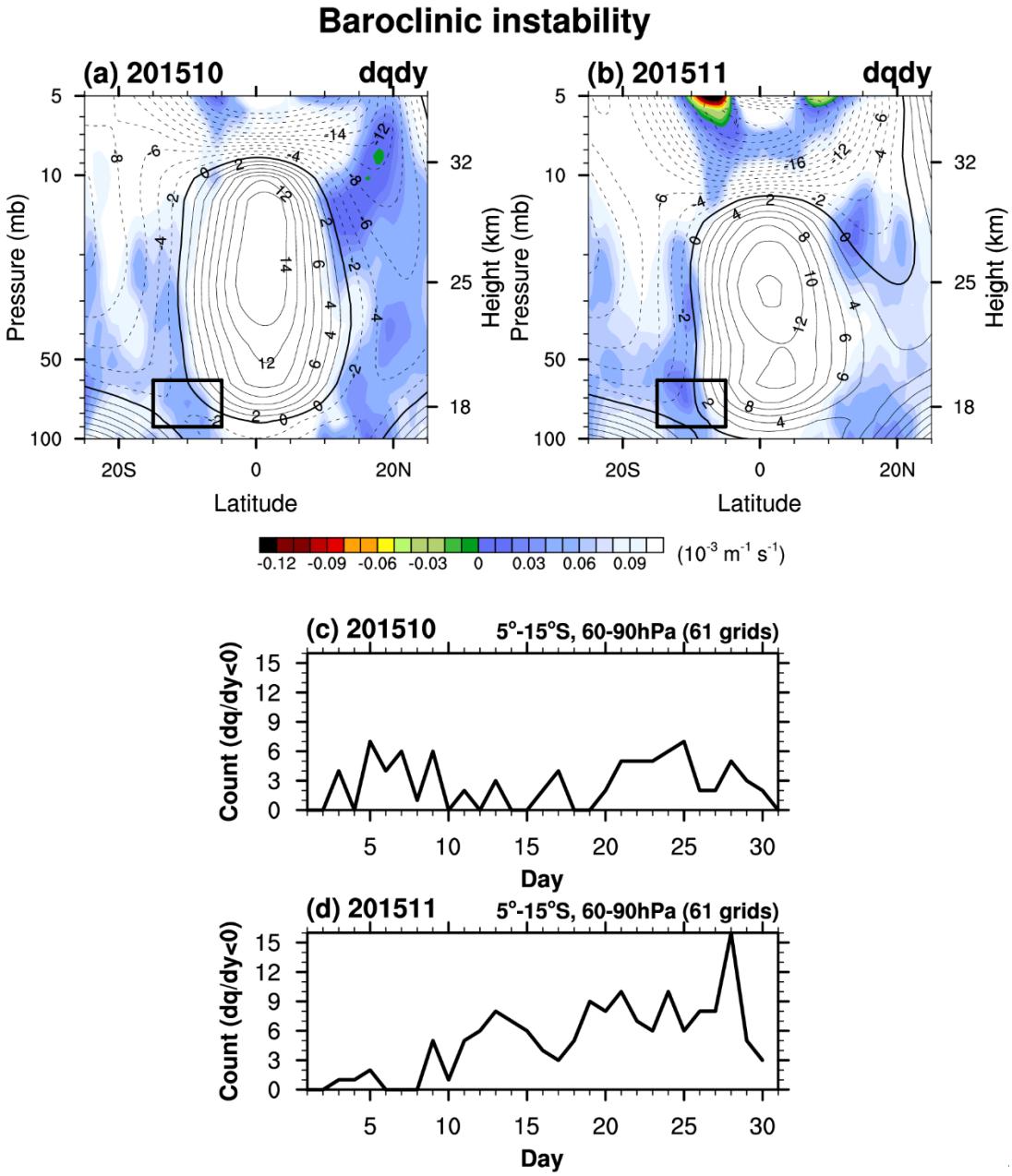

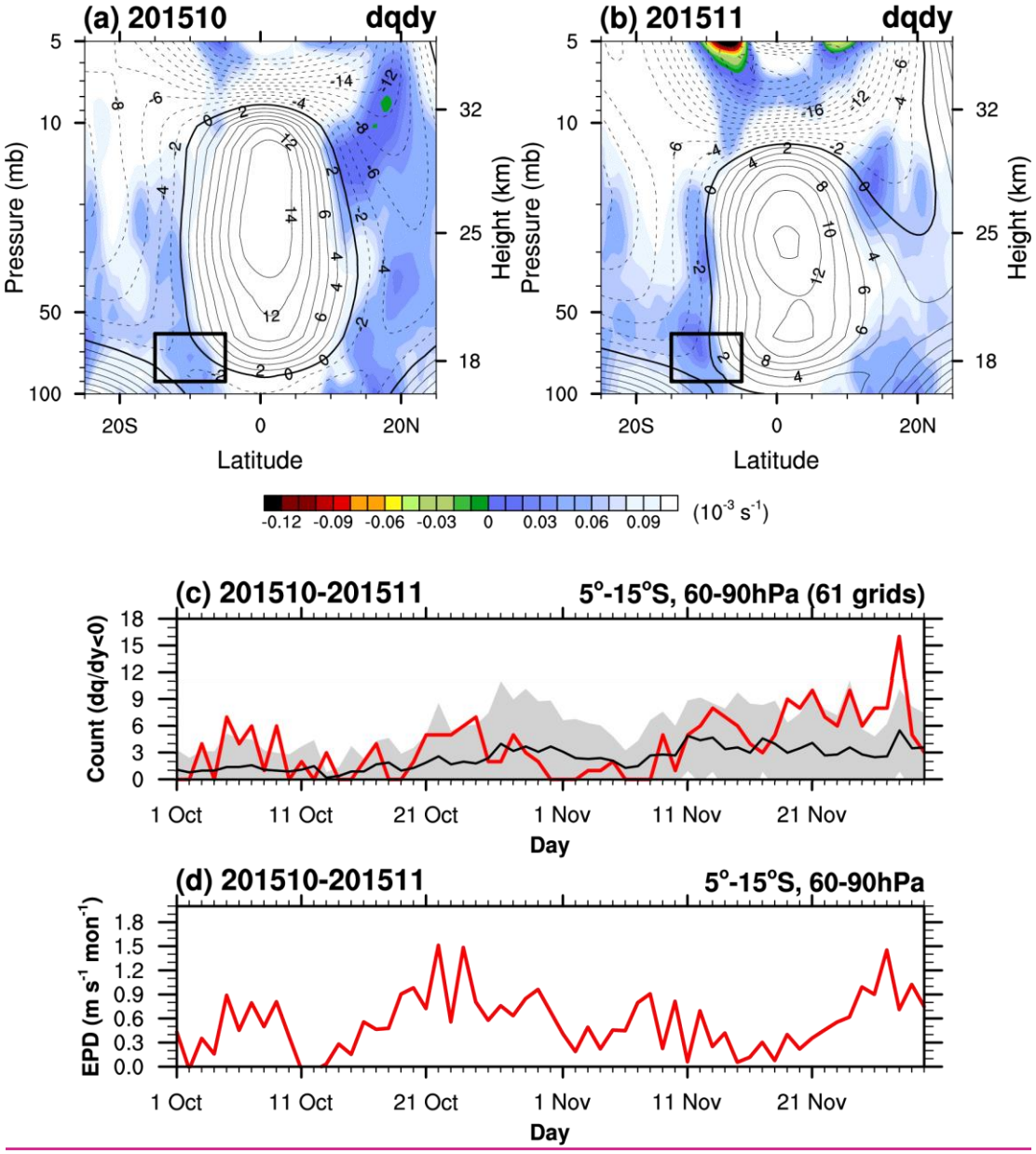

890 **Figure 8.** Latitude–height cross sections of the monthly-mean ~~baroclinic~~barotropic instability (shading) superimposed on the zonal-mean zonal wind (contour) in (a) October 2015 and (b) November 2015. Positive (negative) zonal winds are plotted with solid (dashed) lines with a contour interval of 2 m s^{-1}, and thick contour lines denote a zero-zonal wind speed. Daily time series of the (c) number of grids where daily-mean $\overline{q}_{\phi}$ (s^{-1}) is negative in the boxed region (5°–15°S, 60–90 hPa) ~~in (c) October 2015~~ and (d) those of the EPD for the MRG waves averaged over the boxed region in October–November 2015~~.~~ (red). Black lines
895 in Fig. 8c is for the climatology with ±1 standard deviation (gray shading)

900

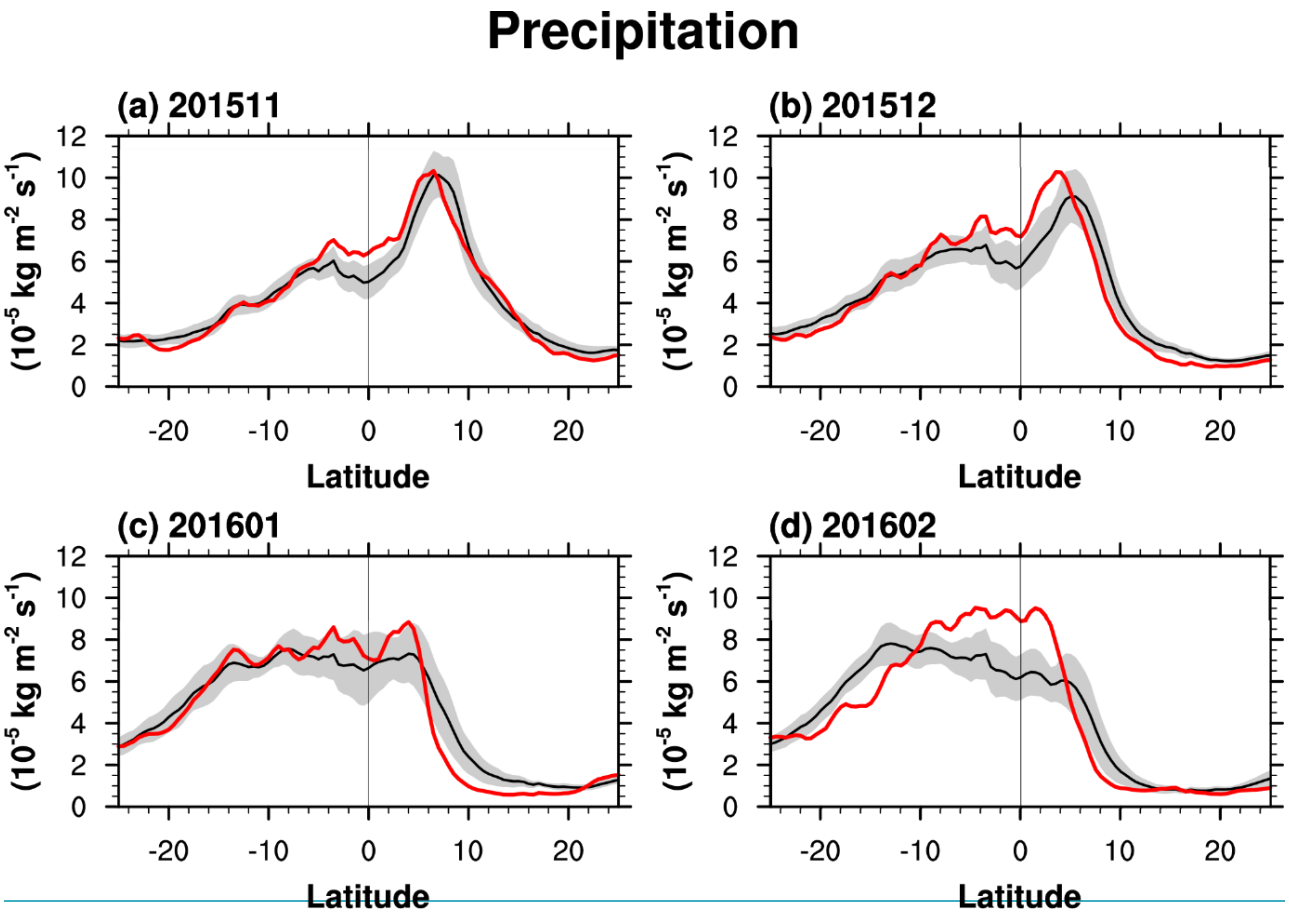
Precipitation
(a) 201511
(b) 201512
(c) 201601
(d) 201602
(10^-5 kg m^-2 s^-1)
Latitude
0
2
4
6
8
10
12
-20
-10
0
10
20

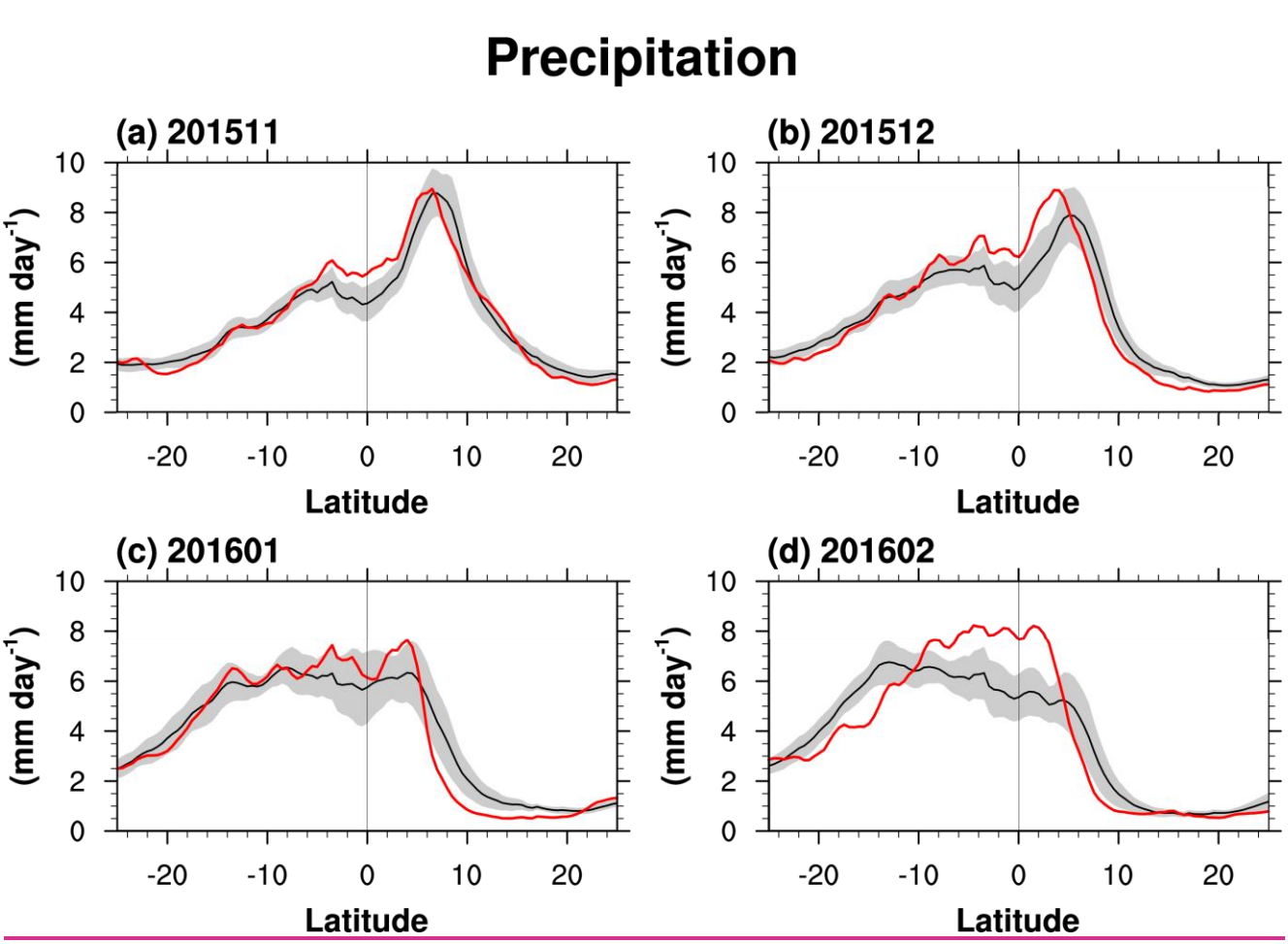

Figure 9. Zonal-mean precipitation of MERRA-2 in (a) November 2015, (b) December 2015, (c) January 2016, and (~~b~~d) February 2016 (red) and their monthly climatology (black) with ± 1 standard deviation (gray shading).

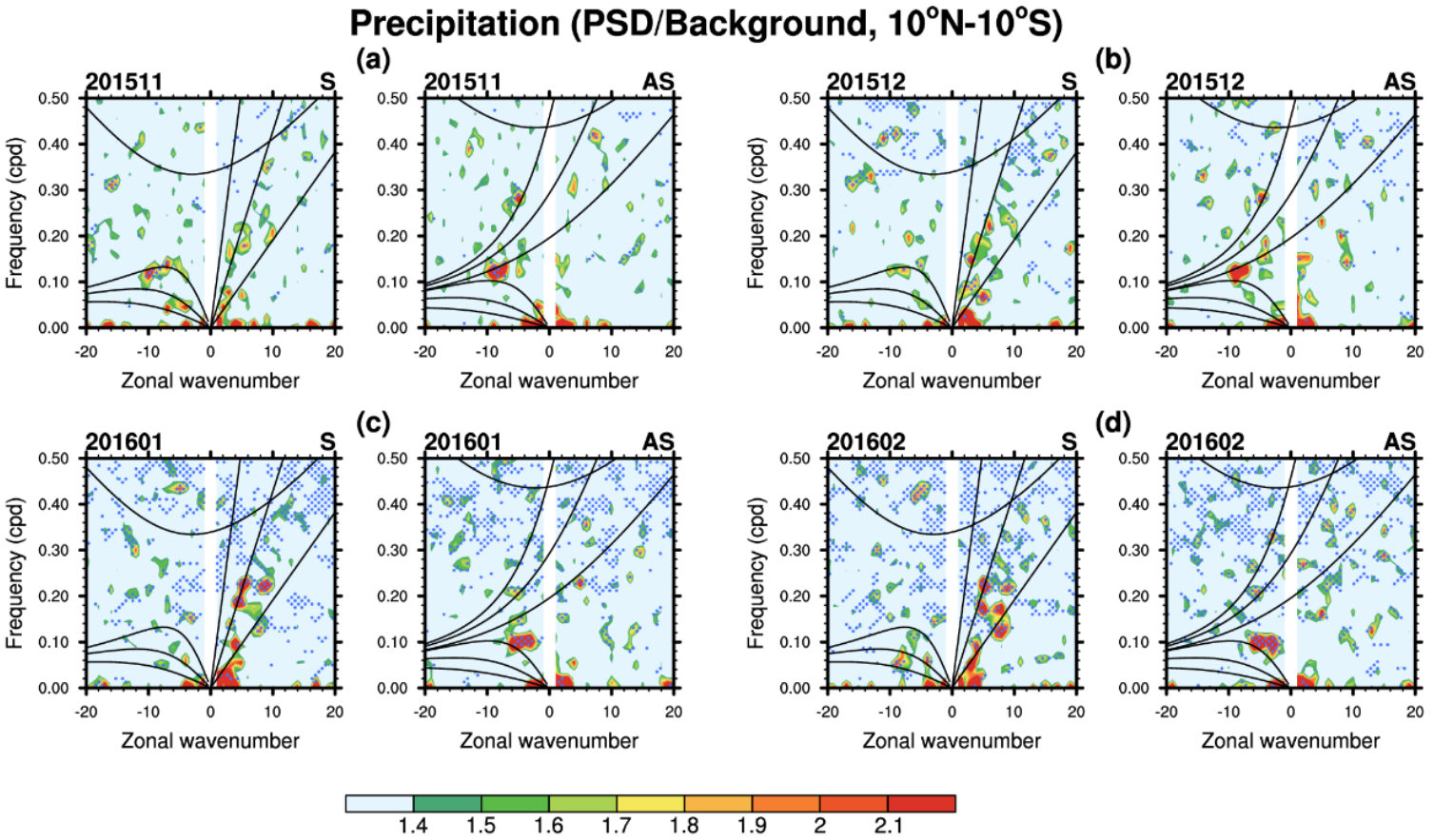

Figure 10. Power spectral density of the MERRA-2 precipitation divided by the background spectrum (see text for details) as function of zonal wavenumber and frequency for (left) symmetric and (right) antisymmetric components averaged over 10°N–10°S in (a) November 2015, (b) December 2015, (c) January 2016, and (d) February 2016. When the ratio between the raw power and the background power is larger than 1.4, it is considered a statistically significant spectrum at 95% level. The blue-stippled pattern denotes a spectrum where the power is stronger than the climatology by more than its standard deviation. Thick solid lines denote theoretical dispersion lines of each equatorial waves for the equivalent depth of $\boldsymbol{h}$ = 8, 40, 240 m, although only $\boldsymbol{h}$ = 8 m line is shown for IG waves.

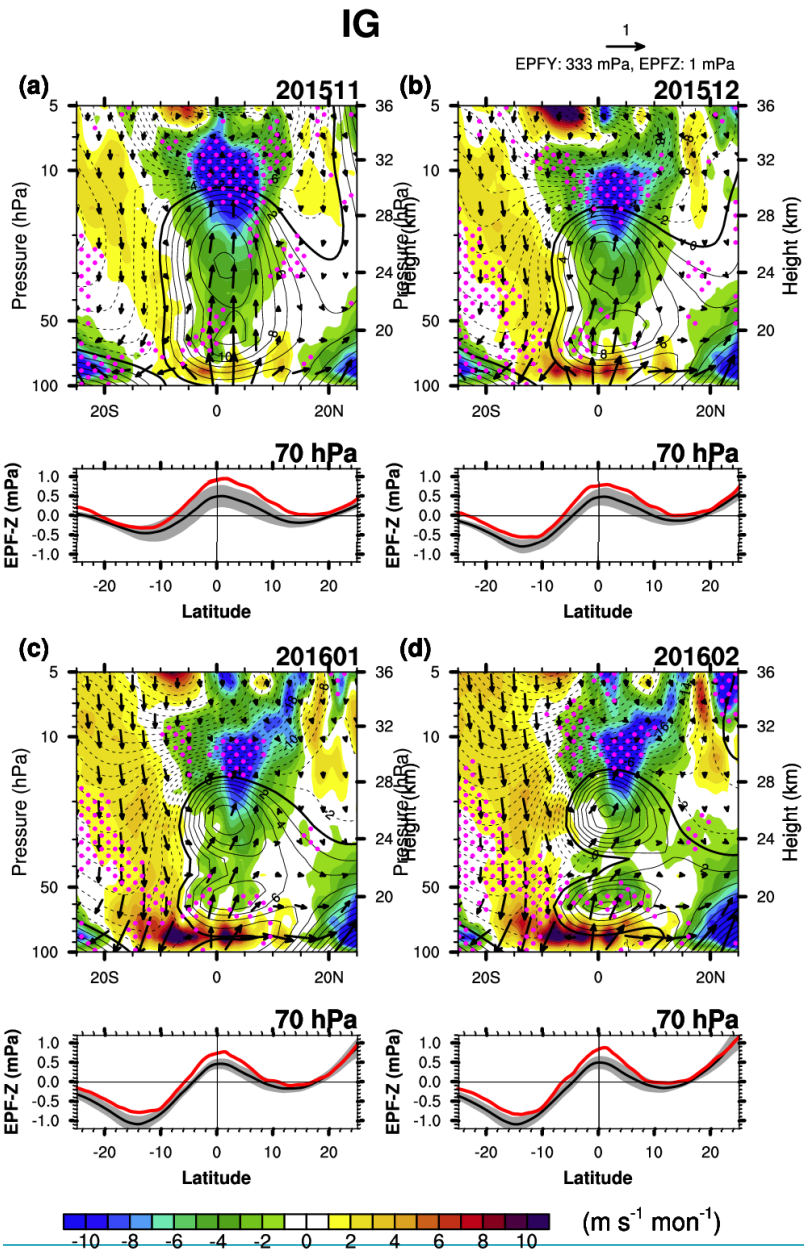
IG
EPFY: 333 mPa, EPFZ: 1 mPa
(a)
201511
(b)
201512
(c)
201601
(d)
201602
Pressure (hPa)
Height (km)
20S
0
20N
70 hPa
EPF-Z (mPa)
Latitude
(m s-1 mon-1)

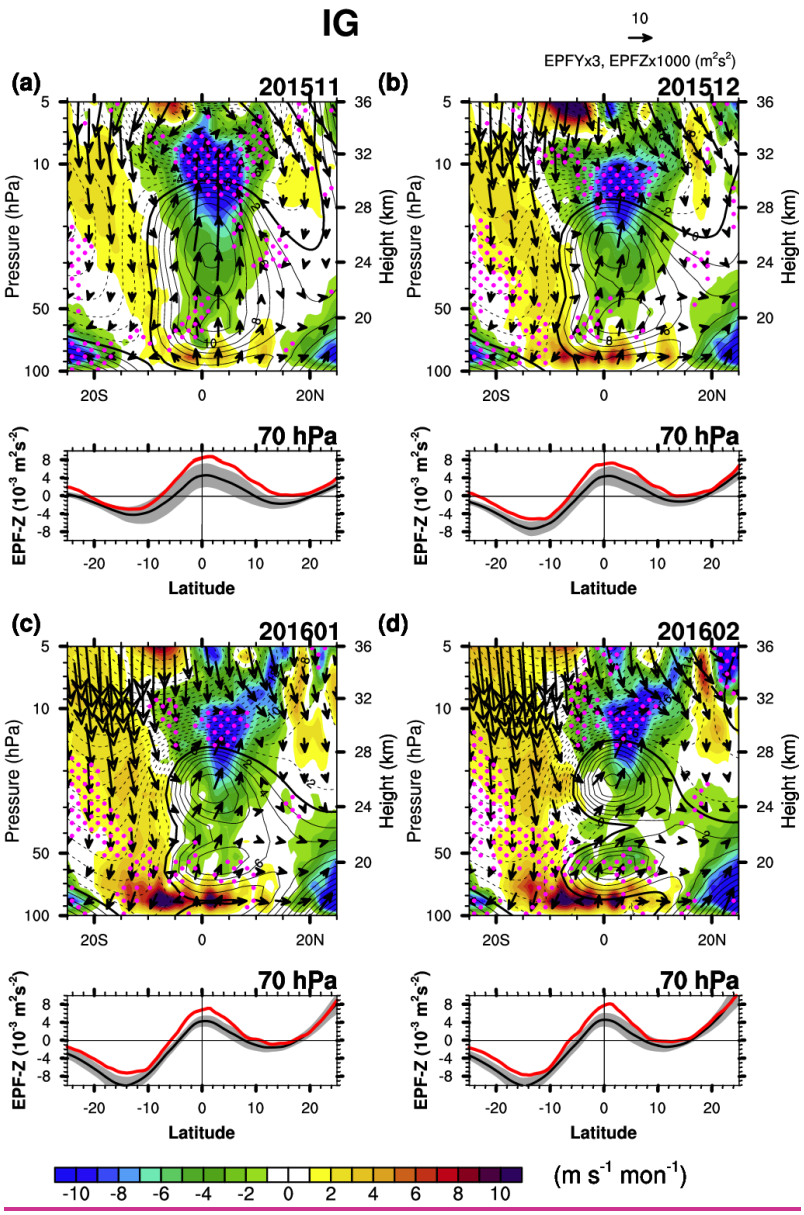

Figure 11. Latitude–height cross sections of the EP flux (vectors) divided by air density and EP flux divergence (shading) for the IG waves (multiplied by 4) with the (bottom) vertical EP flux for the IG waves at 70 hPa in (a) November 2015, (b) December 2015, (c) January 2016, and (d) February 2016 (red) and their monthly climatology (black) with ±1 standard deviation (gray shading). Positive (negative) zonal winds are plotted with solid (dashed) lines with a contour interval of 2 m s^{-1}, and thick contour lines denote a zero zonal wind speed. The magenta stippled pattern represents a region where the EPD is

algebraically smaller (more negative) than the climatology by more than its standard deviation. Here, EPF and EPD are multiplied by 8 and 4, respectively.

925

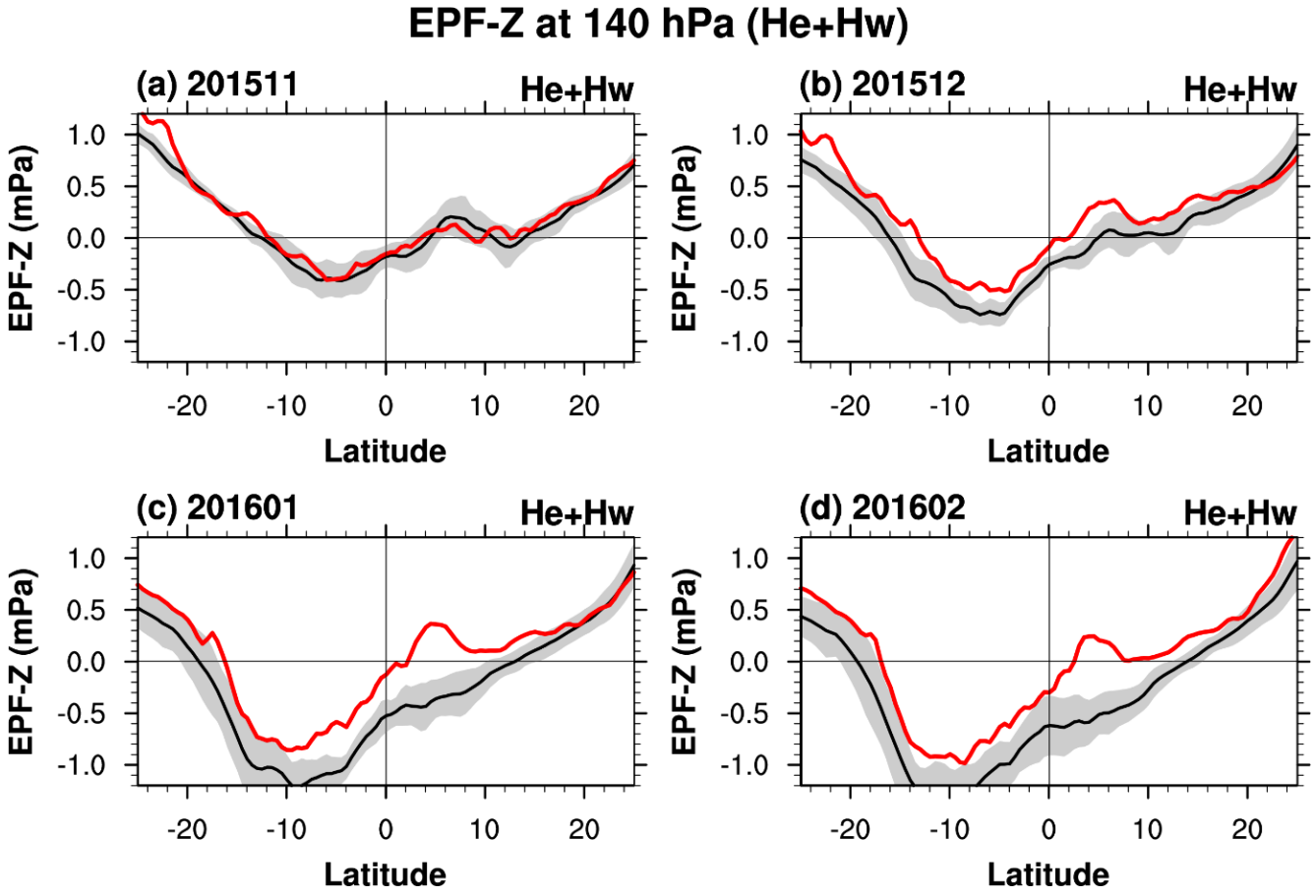

930

Figure 12. Vertical EP flux at 140 hPa for the $\boldsymbol{H_e + H_w}$ waves [(i) $|\boldsymbol{k}| > 20$ and $\boldsymbol{\omega} > \mathbf{0}$ cpd or (ii) $|\boldsymbol{k}| \leq 20$ and $\boldsymbol{\omega} > 0.4$ cpd; approximately for the IG waves] in (a) November 2015, (b) December 2015, (c) January 2016, and (d) February 2016 (red) and their monthly climatology (black) along with ± 1 standard deviation (gray shading).

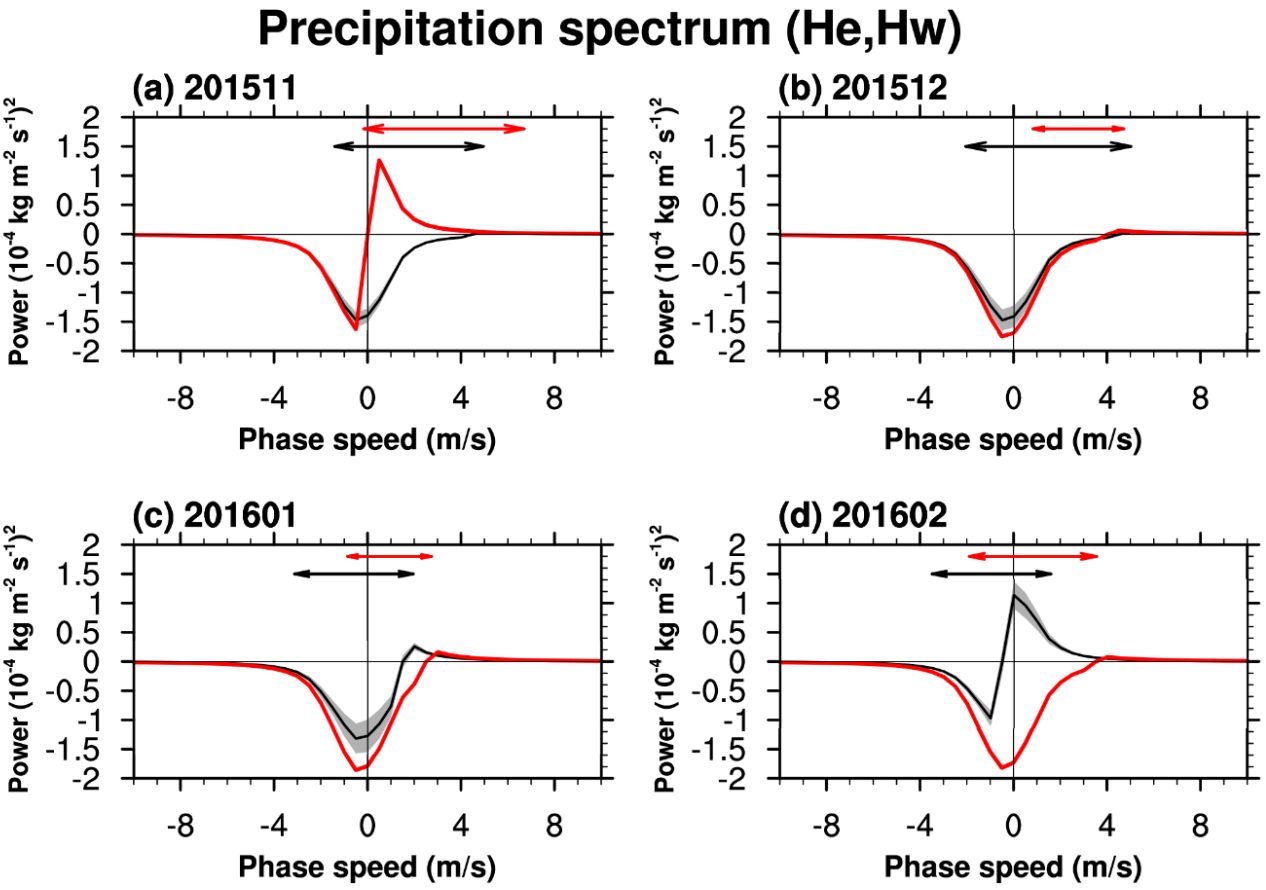
Precipitation spectrum (He,Hw)
(a) 201511
(b) 201512
(c) 201601
(d) 201602
Power (10^{-4} kg m^{-2} s^{-1})^2
Phase speed (m/s)
2
1.5
1
0.5
0
-0.5
-1
-1.5
-2
-8
-4
0
4
8

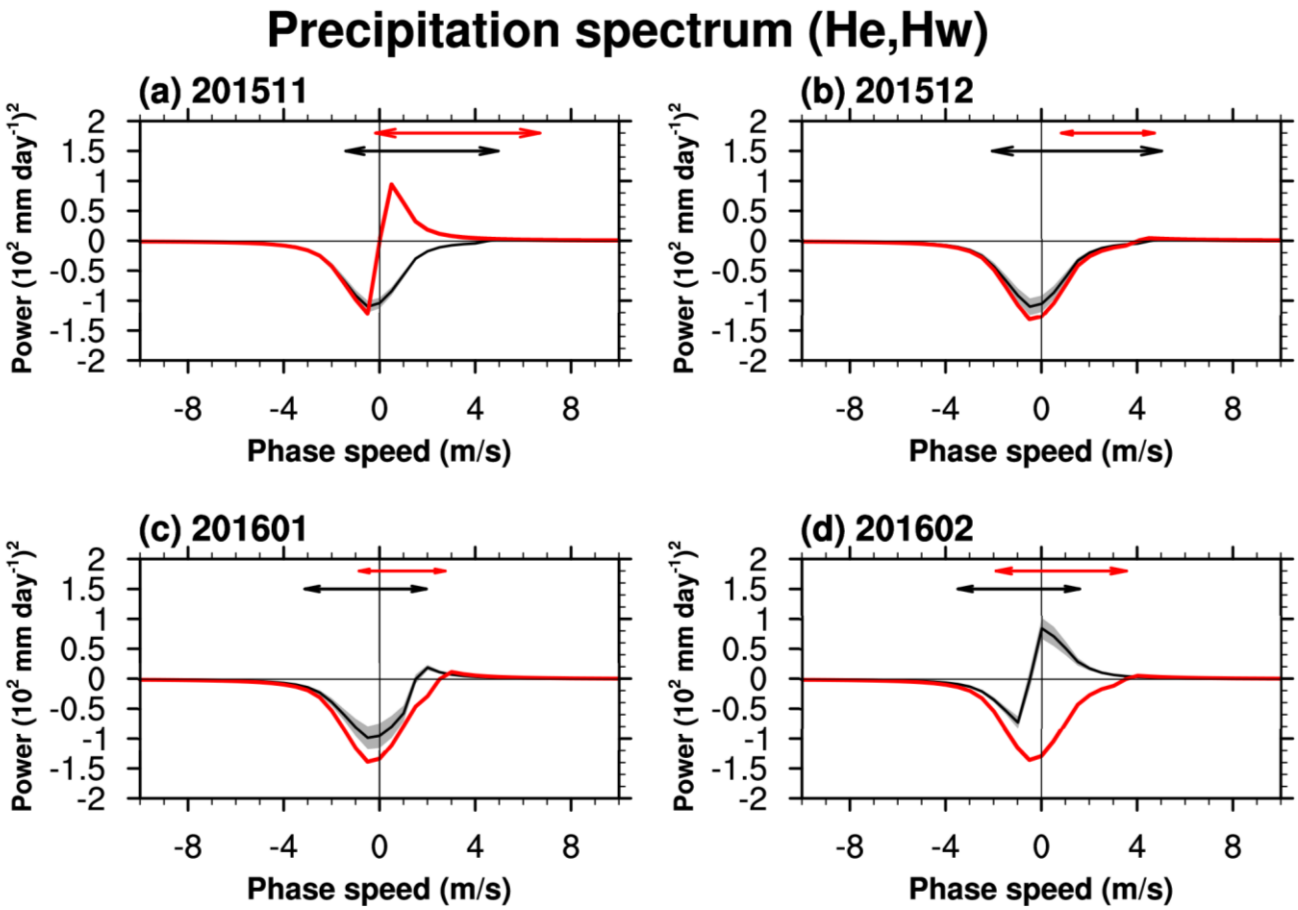

940

Figure 13. Phase-speed spectra of the precipitation in the spectral range of the $\boldsymbol{H_e + H_w}$ waves [(i) $|\boldsymbol{k}| > 20$ and $\boldsymbol{\omega} > 0$ cpd or (ii) $|\boldsymbol{k}| \leq 20$ and $\boldsymbol{\omega} > 0.4$ cpd; approximately for the IG waves] averaged over 10°N–10°S in (a) November 2015, (b) December 2015, (c) January 2016, and (d) February 2016, and their monthly climatology (black) along with ±1 standard deviation (gray shading). Note that the power is multiplied by a negative sign when the phase speed is smaller than the zonal-
945 mean zonal wind at 140 hPa (i.e., source level). Double-sided arrows represent zonal wind ranges from 140 hPa to 70 hPa for the QBO disruption period (red) and the climatology (black).

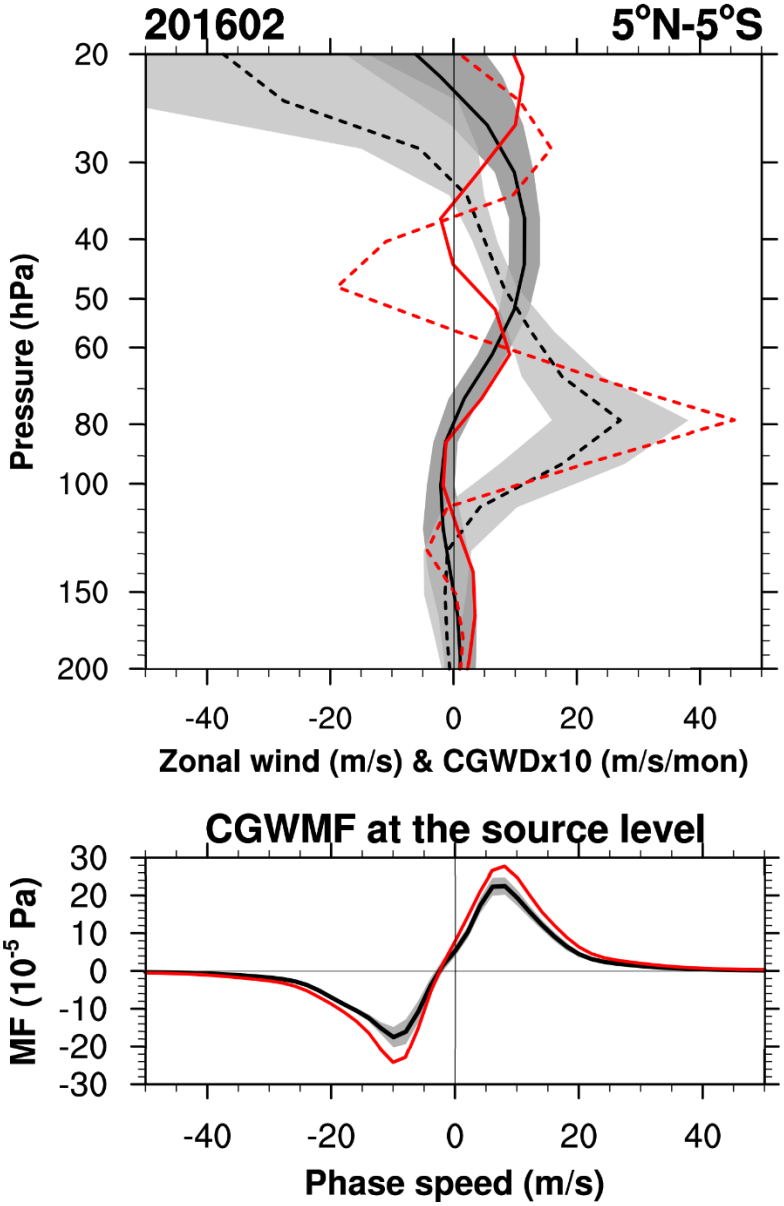

950 **Figure 14.** (Top) The zonal-mean zonal wind profile and the zonal-mean CGWD profile averaged over 5°N–5°S in February 2016 (red solid and red dashed, respectively) and those for the climatology (black solid and black dashed, respectively) with ± 1-standard deviation (dark-gray and light-gray shading, respectively). (Bottom) Phase-speed spectra of the zonal-mean zonal CGW momentum flux at the source level averaged over 5°N–5°S in February 2016 (red) and the climatology (black) with ± 1-standard deviation (gray shading).

955

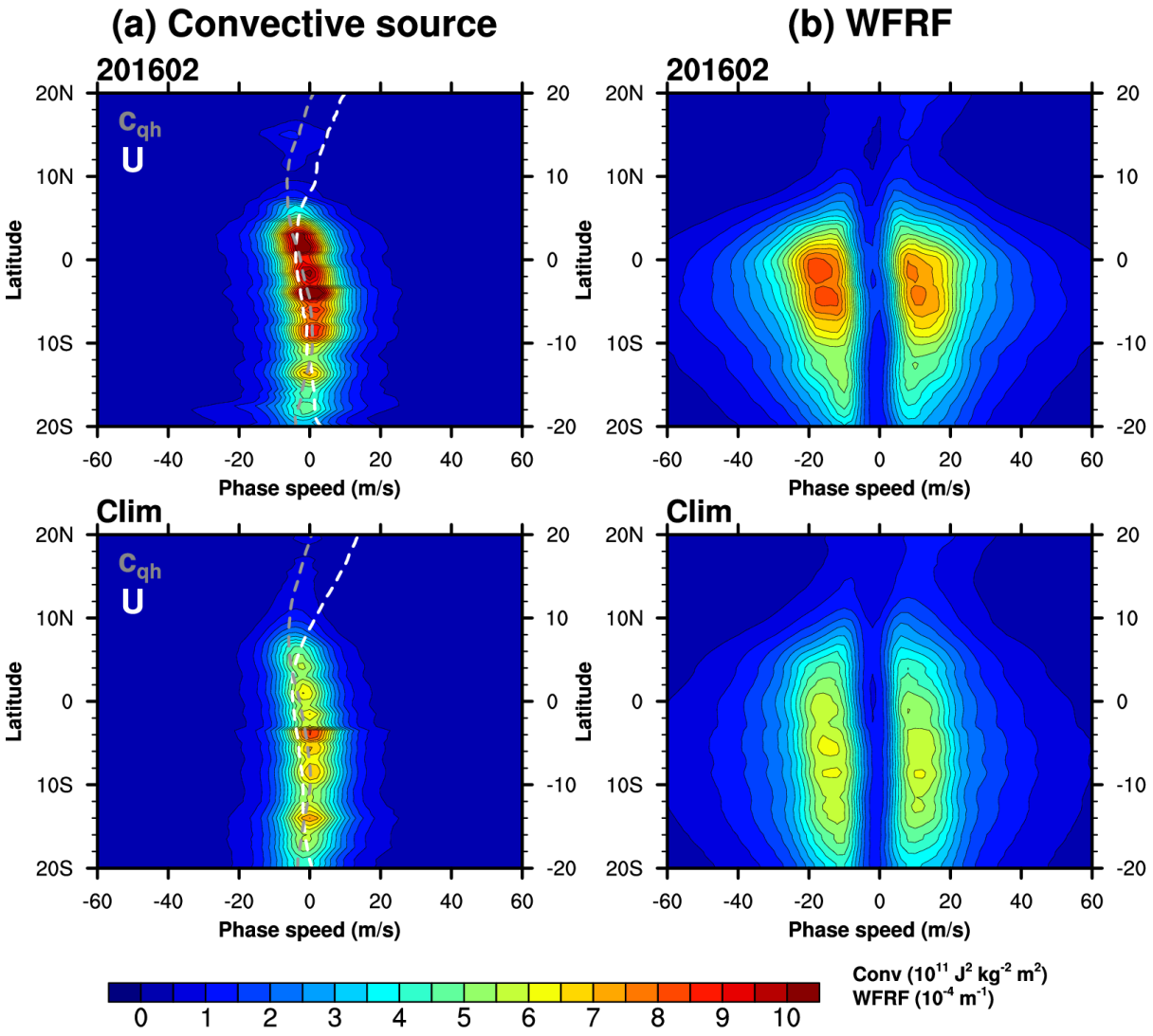

960 **Figure 15.** Latitudinal distributions of (left) zonal-mean convective source spectrum and (right) wave-filtering and resonance factor (WFRF) spectrum in (top) February 2016 and (bottom) the climatology. White and gray dashed lines in the convective source spectrum denote zonal-mean zonal wind ($\boldsymbol{U}$) and the moving-speed of convection ($\boldsymbol{c_{qh}}$), respectively.

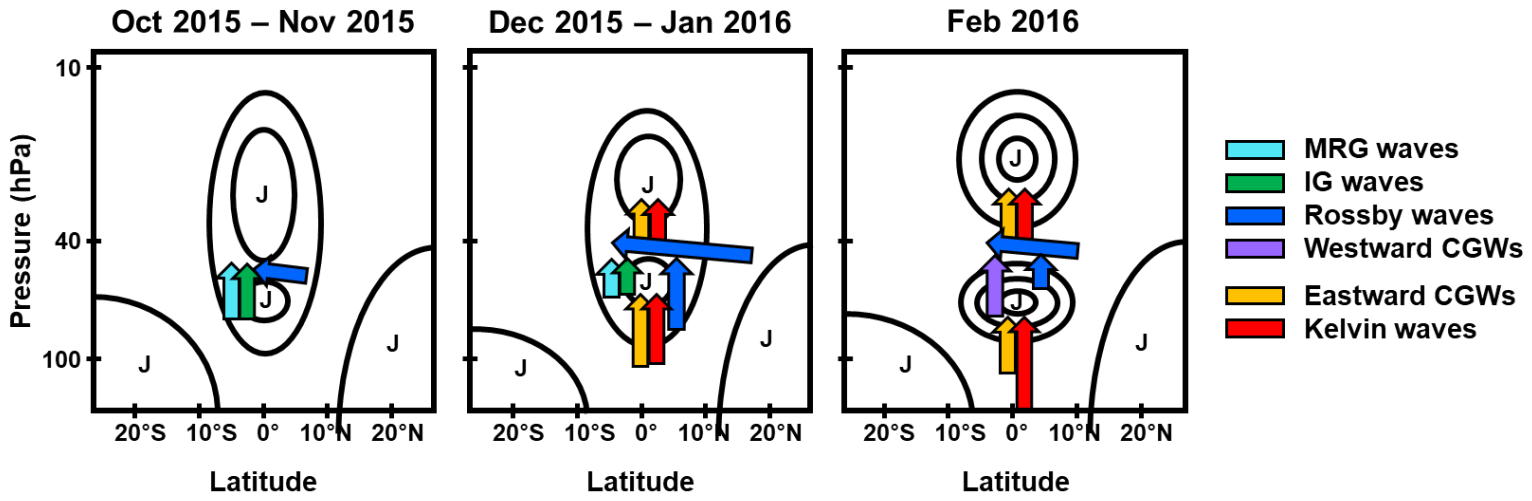

965

Figure 16. Schematic of the zonal wind evolution (black contour) and the anomalous wave forcing (arrow) during the QBO disruption in October 2015–November 2015 (left), December 2015–January 2016 (middle), and February 2016 (right). The "J" denotes a westerly jet.

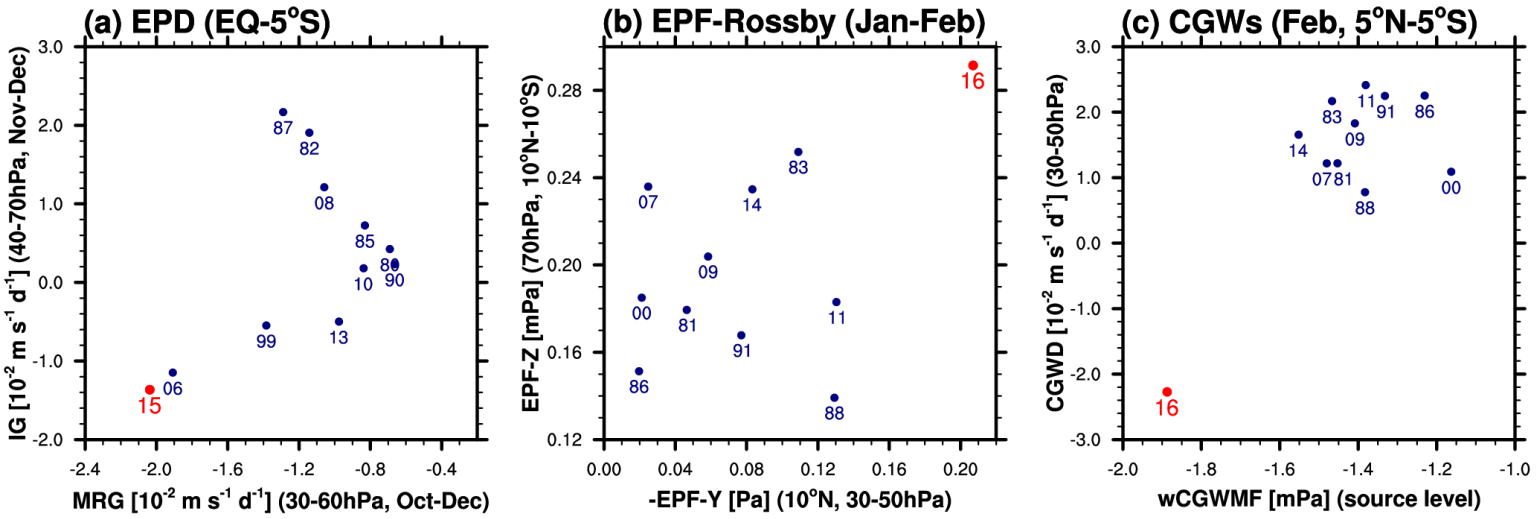

Figure 17. Scatter plots of the (a) EP flux divergence (EPD) for the MRG waves (*x*-axis) and that for the IG waves (*y*-axis) at 0°–5°S, averaged for October–December in 40–60 hPa and November–December in 30–70 hPa, respectively, (b) meridional EPF (multiplied by -1) at 10°N and 30–50 hPa (*x*-axis) and vertical EPF at 70 hPa in 10°N–10°S (*y*-axis) for the Rossby waves averaged for January–February, and (c) westward CGW momentum flux at the source level (*x*-axis) and the zonal-mean zonal CGWD (*y*-axis) in 30–50 hPa at 5°N–5°S averaged for February. Red dots denote the disruption year (2015–16) and dark-blue dots denote the other years with WQBO phases.